DOKUZ EYLÜL UNIVERSITY
GRADUATE SCHOOL OF NATURAL AND APPLIED SCIENCES

THREE DIMENSIONAL MODELING AND MONITORING OF A MAN MADE SLOPE USING IMAGES TAKEN FROM UNMANNED AERIAL VEHICLE

Ali Alper SAYLAN

April, 2020
İZMİR

THREE DIMENSIONAL MODELING AND MONITORING OF A MAN MADE SLOPE USING IMAGES TAKEN FROM UNMANNED AERIAL VEHICLE

A Thesis Submitted to the
Graduate School of Natural and Applied Sciences of Dokuz Eylül University
in Partial Fulfillment of the Requirements for the Degree of Master of Science
in Civil Engineering, Applied Geotechnical Program

Ali Alper SAYLAN

April, 2020
İZMİR

M.Sc THESIS EXAMINATION RESULT FORM

We have read the thesis entitled **"THREE DIMENSIONAL MODELING AND MONITORING OF A MAN MADE SLOPE USING IMAGES TAKEN FROM UNMANNED AERIAL VEHICLE"** completed by **ALİ ALPER SAYLAN** under supervision of **ASSOC. PROF. DR. OKAN ÖNAL** and we certify that in our opinion it is fully adequate, in scope and in quality, as a thesis for the degree of Master of Science.

Assoc. Prof. Dr. Okan ÖNAL

Supervisor

Prof. Dr. Gürkan ÖZDEN

(Jury Member)

Assoc. Prof. Dr. Selman SAĞLAM

(Jury Member)

Prof.Dr. Kadriye ERTEKİN

Director

Graduate School of Natural and Applied Sciences

ACKNOWLEDGEMENTS

I would like to express my special appreciation and thanks to my advisor, Assoc. Prof. Dr. Okan ÖNAL, he has been a tremendous mentor for me. I would like to thank you for encouraging my research and for allowing me to grow as a research assistant. His advice on both research as well as on my career have been priceless. I would never have accomplished my goals without his guidance and encouragement.

I would also like to thank Prof. Dr. Gürkan ÖZDEN, Prof. Dr. Yeliz YÜKSELEN AKSOY, Assoc. Prof. Dr. Ali Hakan ÖREN for their contributions and helps throughout my M.Sc study. Also, I need to express my special thanks to Dr. Tuğçe ÖZDAMAR KUL for her help and support. They all were not just my teachers. They were always behind me in hard times. I will not forget these supports forever.

I must express my very profound gratitude to my wife, Çiğdem for providing me with unfailing support and continuous encouragement throughout master's degree study and through the process of researching and writing this thesis. Thank you for being my muse, editor and proofreader. But most of all, thank you for being my best friend.

This thesis is part of the TÜBİTAK 1001 Project 116M506: "*Sayısal Görüntü İşleme Tekniklerinin Şev Ve Dolguların Üç Boyutlu Topoğrafik Modellerinin Kurulumuna Uygulanması Ve Kalibrasyonu Üzerine Bir Araştırma: İnsansız Hava Araçlarından Alınan Sayısal Görüntülerin Kullanımı*". I would like to thank TÜBİTAK for the financial and technical support provided by the project and my master's degree education.

Ali Alper SAYLAN

THREE DIMENSIONAL MODELING AND MONITORING OF A MAN MADE SLOPE USING IMAGES TAKEN FROM UNMANNED AERIAL VEHICLE

ABSTRACT

In this thesis, it is aimed to use topographic models obtained from aerial photographs using image processing techniques for the stability analysis of slopes and embankments. "Structure from Motion" technique was used to create topographic surface models from aerial photographs. In this context, overlapping images were taken from different perspectives and three-dimensional numerical models of the study area created. The models were calibrated with the real coordinates taken from the control points. Thus, three-dimensional models were moved to the actual coordinates and scaled to actual dimensions. Three-dimensional surface models created at high level of detail were compared with time interval and it was observed that the movements in the terrain could be monitored quantitatively. The unique aspect of this project was the establishment of the three-dimensional finite element model by using the high resolution surface model obtained from the photogrammetric methods and transfer the data obtained from the field. For this purpose, a systematic study was carried out in order to transform three-dimensional models in the quality that finite element software can analyze. As a result of this study, it was concluded that it is not possible to transfer surface models taken by photogrammetric method to finite element software without simplification within certain limits. On the other hand, it was determined that the three-dimensional finite element analysis of the models with high polygon number cannot be completed in significant periods and it is a necessity to reduce the polygon number significantly without disturbing the surface geometry. In line with these results, a three-dimensional finite element model of an excavation slope, which had active movement and was monitored instrumentally, was created by evaluating aerial photographs and field observations and inclinometer measurements. Thus, the structural measures necessary to stop the movement were analyzed.

Keywords: UAV, digital image processing, slope stability, 3D finite element analysis

İNSANSIZ HAVA ARACINDAN ALINAN GÖRÜNTÜLER KULLANILARAK BİR YARMA ŞEVİNİN ÜÇ BOYUTLU MODELLENMESİ VE İZLENMESİ

ÖZ

Bu tez kapsamında şev ve dolguların stabilite analizleri için görüntü işleme teknikleri kullanılarak hava fotoğraflarından elde edilmiş topografik modellerinin kullanılması amaçlanmıştır. Hava fotoğraflarından topografik yüzey modellerinin oluşturulması için "Hareket Tabanlı Yapısal Modelleme" tekniği kullanılmıştır. Bu kapsamda farklı perspektiflerden birbiri ile kesişen hava görüntüleri alınmış ve bunlar işlenerek sahanın üç boyutlu sayısal modelleri oluşturulmuştur. Oluşturulan modeller kontrol noktalarından alınmış koordinatlarla kalibre edilmiş ve model gerçek koordinat ve boyutlara taşınmıştır. Farklı tarihlerde yapılan uçuşlar ile yüksek detay seviyesinde oluşturulmuş üç boyutlu yüzey modelleri birbiri ile kıyaslanmış ve arazideki hareketlerin niceliksel olarak takip edilebildiği görülmüştür. Fotogrametrik yöntemlerle elde edilen yüksek çözünürlüklü yüzey modelinin ve araziden elde edilen verilerin sonlu elemanlar modeline aktarılması bu projenin özgün yanını oluşturmuştur. Bu maksatla üç boyutlu modellerin sonlu elemanlar yazılımlarının analiz edebileceği niteliğe taşınması amacıyla sistematik bir çalışma yürütülmüştür. Bu çalışma sonucunda yüzey modellerinin belirli sınırlar dahilinde sadeleştirilmeden sonlu elemanlar yazılımına aktarılmasının mümkün olmadığı sonucu ortaya çıkmıştır. Öte yandan poligon sayısı yüksek olan modellerin üç boyutlu sonlu elemanlar analizlerinin anlamlı sürelerde tamamlanamadığı, yüzey geometrisini bozmamak koşuluyla poligon sayısının önemli oranda azaltılmasının bir zorunluluk olduğu belirlenmiştir. Bu sonuçlar doğrultusunda, aktif olarak hareketin devam ettiği ve aletsel olarak izlenen bir kazı şevinin üç boyutlu sonlu elemanlar modeli hava fotoğrafları ve sahada yapılan gözlem ve inklinometre ölçümleri değerlendirilerek oluşturulmuş ve hareketin durdurulması için gerekli yapısal önlemler analiz edilmiştir.

Anahtar Kelimeler: İHA, sayısal görüntü işleme, şev stabilitesi, 3B sonlu elemanlar analizi

CONTENTS

LIST OF FIGURES

LIST OF TABLES

Page

CHAPTER ONE
INTRODUCTION

1.1 Landslides

Landslides, which are one of the disasters that cause the most considerable loss of life and property from past to present, occur as a result of the loss of stability of natural slopes or artificial excavations or fillings. Landslides, defined as the movement of rock, debris, or soil mass on a slope, occur with the failure in the material under shear stress (Cruden, 1991). The high shear stress on the soil or the low shear strength of the soil are the two main factors in the initiation of the sliding process (Varnes, 1958). Apart from these, the water penetrating the ground can cause landslides by increasing the shear stress due to aggravation of the soil and by decreasing the shear strength due to reducing the effective stress on the slip circle. The factors such as removal of horizontal structural supports, formation of new slopes on previously slipping zones, insufficient slope angles, extra surcharge load to the slope crown, uncontrolled fillings, earthquakes, scouring originating from wave and river flow, filling of water into the crack on slopes and increasing horizontal stresses as a result of swelling on the ground may also cause shear stress to increase. On the other hand, weak layers existing in the soil, roundness of the soil particles, discontinuities, change of water content in the ground, and thermal changes can also cause the landslide to be triggered.

Landslide geometry and material properties should be well known in order to understand the landslide mechanism better. Thus, measures to be taken against landslides can be determined correctly. In the context of the classification of landslide types, the first study was introduced by Varnes (1958). In this study, Varnes classified landslides according to slip geometry and material type; and separated the material types as rock and soil. In another study by Varnes (1978), in addition to his previous work, he elaborated on the material types with grain sizes and reclassified them to rock, debris (predominantly coarse), and earth (predominantly fine). An important source for the classification of the landslide was revealed by Hutchinson (Hungr, Evans, Bovis, & Hutchinson, 2001). In contrast to Varnes, Hutchinson categorized landslide types with kinematic patterns rather than taxonomic classification. Varnes and Hutchinson's classification systems are the most accepted systems that constitute the basis for the posterior classification studies.

The wide scope of the landslide phenomenon and the complexity and diversity of its effects against human and nature make it difficult to reveal a single landslide definition. For example, landslides with fast and large masses are the most destructive and dangerous type. Slow and deep-seated landslides can lead to a considerable loss of property rather than loss of life (Guzzetti, Carrara, Cardinali, & Reichenbach, 1999). Preventing such losses before the disaster is possible with the measures taken in the light of the data obtained by landslide monitoring and analysis.

1.2 Landslide Monitoring

Temporal and spatial monitoring of slope mobility is an essential source of data on the dynamic and structural characteristics of the landslide (Savvaidis, 2003). The velocity and magnitude of the displacements are indicative of stability status. In the case of using early detection instruments by landslide monitoring, it is possible to prevent a landslide before it occurs. If a landslide begins, monitoring indicates the extent of the destruction and helps to damage assessment studies.

Some instruments perform time-dependent monitoring of slope stability conditions, especially in areas such as open mines and excavations. As the pioneering application in slope stability monitoring, tapes and wire devices were used by measuring the cracks on retaining walls and soil surfaces (Gili, Corominas, & Rius, 2000). Afterward, with the development of technology, it was possible to observe the amount of movement for not only the damaged points on the structures but also the desired points by classical measuring instruments such as theodolites, electronic distance measurers, and total stations (Ashkenazi & Yau, 1986). The disadvantage of these techniques is that only surficial measurements can be taken, and no data can be obtained about the slip in the ground. This problem was overcome by measuring the displacements in the normal axis of the borehole with inclinometer systems installed by penetrating into the ground

(Dunnicliff, 1993). Inclinometers provide important sliding parameters by calculating failure depth and displacement data (Stark & Choi, 2008). In addition to providing information about the stability characteristics, these parameters are the sources for transferring the discontinuities to the numerical models for stability analysis.

1.3 Slope Stability Analysis with Numerical Methods

Limit equilibrium method (LEM) and finite element method (FEM) are frequently used in slope stability analysis. LEM, which is a traditional and well-understood technique, is preferred by engineers and researchers due to its simplicity (Cheng, Lansivaara, & Wei, 2007; Liu, Shao, & Li, 2015). Although the result of the stress-strain condition is not obtained with LEM, it is a practical solution method for simple problems (Cheng et al., 2007). Nevertheless, LEM is an approach that ignores the plastic flow rule for the soil body and works with rigid slices (Yu, Salgado, Member, Sloan, & Kim, 1998). In addition to this, it is not satisfactory to consider a global equilibrium condition (rather than the equilibrium situation at every point). FEM is distinguished by the fact that it divides the soil into small pieces and calculates with elastoplastic material formulas (Schweiger, 2005). The points that FEM is superior to LEM (Griffiths & Lane, 1999) are as follows:

- The shape and position of the sliding surface do not require any prediction or prior knowledge. The fail occurs naturally at the point where the shear strength of the soil is surpassed.
- The soil is not sliced, and the global equilibrium is preserved until the moment of fail.
- Deformations results can be calculated at working stress levels.
- Shear failure can be monitored progressively.

A disadvantage of FEM, according to LEM, is that the computational solution durations are long, especially in the 3-D analysis (Cheng et al., 2007). It is predicted that this problem will be reduced to the levels that can be ignored by the development of computer software and hardware. On the other hand, the most critical problem faced by FEM is the calculation of the factor of safety. As a method of solution for this problem, the shear strength reduction (SSR) method was proposed by Zienkiewicz et al. (1977). The basic principle of this method is to systematically reduce the shear strength parameters of the soil until failure. The factor of safety value is the rate of reduction of parameters. Numerous numerical studies have shown that this is an effective method (Huang & Jia, 2009). Shear strength parameters that caused the slide (c'_f and Φ'_f) are defined as the ratio of the initial parameters of the soil (c' and Φ') to the shear strength reduction factor (F_t),

$$c'_f = \frac{c'}{F_t} \tag{1.1}$$

$$\Phi'_f = \arctan\left(\tan\Phi'/F_t\right) \tag{1.2}$$

Although traditional 2-dimensional analyses are considered sufficient for many cases, landslides have 3-dimensional characters. For example, in a 2-dimensional analysis, the positive effect of the arching mechanism resulting from the transfer of the sliding block to the bordering sides is ignored. It results in 2-dimensional analysis to produce more conservative values than 3-dimensional analysis (Hicks & Spencer, 2010). Besides, the landslide may not always occur in a straight direction. In such cases, the selection of the most pessimist vertical cross-section is complicated by the engineer. Even if the most pessimist section is correctly selected, it yields conservative results (Griffiths & Marquez, 2007). It should be noted that, even in complex topographies, possible slip planes can be determined naturally by using FEM in 3D analyses (Alkasawneh, Husein Malkawi, Nusairat, & Albataineh, 2008). In addition, the variable soil structure, which has a direct effect on geotechnical structures (pile, anchor, rock bolt), can be modeled much more realistically in 3D analyses (Li, Hicks, & Nuttall, 2015).

Whether it is 2D or 3D, all slope stability numerical analyses require a model. In 2D analyses, less detailed topographic studies may be enough, whereas in 3D analyses, if a complex topography such as a mine site is concerned, numerical modeling becomes more complicated, and more comprehensive studies are required. In recent years, with the development of remote sensing methods such as Lidar and photogrammetric methods, digital surface models (DSM) of large areas can be created both in shorter periods and relatively inexpensively.

In slope stability analysis, the results become more reliable by increasing the detail of the geometry of the terrain, which is one of the main objects for slope stability analysis. However, in today's technology, there are still problems in the computational time for 3D computer analysis. Performing analyses with the high-resolution field surface model increase the required computational time. It causes many practitioners to prefer 2D software instead of 3D. However, with the further development of computer technology, analyses can be performed faster, and more detailed analysis results can be obtained.

1.4 Structure from Motion

The past decade has witnessed significant technological advances in numerical terrain modeling and geomorphological terrain analysis (Gupta & Shukla, 2017). High-quality numerical modeling of topography, one of the most essential characteristics of the ground, is available in today's technology. However, many measurement methods require both intensive expertise and financial resources (Micheletti, Chandler, & Lane, 2015). At this point, the importance of Structure from Motion (SfM) technique shows up. The SfM technique uses multiple overlapping photos of the same scene from different perspectives to generate a great detail 3D reconstruction. This is a photogrammetric method with a much lower cost compared to other classical methods such as Lidar, a laser-based scanning system for high-resolution topography, or RTK-GPS based land surveys (Carbonneau & Dietrich, 2017; Leon, Roelfsema, Saunders, & Phinn, 2015; Micheletti et al., 2015; Ruggles et al., 2016; Stumpf, Malet, Allemand, Pierrot-Deseilligny, & Skupinski, 2015; Westoby, Brasington, Glasser, Hambrey, & Reynolds, 2012; Yu, Huang, Zhou, & Mao, 2017).

In this remote sensing method, a 3-dimensional point cloud of the terrain is obtained by using the photographs acquired from land or air. (Koschitzki, Schwalbe, Cardenas,

& Maas, 2017; Savvaidis, 2003). It is advantageous compared to other geomorphological monitoring methods by monitoring not only the local points but the whole terrain surface. The comparison of the models created with the use of the images made with time intervals and the numerical calculation of the surface topographic differences led to a high-level slope monitoring method. In addition to this, although there is no comprehensive study in terms of complex topographic areas in the literature, it has the great potential for very realistic slope stability studies in 3D.

Topographic models can be produced with SfM, even with ordinary cameras (Micheletti et al., 2015). However, the precision required to be used in engineering and research depends on many parameters (Ružić, Marović, Benac, & Ilić, 2014). The most important ones are camera characteristics, environmental weather conditions, the number of photos taken from different heights and angles, the editing process in the software, and the number and characteristics of the ground control points.

Measurements using basic photogrammetric methods require camera orientation to determine the position of the points in the three-dimensional space (Hackl, Adey, Woźniak, & Schümperlin, 2018). SfM method can calculate the three-dimensional point coordinates with the iterative algorithms with the introduction of camera parameters (Westoby et al., 2012). SfM method uses the "Scale Invariant Feature Transform" method developed by Lowe (2004) to define common features in intersecting images, regardless of scale (Snavely, Seitz, & Szeliski, 2008). It allows the location of the points on the object or terrain surface of interest to be determined in three dimensions. With this technique, the sparse point cloud is created by recognizing common points on the intersecting photos, and then this model is developed and transformed into a dense point cloud (Furukawa & Ponce, 2010). As a result of the development of image processing analysis, it was possible to create high-resolution digital terrain models and dense point clouds automatically with SfM technique (Gupta & Shukla, 2017; Javernick, Brasington, & Caruso, 2014). In this way, according to the terrestrial measurement methods, SfM technique can create high-detailed numerical models very quickly (Siebert & Teizer, 2014).

1.5 Scope of the Study

Within the scope of this thesis, time-dependent monitoring and slope stability analyses carried out by the photogrammetric method for a mining site located in Çine district of Aydın were investigated. The mine site has a total area of about 45 hectares, and active landslide affects about 8 hectares. The wide field of this site and the complex geomorphology site brought the analysis to be carried out in high detailed in 3D.

Decreasing the level of detail of the items that are important for analysis within the study to the level that finite element software can process was the most critical part of the study. In addition to inclinometer data and field observations to determine the boundaries of the moving mass, a particular case was the use of data obtained from the comparison of point clouds generated from aerial photographs at different times in the creation of the finite element model.

In the last phase of the study, finite element analyses were performed for structural measures to prevent slope movement. The measures that emerged as a result of these studies were not only in the theoretical analysis phase but also implemented in the field. However, as of the date the thesis was written, only the rock bolts above +500 elevation and above were completed. In this respect, the effect of rock bolts on slope movements could be observed during the thesis.

In recent years, there is very little literature on the use of photogrammetric methods in geotechnical applications, which is a popular research topic in the field and has recently begun to be used in practice. The specific purpose of the study is to explain each step of this method in detail and thus to create a case study for applications.

CHAPTER TWO
GEOLOGICAL AND GEOTECHNICAL EVALUATION OF THE LANDSLIDE

The landslide area is an open mine site located in Aydın, Çine (Figure 2.1). The mine has an area of 45 hectares, and the highest elevation point is 543m, and the lowest point has an elevation of 382m. The man made slopes are formed with benches, and the face angles of these benches vary between 40°-50°.

Figure 2.1 An image of the open mine site (Personal archive, 2018)

The increase of the depth due to the excavation operation caused stability problems in various regions of the field. The biggest and the riskiest of these problems were investigated for stabilization within the scope of this study. Geological and geotechnical evaluations were made, and measures were taken to eliminate the landslides.

A total of 14 drillings were carried out in the application area with a depth of 40m to 70m. These drillings are named as ISK1-4 and JSK1-10. However, excess sub-surface displacements caused the ISK 1 and ISK 2 wells to collapse. In order to better understand the sliding mechanism, two new wells were opened instead of these wells. (ISK 5, ISK6). The sliding mass was evaluated with borehole data, inclinometer, and topographical monitoring and field observations. Figure 2.2 shows the location of the ISK 4, ISK 5, and ISK 6 active inclinometer wells (blue spots) and other boreholes (black spots) in the cloud model of the field. Boreholes were used for the determination of the ground parameter of these units and the determination of the boundaries of the lithological units and creation their boundary surface models, which are the source of the finite element model of the soil strata. According to the results of the laboratory experiments, gneiss, quartz-feldspar, mica-schist, feldspar (ore) and gneiss lithological units are found along the section A-A′ perpendicular to the direction of movement of the wedge-shaped landslide (Figure 2.2).

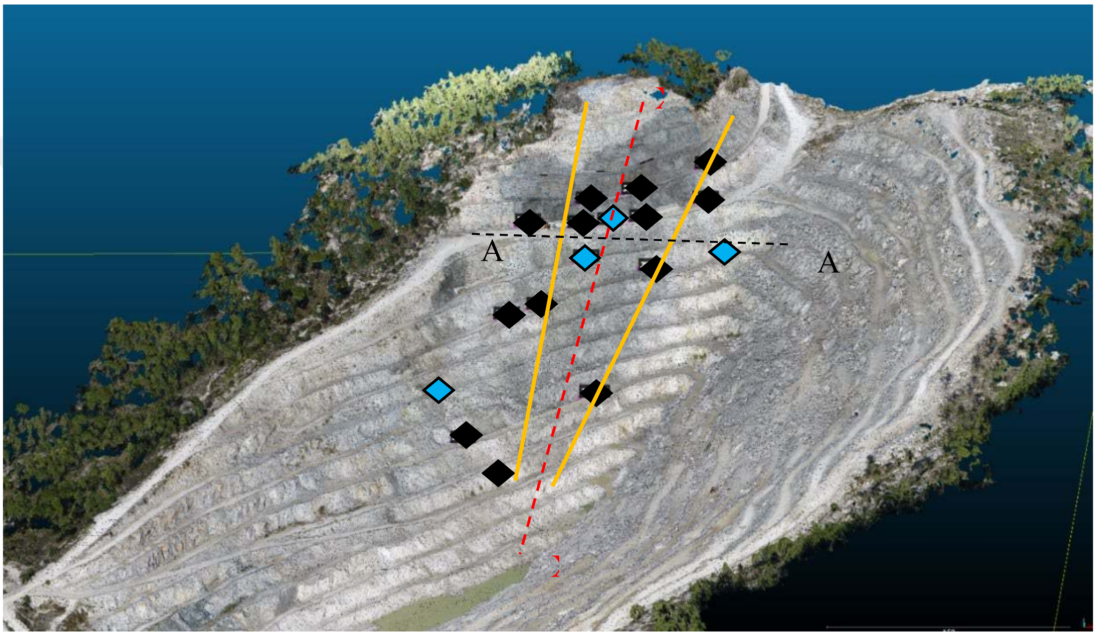

Figure 2.2 Distribution of inclinometer boreholes (blue dots, left-to-right ISK 6-ISK 4-ISK 3-ISK 5) and the other boreholes (black dots)

2.1 Landslide Mechanism

The surface width of this zone from the ore to the gneiss formation is approximately 200m. The zone is disturbed, and therefore it is in quite complicated form due to the presence of several shear zones (i.e., spinal mica discontinuities). The shear zones are rich in mica formations, the majority of which weathered to the degree that they attained soil behavior. The yellow lines in Figure 2.2 represent the boundaries of sliding mass. The mica zones that were developed along the shown direction in Figure 2.3 are regarded as shear bands being parallel to the large shearing zone that resulted in ore formation in the geological sense. The landslide zone, therefore, is bounded by the thick mica zone on the south-east and relatively thin shear band consisting of lenses and spinal shaped mica zones on the north-west.

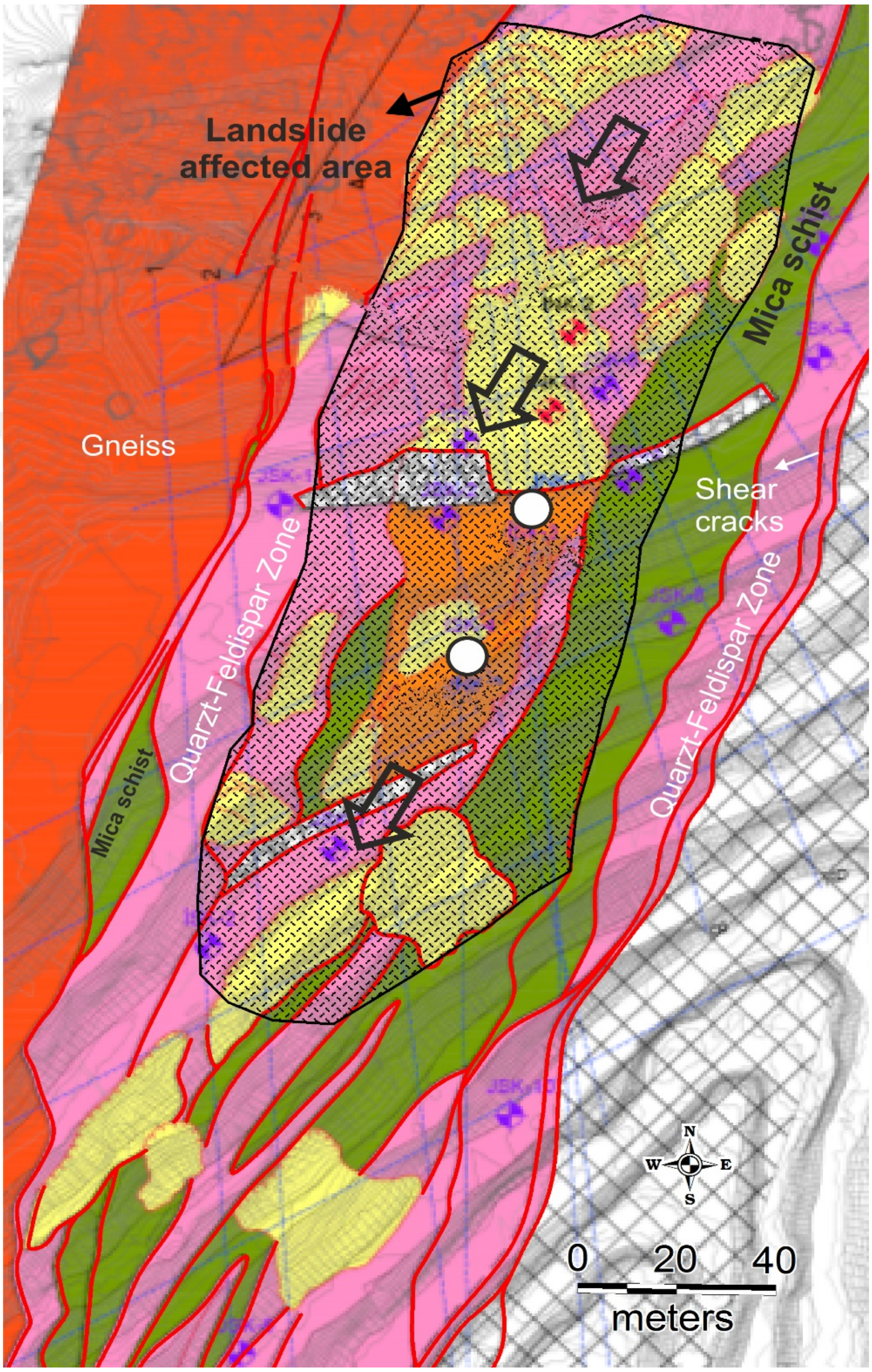

Figure 2.3 The effective area of the ellipsoid landslide with its sliding direction and surface geology

The landslide that is active along the cut-slopes of a mine site elongates parallel to mica zones. The sliding direction intersects the north-west side slope steps with an acute angle (~30°) (Figure 2.2). Therefore, the landslide is not orthogonal to the slope steps being perfectly parallel to the mica-schist veins. This mechanism can be better observed in Figure 2.3, where the outcrops of the mica-schist zone on the right-hand side of the moving mass are shown with a minimum and maximum thickness of 10m and 40m, respectively. The mica-schist on the left-hand side, however, exposes itself with rather small outcrops. The landslide affects an area of approximately 14620m2. The south-east boundary of the NE-SW elongating ellipsoid shaped landslide area is passing through the aforementioned mica-schist vein.

The lithological units can be seen visually in Figure 2.4. The units are indicated by arrows and are marked with gneiss (beige), quartz-feldspar unit (blue), mica-schist (dark gray), feldspar unit (red), feldspar (green) and gneiss (beige) arrows from left to right respectively.

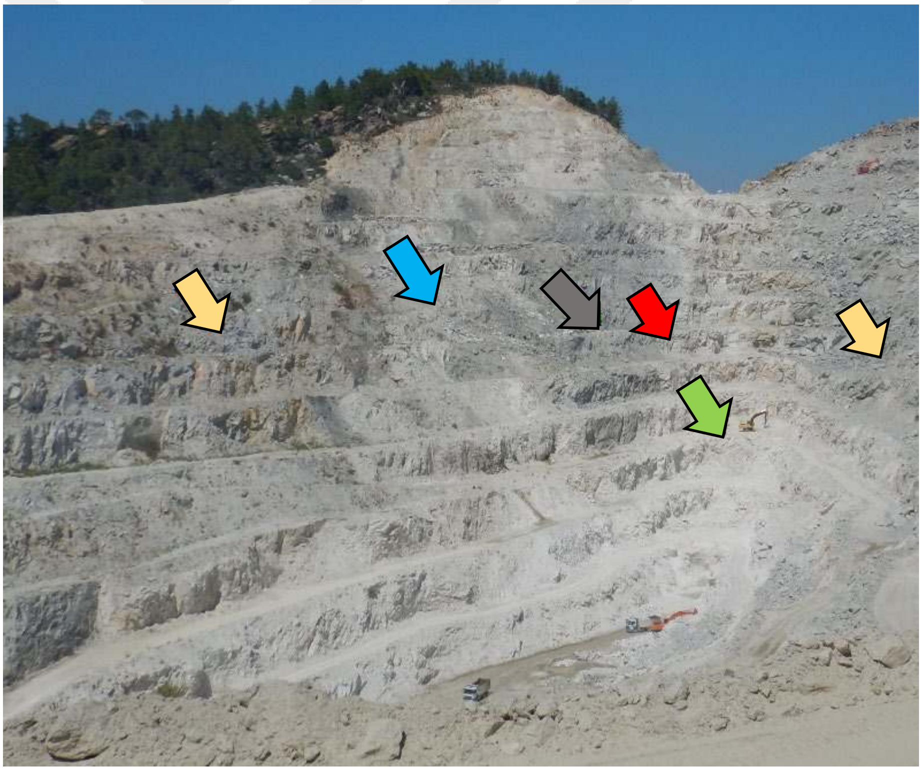

Figure 2.4 The lithologic units on the terrain (Personal archive, 2018)

Some surficial evidences define various types of mass movements that took place as a result of disturbances generated by the shear bands. One may reach to this conclusion due to the existence of mica-schist fault zones and quartzite outcrops and investigating the thickness of the surface soil cover, as shown in Figure 2.3. The principal mechanism that triggered mass movements, however, is the presence of the thick mica zone along with thinner mica spinal veins inside the landslide area. This fact is demonstrated by the geologic cross-section, as presented in Figure 2.5. The slip circle of the landslide covering entire mass movements commences from the outskirts of the hill, passing through the thick mica zone tracing an arc shape towards the south-west.

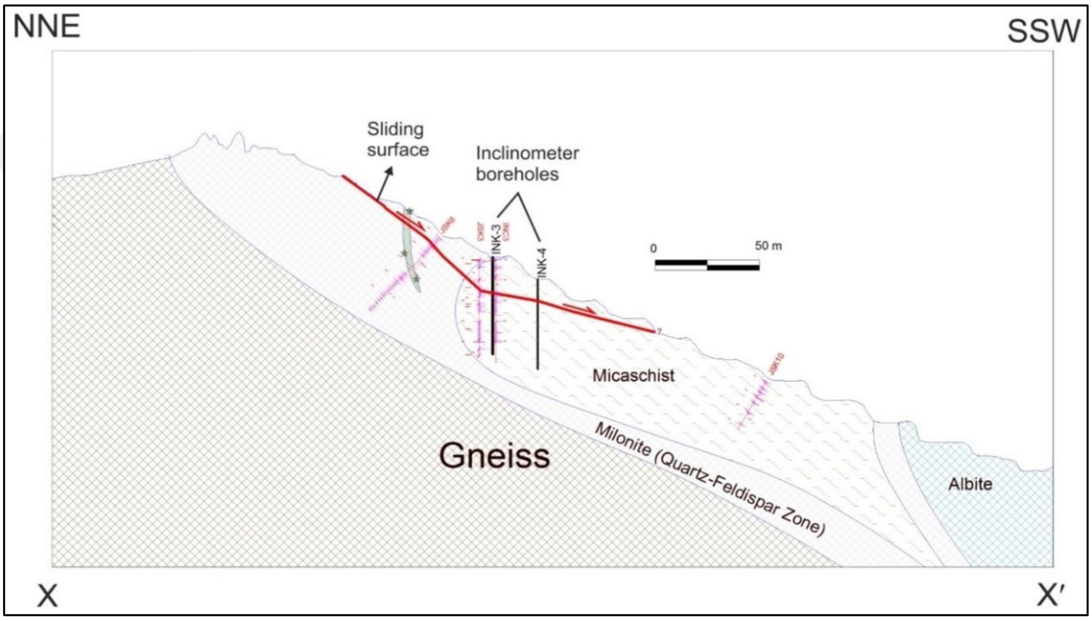

Figure 2.5 Location of the slip circle determined by considering the inclinometer data and the geological structure

Figure 2.5 is sufficient to visualize the characteristic of the slip, but it does not provide sufficient data for analysis for such a complicated condition. Because the effect of mica-schist units on both sides of the sliding mass, which directly affect the sliding, cannot be shown in a 2-dimensional slope stability analysis with the cross-section. Moreover, in such cases, the mistake in selecting the correct cross-section may lead to the results unsafe (Griffiths & Marquez, 2007). In addition, considering the complex topographic structure of the land, it was decided to analyze this slope problem in 3-dimensional.

2.2 Laboratory Shear Strength Tests on Mica-schist

The laboratory and field surveys were clearly shown that the mica-schist has a direct impact on the formation of landslides. The tendency to slip, especially in rainy periods, caused cracks on the micaceous surface. The effect of rain on the anisotropic mica-schist shear strength is much more pronounced than the other rocks. In a simple observation, it is almost impossible to disassemble a mica-schist rock fragment with hand in the natural water content while a saturated mica-schist fragment can be easily dismantled. The strength values of this observational state can be determined by using the strength tests. For this purpose, laboratory direct shear box experiments were performed on the disturbed mica-schist samples taken from the field.

Mohr-Coulomb shear strength values were investigated in two cases in direct shear box experiments on mica-schist samples (Figure 2.6). The first one is the experiment with the disturbed sample in the natural water content, and the other is the experiment for the post wetting state by adding water to the disturbed sample in the natural water content at a time while the shearing is in progress. The addition of water represents a sudden occurrence of precipitation in the field.

Figure 2.6 Direct shear box test system (Personal archive, 2019)

The natural water content of the material is w=15%. The disturbed material was prepared in natural water content and manually compressed in a standard mold of direct shear test with a unit weight of 1.9 gr/cm^3 (Figure 2.7). Both experiment cases (at natural water content and fully wetted state) were performed with three different normal stresses (N=0.5 kg/cm^2, N=1.0 kg/cm^2, N=2.0 kg/cm^2. The wetting operation was performed at the time the shear strain reached 1% in order to make the experiments comparable.

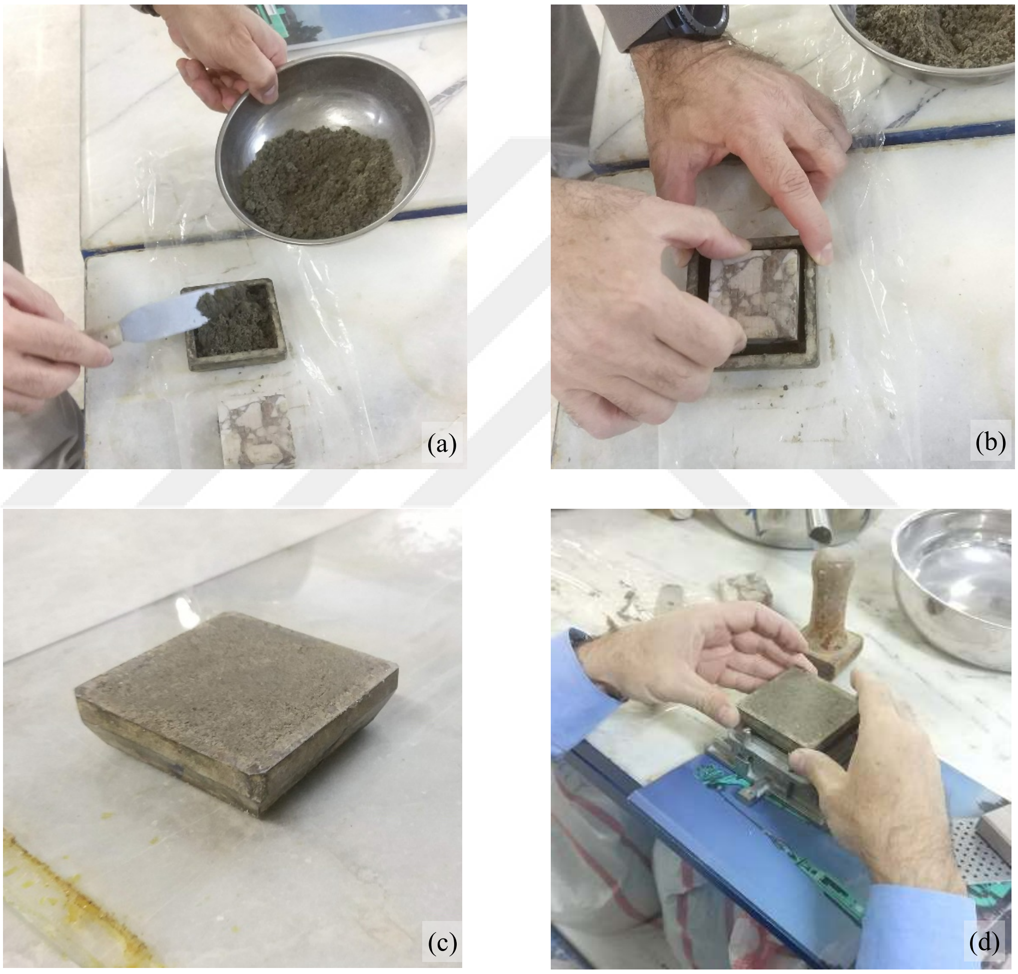

Figure 2.7 Insertion (a), compaction (b), compacted condition (c), and placement of the sample in natural water content in the direct shear test box (Personal archive, 2019)

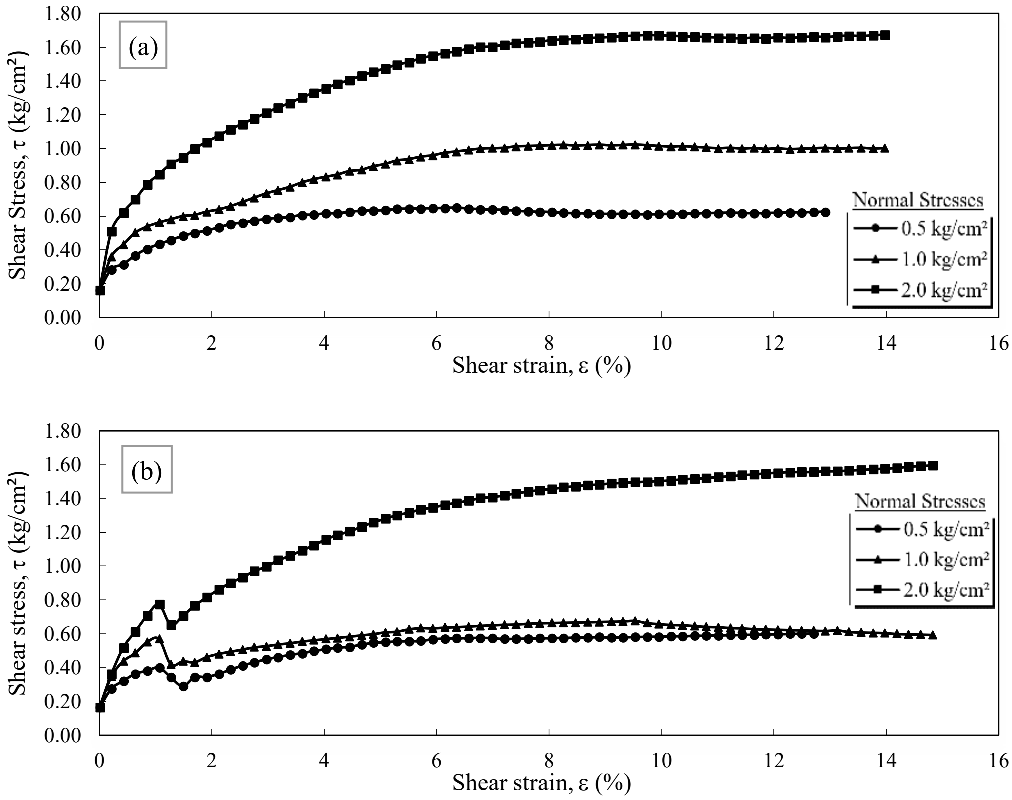

Figure 2.8 Stress-strain behavior of the mica-schist specimen in different normal stress in standard (a) and wetted (b) conditions

Shear stress-shear strain graphs obtained as a result of the experiments are shown in Figure 2.8. In all experiments, the effect of water addition can be seen. The sudden changes in the graph show the effect of post wetting. The shear strength values of the material have decreased significantly after the wetting operation under all normal stresses. The Mohr-Coulomb failure envelope is shown in Figure 2.9.

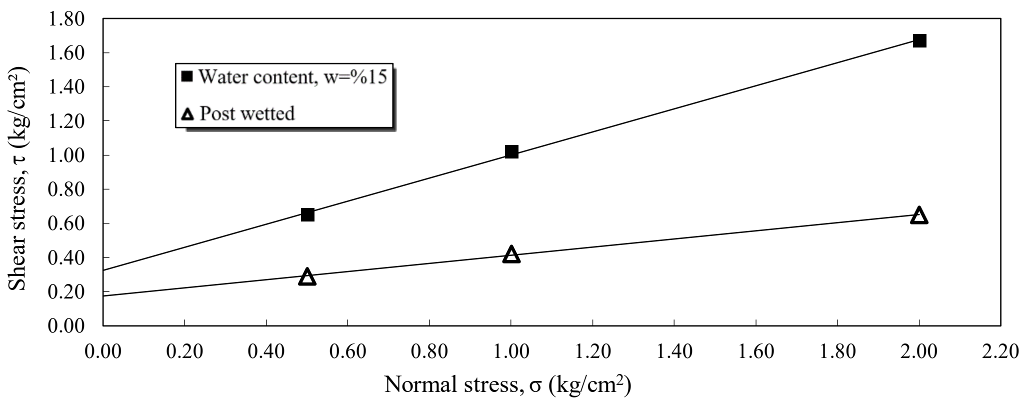

Figure 2.9 Mohr-Coulomb envelopes for two different conditions

Figure 2.9 shows the effect of water on the material more clearly. While the internal friction angle of the material in the natural water content is determined as 34°, and the internal friction angle of wetted sample is 13°. This effect of water was used in the finite element analysis to assign the saturated strength parameters of mica-schist.

CHAPTER THREE
TIME-DEPENDENT MONITORING OF THE LANDSLIDE

3.1 Overview

The information about surface mobility, as well as the monitoring of subsurface displacements in landslides, is an important source of data on landslide characteristics. Sub-surface displacements occurring in the field are obtained, as shown in the previous chapter. On the other hand, surface displacements have been found as a result of a numerical comparison of surface models created using images obtained with Unmanned Aerial Vehicles. It is achieved by calculating the surface differences of each point in point clouds by the software called CloudCompare. 3D point clouds were created with Agisoft Metashape software.

The displacements of the site were monitored with surface models created using aerial images obtained by UAV at five different times. Accordingly, displacements were calculated between 2 consecutive surface models, and a total of 4 different 3D monitoring matrices were generated. The calculated displacements were visualized with the displacement dependent color scale on the numerical model by the CloudCompare.

The surface models created at this stage were used for temporal monitoring as well as the primary data for the slope stability analyses described later.

3.2 Background

The trend of creating a high-resolution 3D digital surface model with the SfM method has increased the number of scientific studies in this field. In 2013, a landslide in Arizona, USA, was modeled by Ruggles et al. (2016) using Lidar and different cameras, and their effect on modeling accuracy was investigated. In this context, a GoPro Hero 3+ camera capable of 48 frames per minute with a resolution of 12 MP and the Nikon D7100 DSLR camera capable of 175 frames per minute with a resolution of 24.1 MP were used. Accordingly, numerical modeling was performed under the same conditions by the aerial images. The Nikon camera, which has better capture quality, has higher sensitivity compared to GoPro. Contrary to this advantage, however, all images taken with the Nikon camera have a much larger file size than the GoPro (13GB and 3GB respectively).

The development of the SfM method has increased its use in engineering applications (Siebert & Teizer, 2014). Notably, the ability to monitor the surface deformation in the fields thanks to time interval monitoring has made this method popular in geotechnical and geological engineering. In the study conducted by Saito et al. (2018), SfM-MVS photogrammetry methods were used to monitor the landslides triggered by earthquakes and heavy rainfalls. In the study, the landslide regions triggered by earthquakes and heavy rainfalls were determined using SfM-MVS photogrammetry methods. In this context, 54 regional landslides resulting from the 2016 Kumamoto earthquake were identified in an area of 1 km^2 in the Aso volcano region in Japan. In another study, Yaprak et al. (2018) modeled a region with a surface area of 0.5 km^2 using an unmanned aerial vehicle (UAV) for an active landslide investigation in Gaziantep in 2018. According to this, two different point clouds were generated with 2-3 cm average error, and these two different models were compared with each other, and deformations were obtained. Erenoğlu (2016) studied UAV-based land modeling to investigate the impact of active landslides on forest and vegetation cover. The results showed that it is possible to determine the current state of the landslide and the deformations. In addition, in the study, models were created with images taken from 3 different altitudes (30m, 50m, 80m), and the sensitivity of modeling due to altitude was investigated. Accordingly, it was observed that the models made with images taken from low altitudes had lower error levels.

Another advantage of the SfM method is that the models created with images taken at two different times can be compared visually to reveal the volumetric differences between them. In the study conducted by Koschitzki et al. (2017), landslides occurred in a flood area near the Las Minas river in Chile were investigated. The differences between two point clouds are obtained by the algorithm called ICP (Iterative Closest

Point), which iteratively calculates the distance between each point of the models and their nearest points (Besl & McKay, 1992). In this way, the surface differences from the flood were visualized (Figure 3.1).

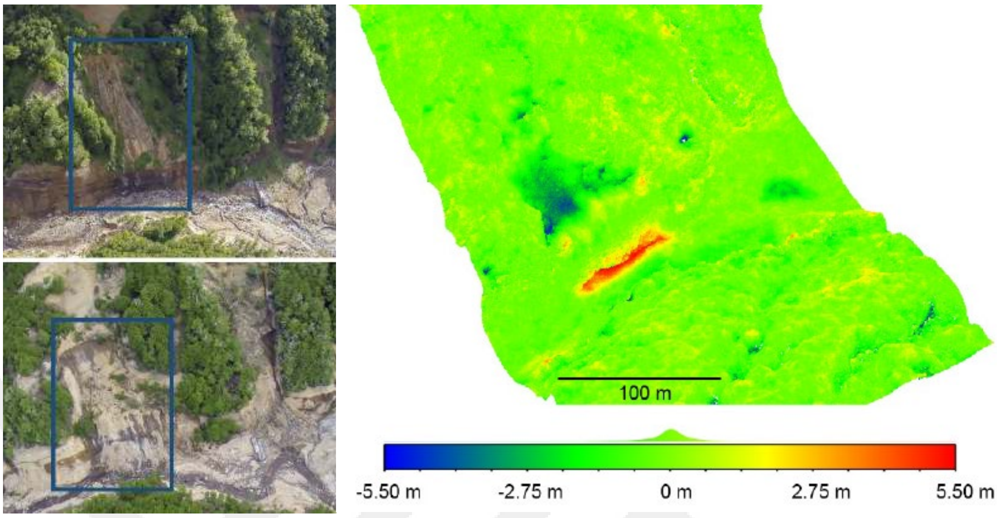

Figure 3.1 Landslide-derived surficial differences analyzed using the ICP algorithm (Koschitzki et al., 2017)

In particular, the fact that the surfaces of large-scale areas can be viewed in 3D in a digital environment has been attractive for geotechnical engineering. Aerial images taken with UAV provide quick and accurate qualitative and quantitative photographic documentation as well as a source for geotechnical stability analyses (Manousakis, Zekkos, Saroglou, & Clark, 2016). In addition, with the advantage of being able to dominate the whole field by modeling large-scale lands with UAV, it facilitates the identification of the underlying causes of geotechnical problems. In this regard, a case study was conducted by Manousakis et al. (2016) using the UAV-based SfM technique to investigate the characteristics of a rockfall that hit and damaged a house. In this context, analyses were made for the rolling path of the rock. The hardness of the site conditions in the region and the monitoring of the disaster over such a large area with aerial images for modeling a long rolling road such as 800 meters showed the importance of UAV based modeling.

During the acquisition of aerial images, the UAVs can keep a coordinate record for the flight with the GPS sensor. However, the recordings held by these devices do not have sufficient sensitivity to calibrate the digital model (James et al., 2017). Numerical modeling software works with the SfM method requires ground control points (GCP), which are located on the site, with coordinate information obtained in accordance with the local or global system in order to scale the model. Therefore it develops the model (i.e. calibration) and calculates the error between the model and the real topography (Reinoso, Gonçalves, Pereira, & Bleninger, 2018). This issue was investigated by James et al. (2017) in a study in Taroudant, Morocco. In this study, the effect of camera parameters on sensitivity was also observed. According to the results of the study, it was observed that digital models created with high quality photographs were more accurate, and the need for calibration with ground control point decreased. In order to perform the calibration correctly, ground control points must be located to cover the site. It was stated that the placement density of the ground control points depends on the required sensitivity, the quality of the camera and the topography of the land.

3.3 Materials and Methods

3.3.1 UAV System

The UAV system was developed by the researchers of this study by considering the severe conditions for aerial imaging of large open pit mines (Figure 3.2). A quad-rotor system with carbon-fiber chassis was chosen because of in-flight stability, effectiveness, and portability. Large size carbon-fiber propellers with low kV effective brushless motors were employed in the system, accompanying an Ardupilot based flight controller capable of fully autonomous flight execution. The system included several sensors connected to a flight controller for flight stability (i.e., GPS receiver, two acceleration sensors, two gyroscopes, two three-axis electronic compasses, and a barometer). The PID (proportional integral differential) loop coefficients are tuned on the aggressive side for the feedback response to maintain quick reactions for the gusty wind conditions. A Lithium-Ion power pack supplies the power for the UAV system. This pack is also engineered by the researchers of this study to provide the best possible energy density. A 4 serial- 4 parallel (4S4P) configuration of Panasonic NCR18650GA cells was established, maintaining 13.8 Ah capacity and 795 gr weight. By considering

14.8 Volt nominal voltage, 257-Watt hour per kg was obtained from the 4S4P pack, which nearly doubles the energy density of the Lithium-Polymer packs having the same capacity. Thus, approximately 1-hour flight time has been secured for the UAV for aerial operations. The only drawback of the pack is the limitation at the continuous dischargeable current due to the chemical components of the cells used. In this case, 10 ampere per cell and 40 amperes for the 4S4P configuration. On the other hand, the UAV system, including the gimbal and camera, only weights 1553 gr and requires only 16 ampere for stable hoovering with this battery pack thanks to the carbon fiber parts, efficient motors, and the weight of the high-density battery pack.

Figure 3.2 The UAV system develop by the researchers (Personal archive, 2019)

For image acquisition, a lightweight action camera (GoPro Hero 4) was used with a modification of high-quality non-distortion 5.4mm lens. Camera was mounted on a two-axis gimbal facing downwards, and images were taken in time-lapse mode with a frequency of 2 hertz.

Although having an autonomous flight capability of the UAV system, manual control over 2.4 GHz is always available for emergency cases. Besides, a long-range telemetry connection over 433 MHz is also maintained for this system. Telemetry connection secures all flight data to be sent to the home station and the failsafe option for cases where the loss of 2.4 GHz manual connection occurs.

3.3.2 Flight Planning

Although a direct line of sight between UAV and operator pilot may be established for the study area, a fully autonomous flight was planned in order to maintain 60% sidelap ratio between the flight corridors. On the other hand, on extreme points, the distance between the UAV and the operator was approximately 1 km, making it impossible to control the UAV due to visibility conditions manually. The coverage was 450000 m2 and 16 flight corridors, having 50m distance from each were completed in 32 min. The peak and the bottom points of the site has 60 m and 218 m clearance from the image plane, respectively. As a result, at least 3 overlapping images were obtained for the peak points, as greater than 9 overlaps was maintained for the remaining area. All 4 flights on different dates were conducted autonomously with this plan.

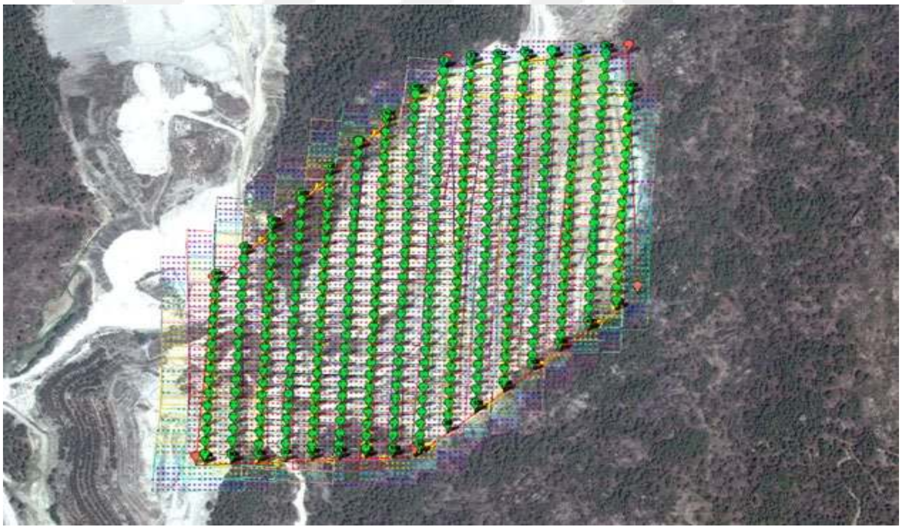

Figure 3.3 Flight plan of the UAV for autonomous image acquisition

Since the study area has 158m elevation difference at peak and bottom points, the ground control points (GCP) were carefully distributed to the site as to include the broadest possible range at elevation for each flight. The spatial distribution of the GCP was also maintained as homogeneous as possible. However, the harsh environment of the open-pit mine was the limiting factor at the deployment of the GCP. The coordinates of the GCP were determined with Realtime Kinematic GPS readings.

Significant effort was spent for the GCP deployment due to the steep slopes and inaccessibility derived from the establishment of the benches.

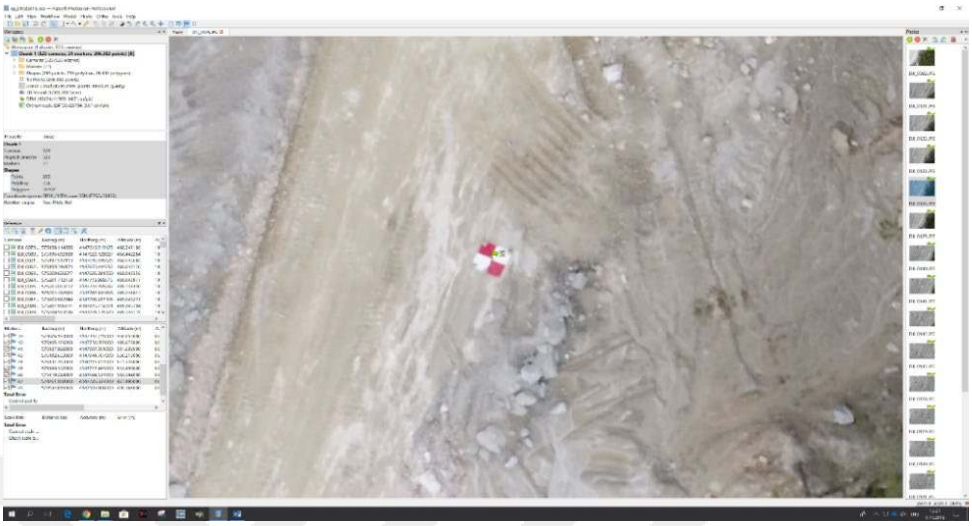

Figure 3.4 A ground control point (GCP) placed on the site

3.3.3 Data Processing

The different number of aerial images for surface models of different time were used in a commercial photogrammetry software called Metashape by Agisoft company. Firstly, images and a unique camera calibration file were transferred to form a processing chunk. This unique calibration file was created using Agisoft Lens calibration tool by imaging a calibration pattern (i.e., checkerboard) from multiple perspectives, projected to the computer monitor. Ten pattern images from different perspectives were used in order to calculate the intrinsic camera parameters of the camera. The intrinsic camera parameters are the focal length (fx, fy), principal point coordinates (cx, cy), radial distortion coefficients (K1, K2, K3), tangential distortion coefficients (P1, P2) and skew coefficient between the x-axis and y-axis (s).

Five different surface models were reconstructed by the same method. In the first step for model reconstruction, feature extraction, and 3D point generation were established by computing camera alignments. In this process, distinct features in the UAV taken images such as sharp rock edges or explicit transitions in the appearance are marked as key points. These key points are then targeted in each other image to find a match. An algorithm called SIFT is used by the software in order to track key points. SIFT algorithm recognizes features that are invariant to the image scaling and rotation and partially invariant to changes in illumination condition and 3D camera viewpoint in each image (Lowe, 2004). Once the key points are extracted, camera positions and orientations (i.e., extrinsic parameters) and the geometry of the scene are solved by an iterative procedure, resulting in a sparse point cloud (Figure 3.5). However, this point cloud is computed based on the geo-references of the UAV images, and UAVs use relatively low accurate GPS sensors comparing RTK-GPS due to the size, weight, and sampling time requirements. Therefore, optimization was performed by only using the GCP coordinates, camera extrinsic, and intrinsic parameters (Figure 3.5). By this approach, average error and pixel mean image residuals for the GCP's were obtained for the calculated scene (Table 3.1). By considering the ground resolution of the aerial images, the accuracy was found more than adequate for slope stability analyses. Niethammer et al. (2012) compared the accuracy of their study with the established studies in the literature for UAV based mass movement applications. In their study, 16 GCP was used for an area of approx. 240000 m^2 and 21.68 cm average precision was obtained. However, in this study, a low-quality compact camera was used with manual pilot-controlled UAV, and images were taken from an altitude of 200 m resulting in a ground resolution of 6 cm per pixel. On the other hand, Chandler et al. (2002) showed that <20 mm precisions may be achieved using SLR cameras and careful image acquisition planning. Researchers were used UAV based imaging for the river channel change monitoring in their study.

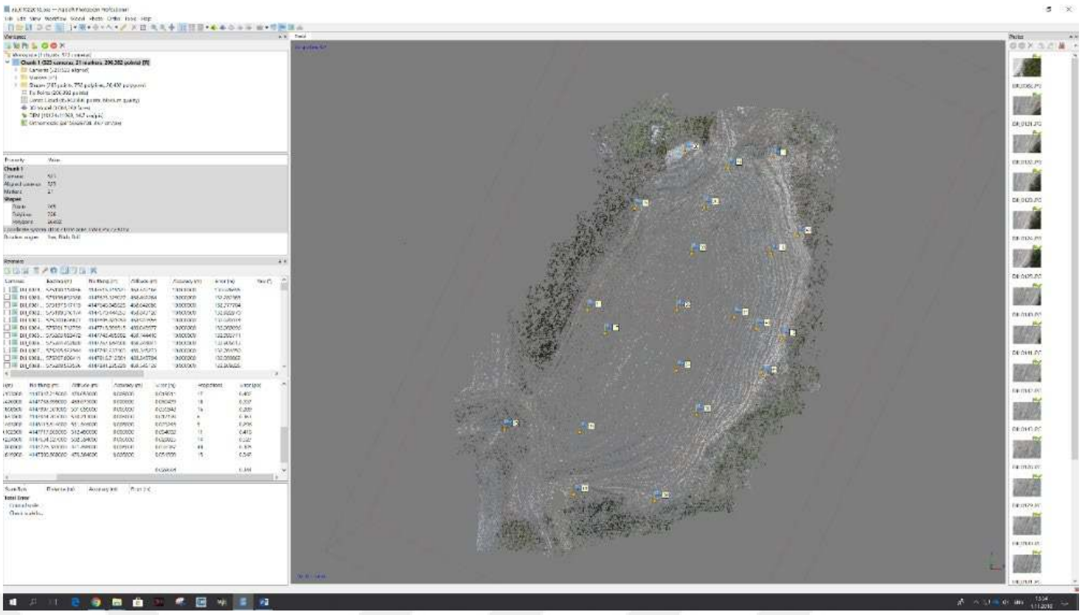

Figure 3.5 Sparse point cloud of February 2018 and the GCP’s

After the calibration and optimization stage, a dense point cloud was calculated in order to obtain several millions of points with coordinates and color value (Figure 3.6). In this particular application, a number of points which were calculated for the 4 different sparse and dense cloud respectively to reconstruct the open-pit mine topography are shown in Table 3.1.

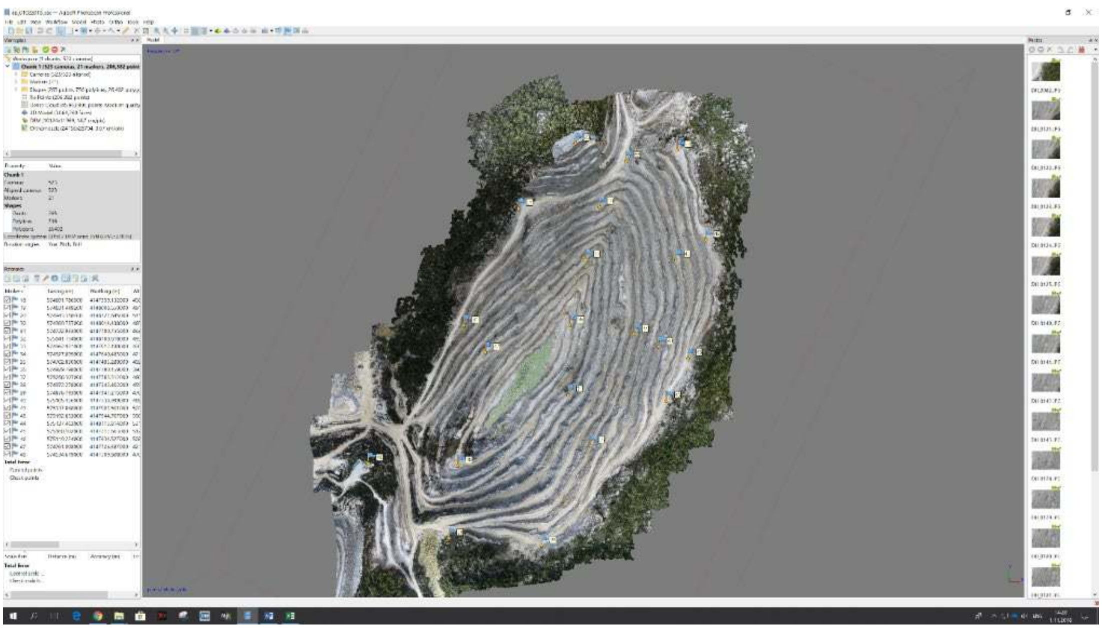

Figure 3.6 Dense point cloud of February 2018

Table 3.1 The properties of surface models with time interval

Model Creation Date	Number of GCP's	GCP average error (cm)	Number of Images	Number of Points of Sparse Cloud	Number of Points of Dense Cloud
February 2018	21	2.77	523	206000	46000000
March 2018	21	2.91	566	217000	46000000
April 2018	18	3.71	623	285000	52000000
July 2018	18	2.02	770	482000	57000000
February 2019	16	3.77	652	359000	48000000

3.3.4 Comparison of the Topographical Models

The comparison of surface differences between the models created with time intervals reveals the displacements in the field. The software can calculate the differences on each axle separately or measure the absolute difference. Besides, mesh-mesh, mesh-cloud, or cloud-cloud comparison options are available depending on the type of surface model. In these comparisons, cloud-to-cloud distances were calculated in all 3 axes (Δx, Δy, Δz). Calculation of these distances was made according to the *nearest neighbor distance* between points of clouds (Figure 3.7). This distance is the distance of each point on the reference point cloud to the nearest point in the other point cloud (CloudCompare, n.d.). The critical point here is that the point with a high point density must be selected as a reference. If the intensity is not too high, the nearest neighbor distance calculation may not be performed sufficiently accurately. However, the fact that each point cloud created within the scope of the thesis has a high point density, was made this effect neglected in the selection of reference cloud.

In this study, point density differences between the models are not considerable. The February 2018 model was used as the reference to monitor the changes in displacements according to the initial situation (Figure 3.8). Each of the models was compared to the previous model, and displacements were obtained based on the previous photo acquisition date.

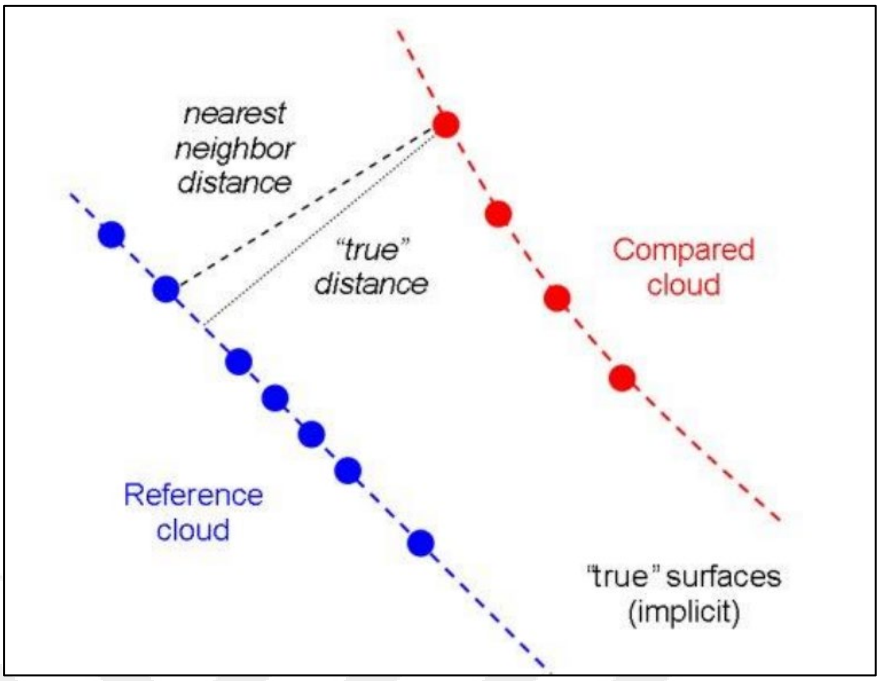

Figure 3.7 Cloud-Cloud distances (CloudCompare, n.d.)

The comparison was made by focusing only on the landslide region. For this purpose, all surface models are cropped to the same dimensions. Then, four comparisons were made between the cloud-cloud distance calculation of five surface models. Each comparison was performed between two-time successive surface models (Figure 3.9- Figure 3.12).

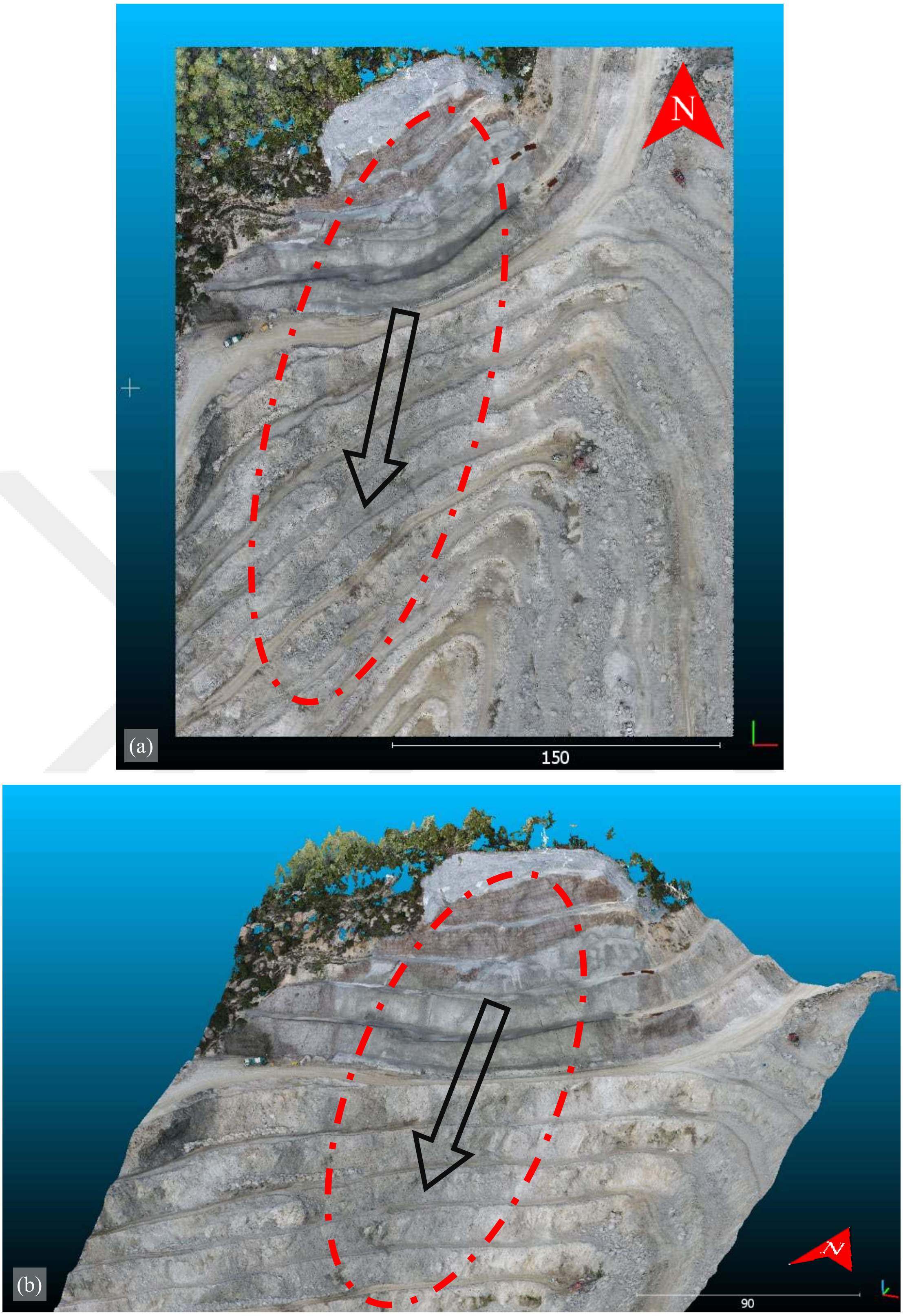

Figure 3.8 Plan (a) and a perspective (b) view of the cropped February 2018 initial surface model and landslide area

3.3.4.1 February 2018- March 2018 Terrain Surface Comparison

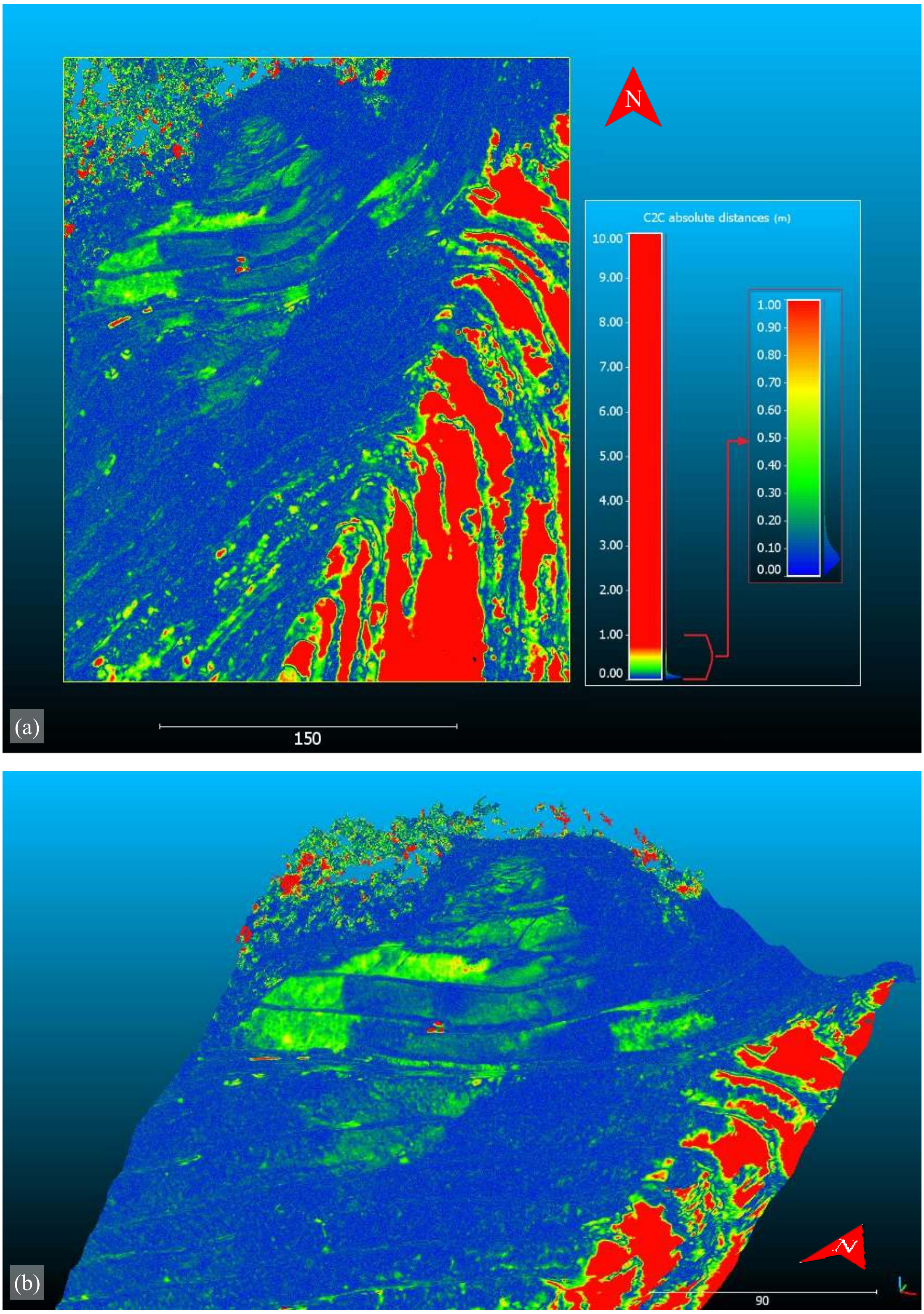

Figure 3.9 Plan (a) and a perspective view (b) of the February 2018- March 2018 cloud to cloud 3D comparison matrix

3.3.4.2 March 2018- April 2018 Terrain Surface Comparison

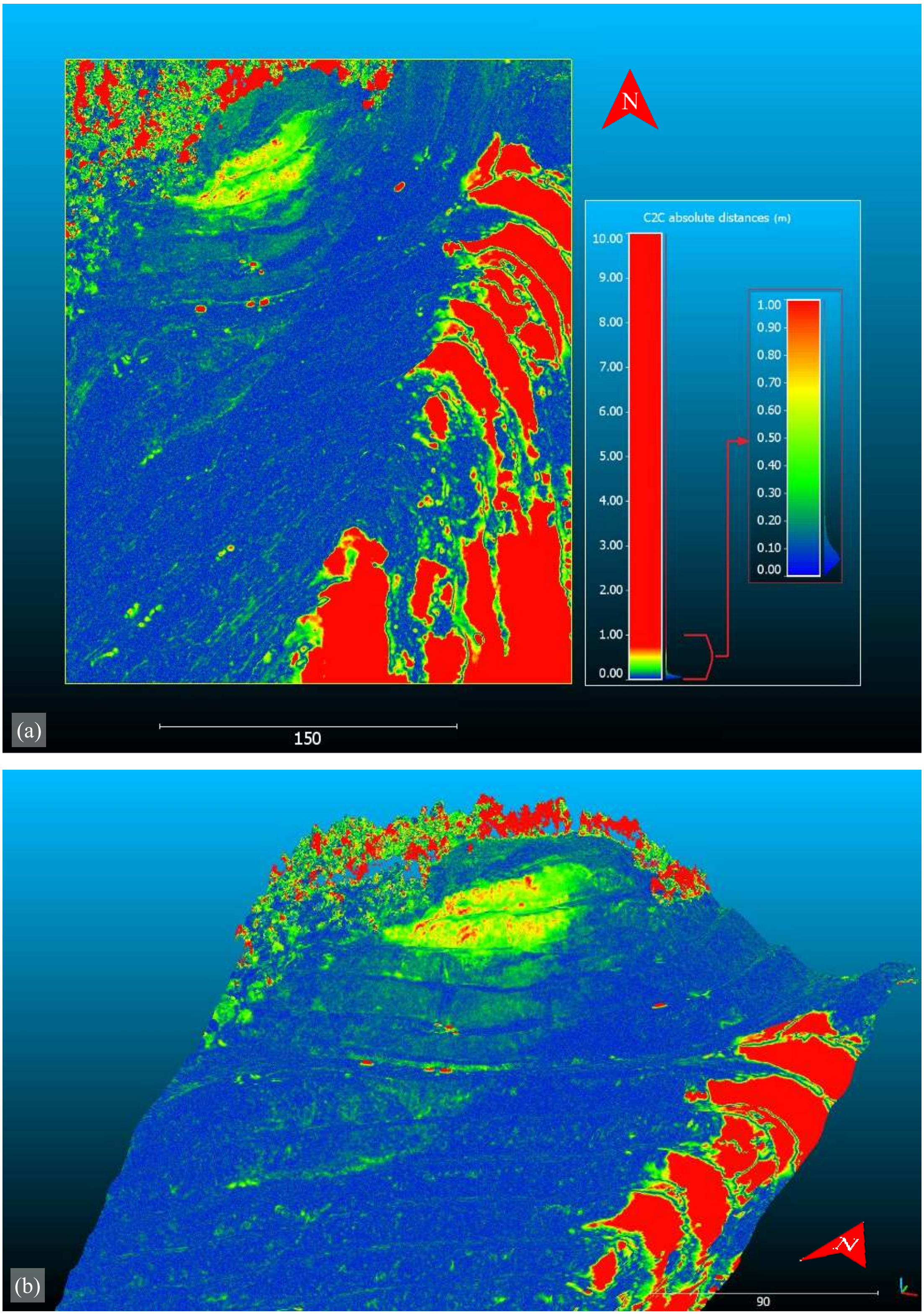

Figure 3.10 Plan (a) and a perspective view (b) of the March 2018- April 2018 cloud to cloud 3D comparison matrix

3.3.4.3 April 2018- July 2018 Terrain Surface Comparison

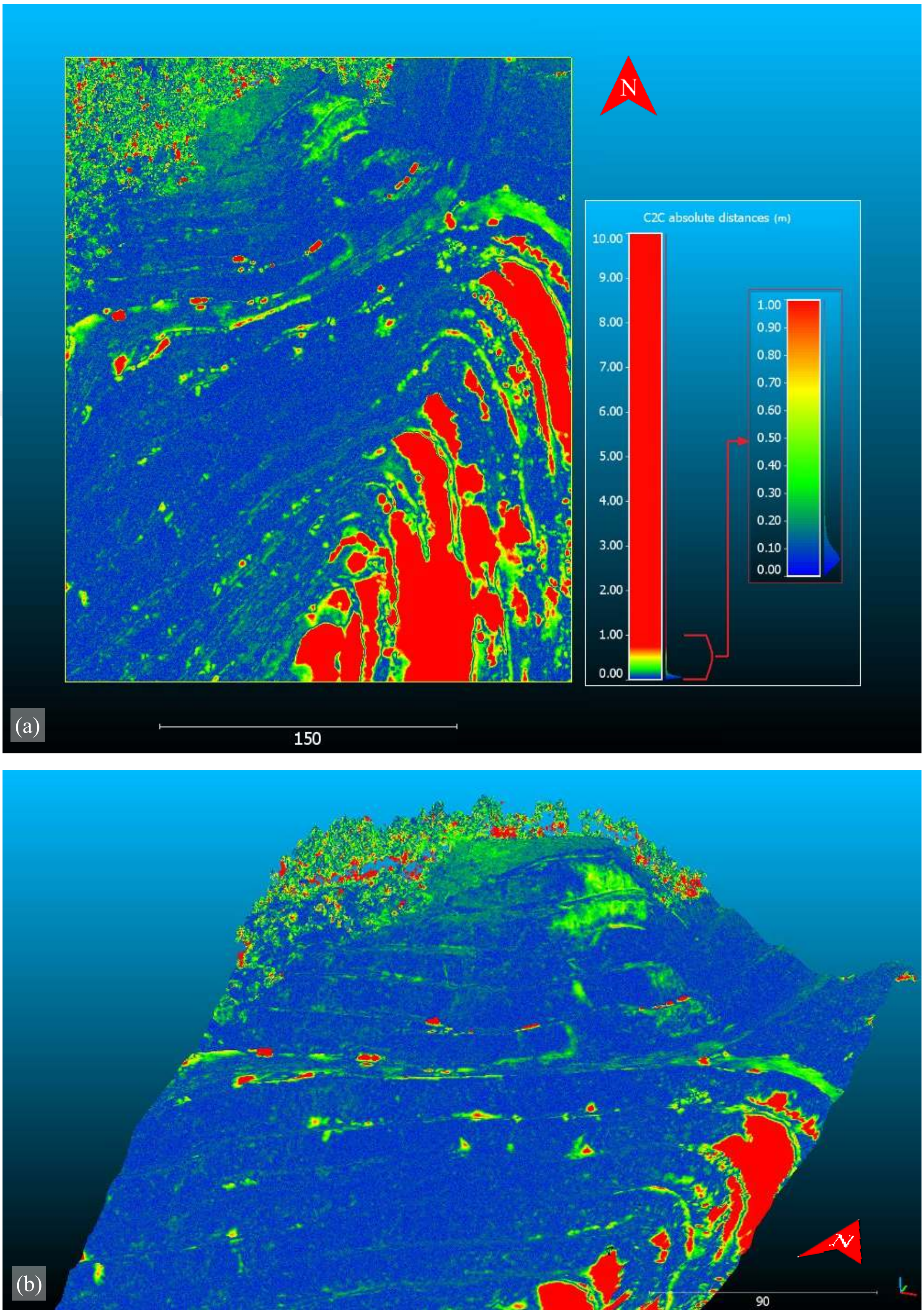

Figure 3.11 Plan (a) and a perspective view (b) of the April 2018- July 2018 cloud to cloud 3D comparison matrix

3.3.4.4 July 2018- February 2019 Terrain Surface Comparison

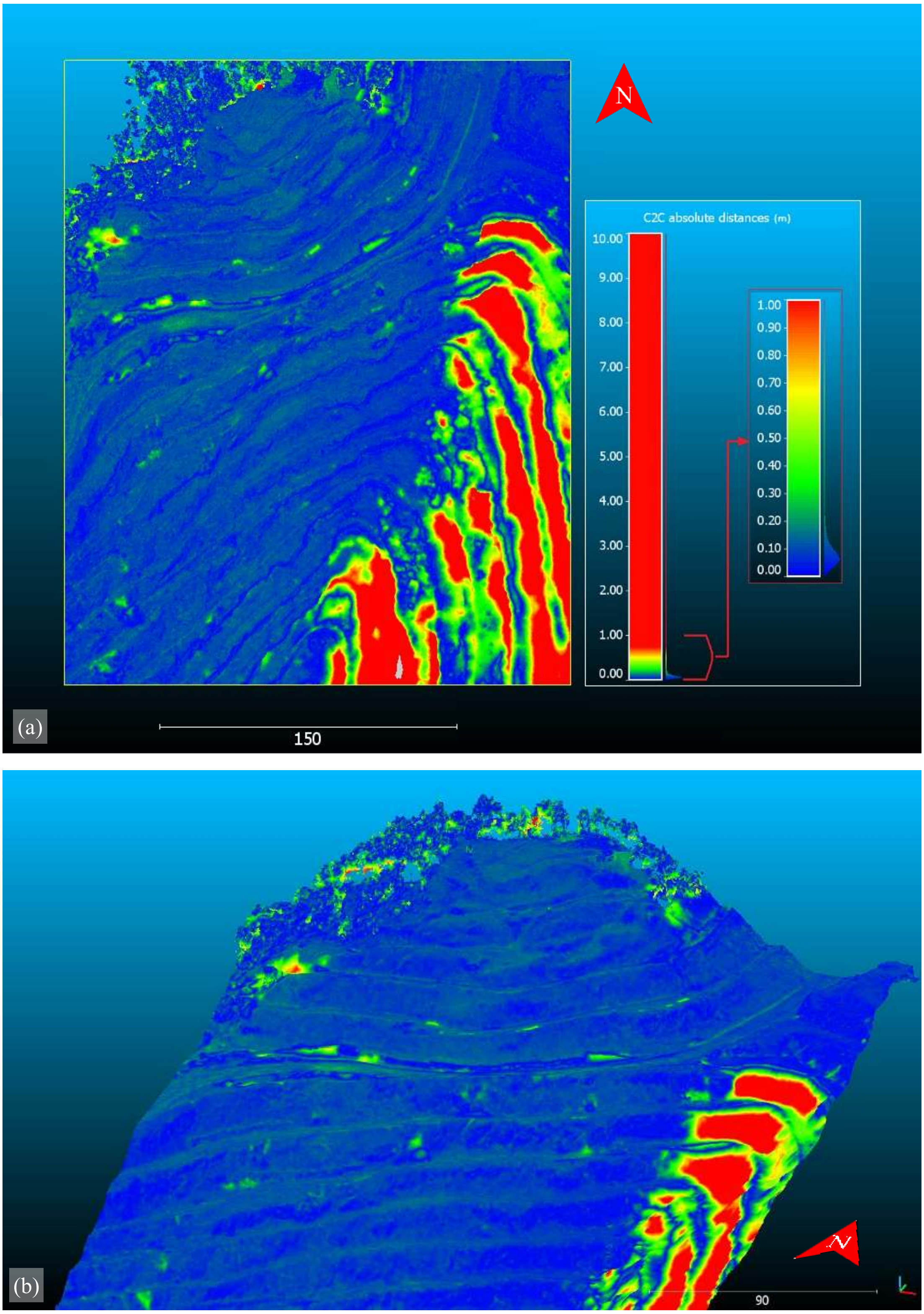

Figure 3.12 Plan (a) and a perspective view (b) of the July 2018- February 2019 cloud to cloud 3D comparison matrix

3.3.5 Interpretation of the Time-Dependent Monitoring

In the field observations, traces of landslide were easily seen. However, the broad area of the field created difficulty in visualization. For this purpose, the difference matrices obtained by the comparison of UAV supported surface models were very useful for understanding the landslide characteristic. In addition, visualization of these 3D matrices with a color scale is an important feature.

The images in Figure 3.9-Figure 3.12 show the 3D difference matrices. In plan images (a), the displacements around 1 m and larger are shown in red according to the histogram. In particular, the intensive red areas in the east-southeast of the site are the result of the operation in mining excavation. Looking at all the figures, it is clear that there is a continuous process in the same region. If we look closely, since there is no excavation of the haul roads in these regions, it is seen that these regions are not red.

The yellow zones show ~65 cm, and the green zones show ~40 cm displacement. It can be said that these colors are concentrated in the east-southeast for all comparisons. Also, there is a region in the northwest where red-yellow and green are intensive. As seen from the dense point cloud in Figure 3.8, vegetation in the region is quite dense. Trees that could not maintain their position because of wind caused the surface model seen in Figure 3.8 to deteriorate. This deformity creates the perception that there are many displacements seen in other figures. However, this region is not subject to landslide-related issues.

The blue-colored areas represent the regions where there is little or no displacement. The comparison images show that the blue regions cover the largest area. This can be seen from the density function graph to the right of the histogram. This point is significant here: the dominance of the blue zones (i.e., zero displacements) seen throughout the site is the validation that two surface models are placed correctly on top of each other for comparison. Because the areas where no operation is performed are known by the researchers.

.

3.3.5.1 February 2018-March 2018 Terrain Surface Comparison

In Figure 3.8, the landslide area is marked according to the observations. In Figure 3.9, the dense green areas are seen in 3 palaces in the northwest region, one of which is approximately 75 m and the other 50 m wide on three benches (Figure 3.13). The reason of this is the application of shotcrete projected as the first step of elimination of the displacements caused by non-deep slipping. When the histogram is examined, it is seen that an application of approximately 30 cm thickness is made here. Three small red dots in the same figure indicate the construction equipment (Figure 3.13). When the landslide area shown in Figure 3.8 is examined in Figure 3.9, a situation is remarkable. The formation of blue-green color is observed in a smooth ellipse (Figure 3.13). The reason for this is the displacement caused by slipping due to *seasonal precipitation*. In addition to these operations in CloudCompare software, displacements can be obtained at any point. The maximum displacement caused by the landslide in this region is 30 cm. The average displacement in the region can be said to be 10-15 cm according to the histogram.

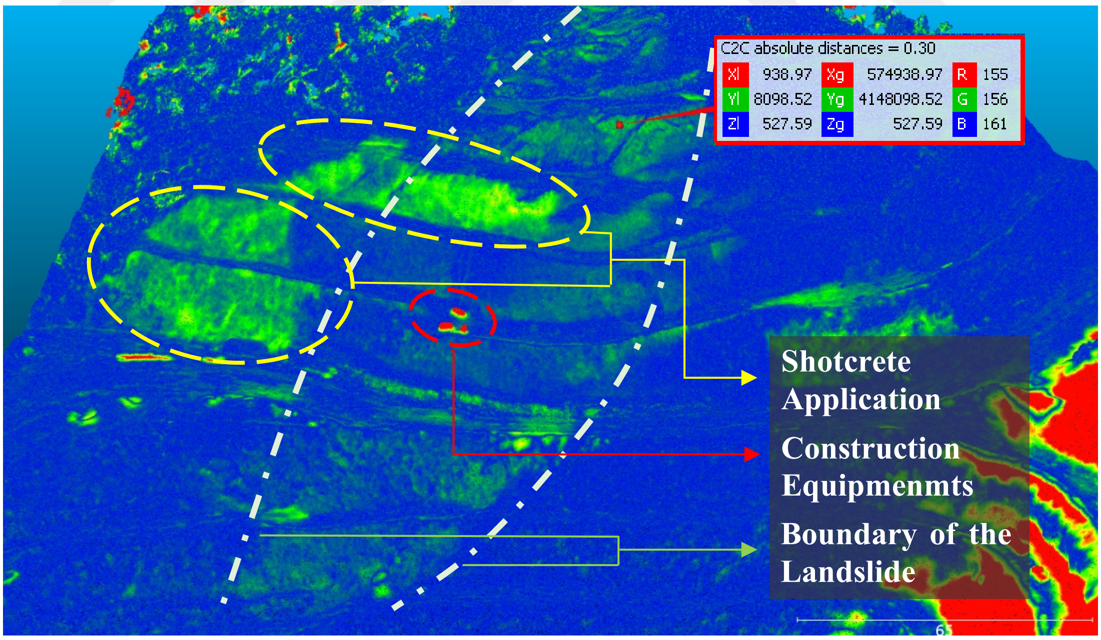

Figure 3.13 Definition of displacements on the February 2018-March 2018 comparison matrix

3.3.5.2 March 2018-April 2018 Terrain Surface Comparison

Figure 3.10 shows the apparent green-yellow traces on the upper elevations in the landslide area (Figure 3.14). It is due to the shotcrete application as in the previous comparison and is about 60-80 cm. On the other hand, construction machinery is seen in red. The landslide trace is again very prominent in this figure. Landslide traces are in parallel with the previous comparison. The direction of the landslide is not perpendicular to the benches, but it is seen that it moves with about 30°. It can be said that the average displacement in this region is 10-15 cm. The most significant displacement measured from the software is 32 cm (Figure 3.14).

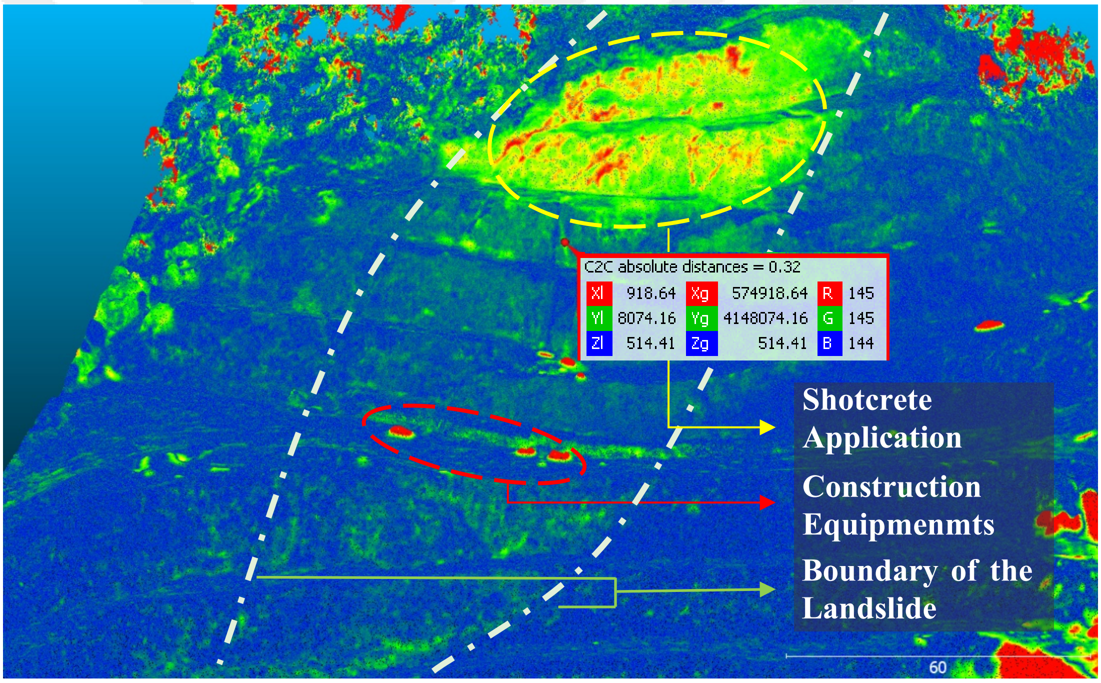

Figure 3.14 Definition of displacements on the March 2018-April 2018 comparison matrix

3.3.5.3 April 2018-July 2018 Terrain Surface Comparison

Figure 3.11 shows that there is no systematic behavior in the landslide area except for some local small green areas. Therefore, it can be said that the landslide has stopped. It can be thought that the reason for the landslide to stop is the shotcrete application, but this is not the case. The seasonal rainfall stopped during these three months shows that the landslide stopped seasonally. However, slope stability measures not yet taken at this date suggest that landslides may continue in the coming months.

3.3.5.4 July 2018-February 2019 Terrain Surface Comparison

This comparison period includes heavy rainy seasons, including autumn and winter. However, in Figure 3.12, there is no systematic displacement as in the previous period. The reason for this is that, within the scope of the project prepared by the Geotechnics Department of Dokuz Eylül University, precautions were taken with rock bolts in the light of 2D and 3D slope stability analyses which is explained later in the thesis (Figure 3.15). The effect of stabilization can be seen in this comparison (Figure 3.12).

Figure 3.15 The application of the shotcrete and rock bolts on the bench surface (Personal archive, 2019)

CHAPTER FOUR
LITHOLOGIC AND TOPOGRAPHIC MODELLING FOR FINITE ELEMENT ANALYSES

4.1 Overview

The landslide mechanism of most natural landslides is not simple enough to be carried out in two dimensions. The effect of the ground on both sides of the slip surface creates an arching mechanism against sliding. This resistance is developed based on the shear strength parameters of the soil. The spatial change of soil properties within the soil structure directly affects the sliding mechanism (Hicks & Spencer, 2010). In the 2D profile sections, the out of the plane wide sliding surface is represented as a line. For this reason, the effect of the contacted soils around the sliding surface cannot be fully reflected.

By performing the analyses in 3D, the geometry of the slide can be modeled more realistically. Besides, performing 3D analyses by the finite element method eliminates the need for selecting the most pessimistic section for shear. Because in this method, the landslide occurs at the point where the applied shear stress overcome the soil shear strength (Griffiths & Lane, 1999). In addition to the most pessimistic cross-section determination, the slip geometry is calculated, although slip is not yet formed. In other words, 3D analyses are more realistic approaches for landslides in complex areas (Alkasawneh et al., 2008).

Good modeling of the geometry of the object in 3-dimensional analysis in all kinds of engineering applications increases the quality of the analysis results. In slope stability analysis, the results are more reliable by increasing the detail of the geometry of the terrain, which is the main object for slope stability analysis. However, in today's technology, there are still problems in the computational time for 3D computer analysis. Performing analyses with the high-resolution field surface model increase the time spent. This causes many practitioners to prefer 2D software instead of 3D.

However, with the further development of computer technology, analyses can be performed faster and, more detailed analysis results can be obtained.

In this study, finite element analysis was performed to eliminate the stability problem occurring on the slope of the open-pit mine. For that purpose, the high-detail topographic model, which was established by images taken from an unmanned aerial vehicle, was used to create a finite element model. However, the high detailed topographic model can exceed the capacity of the finite element software. In this chapter, the optimization of 3D mesh surface model, which is appropriate for finite element analyses, is described.

The soil and rock units of the site and their parameters were predicted from the borings and inclinometers. The 3D finite element model was established by using the topography and predicted 3D shapes of the lithologic units by using PLAXIS 3D. In the context of this study, the emphasis is given on the establishment of the 3D finite element model, which has good mesh quality and reasonable calculation time.

4.2 Generation of the Lithologic Model

Field observations and inclinometer data are presented in detail in Chapter 2. In this context, as a result of the readings taken from 14 boreholes and 6 inclinometer wells and evaluations made in the light of topographic surface surveys and observations, the lithologic units in the mine site and the moving mass were evaluated and the boundary surfaces of the lithologic units to be used to form the finite element model were created in AutoCAD software. As shown in Figure 4.1.a, the red surface is the sliding mass, the gray surface is the mica-schist layer, the blue surface is the quartzo-feldspar unit, the green surface is the feldspar unit, and the other is the gneiss unit. The sliding mass is composed of quartzo-feldspar unit bounded by mica-schist layers. Since a thin mica-schist layer delimits the western boundary surface of the sliding mass, this surface is not formed as a separate unit; the effect is modeled using the interface in the finite element model. The units placed on the surface topography are shown in Figure 4.1.b.

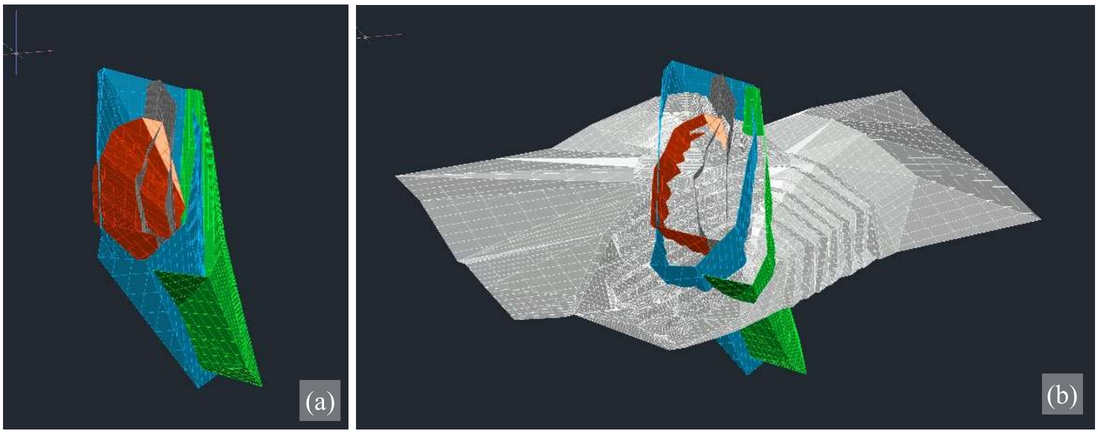

Figure 4.1 Lithologic units in the landslide area (a) and the surface topography model (b)

4.3 Generation of the Topographic Surface Model

The first surface model, February 2018, was used in the analyses to be performed in the finite element software. Although this model is older than the other models, the deformations do not affect the analysis. However, the model is already a point cloud. PLAXIS 3D, the finite element software for slope stability analysis, accepts mesh models consisting of 3D closed polygons in FEM creation. For this purpose, a mesh model is automatically generated from the dense point cloud in Metashape software (Figure 4.2).

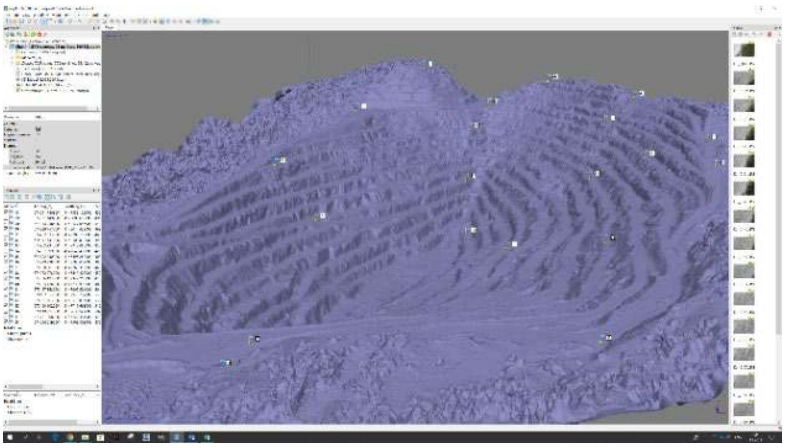

Figure 4.2 3D mesh model of the mine site

The dense and complex structure of the vegetation area reduces the suitability of the model for finite element analyses. In the preliminary studies made with the finite element software, this complex structure in the field caused errors in the geometry creation process and caused it to stop. As a solution to this problem, it is aimed to reduce the dense mesh complexity in the vegetation areas. In other words, it was desired to simplify the appearance of the model in this region. Since this simplification process is not performed in a critical area for stability analysis and only reduce the roughness without changing the overall structure of the surface, the analysis results will not be affected. In the PLAXIS 3D finite element software official promotional video, it was proposed to reduce unnecessary details of the model, to simplify the model as much as possible and to reduce the roughness as it improves the software performance (Bentley Geotechnical Engineering, 2016). In order to determine the optimum polygon number of the surface model to be used in the finite element software and to investigate the effect of roughness, the surface model was modified with different operations, and the response of the finite element software was investigated.

4.3.1 Optimization of the Surface Model

Since the bottoms could not be clearly visualized in the vegetation areas photographed by unmanned aerial vehicles, it was observed that gaps were formed in the dense point cloud model created with Agisoft Metashape software. The existence of any gaps on the surface model is an obstacle for the creation of the terrain model in the finite element software. The gaps in Figure 4.3.a are the areas that appear gray in the green bush. In the mesh model created later, it was observed that these gaps were reduced or even entirely removed by the software (Figure 4.3.b). However, with the observations made on the mesh model, it is not possible to make sure that all gaps are closed precisely, and the "close holes" command of the software can be used.

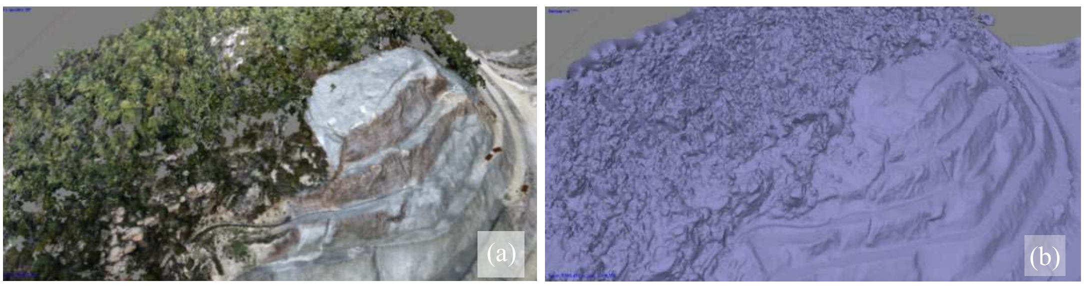

Figure 4.3 Dense point cloud (a) and gap status of the mesh model (b)

In Agisoft Metashape software, the surface roughness reduction process is performed with the “smooth mesh” command, which can reduce the roughness of the model entirely or partly. The number of polygons does not change in the smoothing mesh process. Decreasing the number of polygons is done by the “decimate mesh” command. With this command, the software can reduce the polygon number of the model, ie, its resolution to the desired extent.

Within the scope of the research, to show the effect of the model mesh status on the finite element analysis performance, five different surface models were created that were modified according to the number of polygons and the way they are formed. Features of the digital surface models (DSMs) are as follows:

DSM1: This is the direct export of the mesh model created in Agisoft Metashape software, and no modifications have been made on it. It is the surface model with the highest number of polygons and the most complex structure (Figure 4.4).

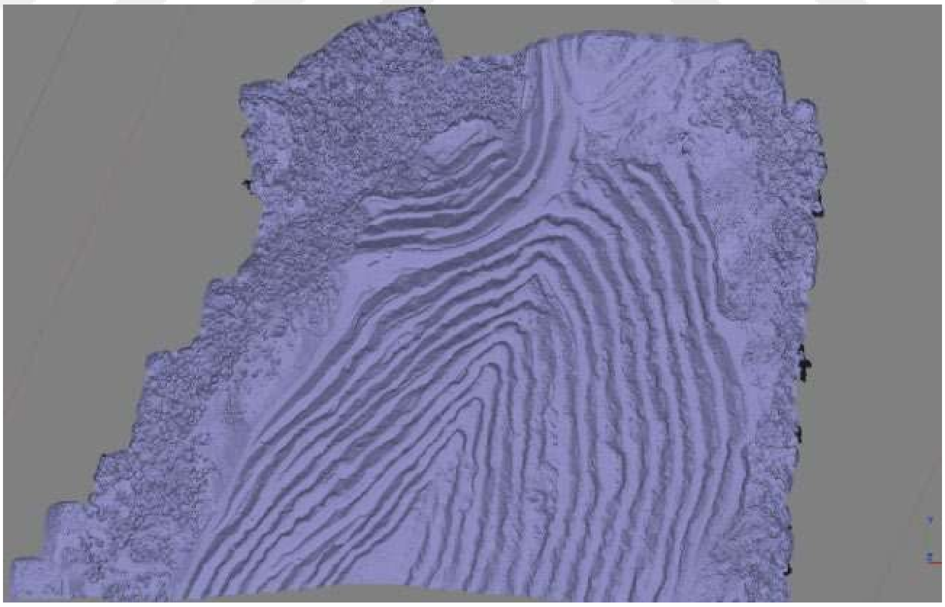

Figure 4.4 Direct exported DSM1 surface model

DSM2: The mesh model is the model which is roughness reduction applied in vegetation regions only. The intensity of the filter used in the roughness reduction process was selected as 1000. No changes have been made on it except for the roughness reduction process. It is the second model which have the most complex structure (Figure 4.5).

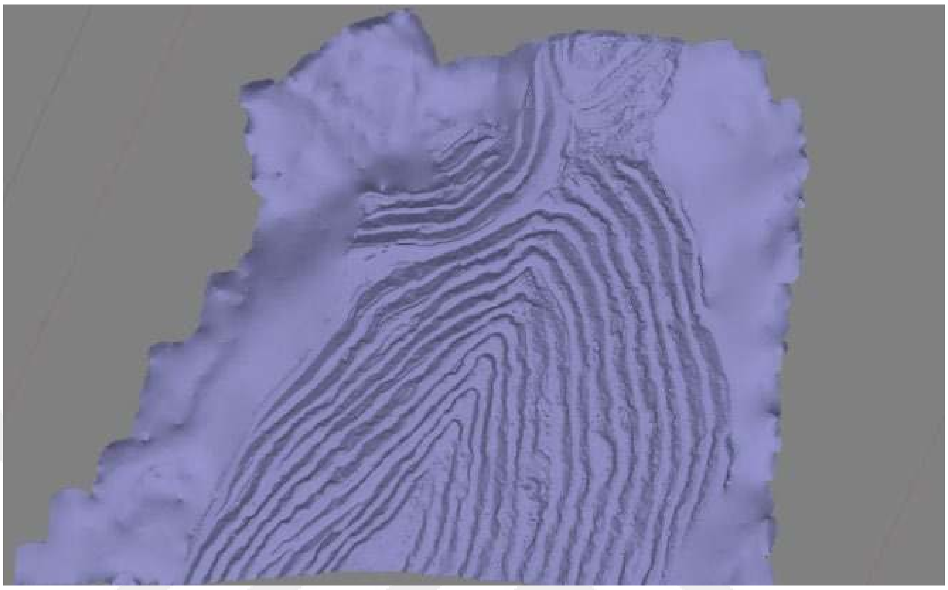

Figure 4.5 Smoothed vegetation area DSM2 surface model

DSM3: This model is a version of the mesh model created in Agisoft Metashape software, which reduces the number of mesh with the software feature. The number of polygons was reduced to 5000. The intensity of the roughness reduction in the vegetation areas was chosen as 1000. It is the third surface model with the highest number of polygons and the most complex structure (Figure 4.6).

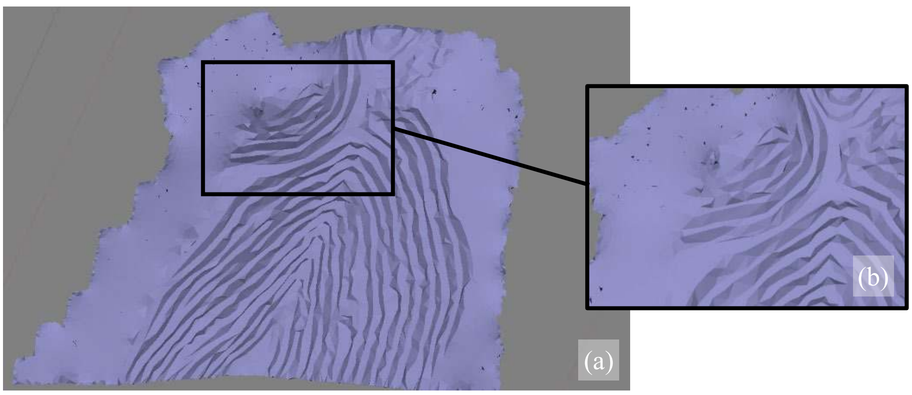

Figure 4.6 DSM3 surface model (a) and zoomed image (b) with mesh reduction and roughness removal in vegetation areas

DSM4: This model is a surface model created by using polygons formed by pointing critical locations such as bench toes and crests on point cloud in Agisoft Metashape software and manually combining these points with three-dimensional faces in AutoCAD software. In this pointing process, the general condition of the land is reflected by ignoring the details. It is the surface model with the least polygonal number and the simplest structure (Figure 4.7).

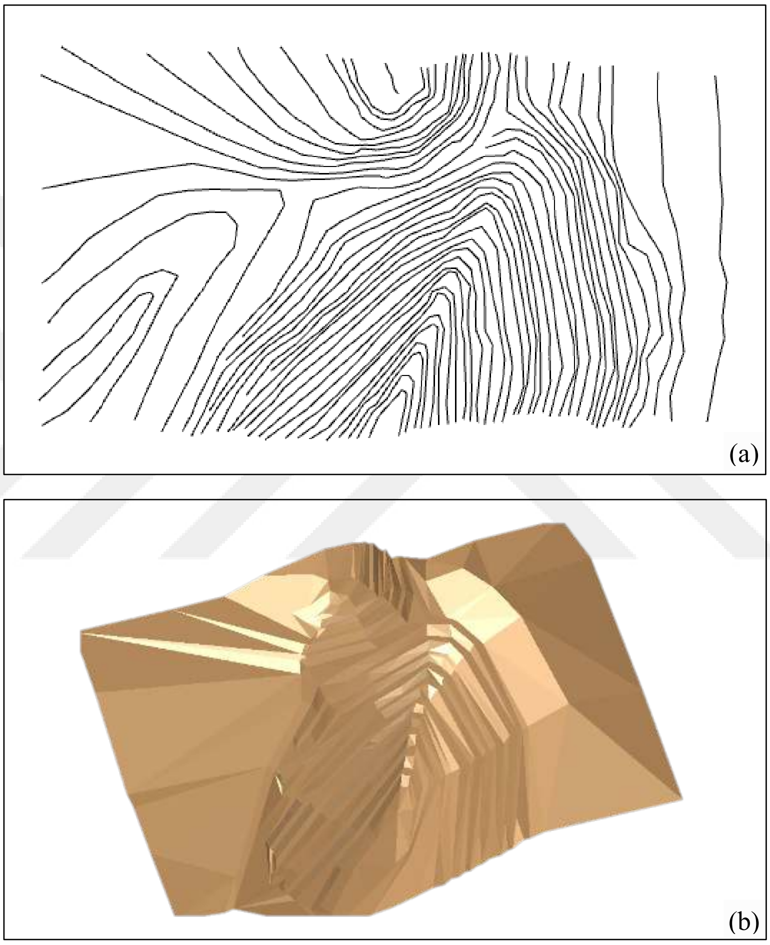

Figure 4.7 The polygons created by manual marking (a) and the DSM4 surface model formed by manually combining these polygons with 3D faces (b)

DSM5: This model was created using the polygons in Figure 4.7.a as the DSM4 model. However, the difference is that the mesh structure is automatically generated by Rhinoceros 3D, which is a 3D CAD software. In addition to creating the model in a very short time, triangular polygons are quite shapely (Figure 4.8). It has more mesh numbers than DSM4 model.

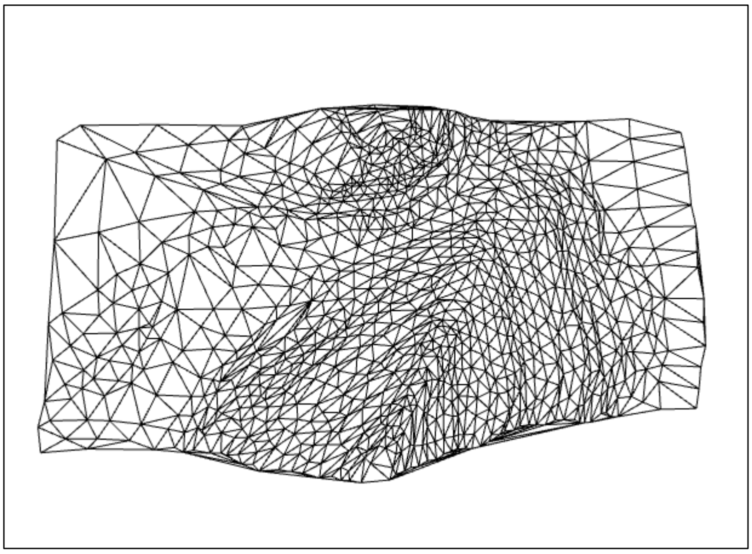

Figure 4.8 DSM5 surface model automatically created from polygons with Rhinoceros 3D

The five surface models created in this way were exported in "2004 dxf" format, as suggested by PLAXIS 3D software. The total number of polygons of the surface models' properties and a summary of their formation are shown in Table 4.1.

Tablo 4.1 Processes on creation of surface models and their number of meshes

Surface Models	Optimization Processes by the Images Processing Software		Optimization Processes by the Cad Software		Total Number of Meshes
	Smoothing	Mesh Decimating	AutoCAD (manual)	Rhinoceros 3D (automatic)	
DSM1					1755000
DSM2	✓				1755000
DSM3	✓	✓			5000
DSM4			✓		645
DSM5				✓	1870

4.3.2 Selecting the Most Appropriate Surface Model

Three-dimensional finite element analysis was performed in PLAXIS 3D software. DSM1, DSM2, DSM3, DSM4, and DSM5 surface models were used in the preliminary analysis to determine the optimum surface model. The surface models were transferred to the software, and geometry creation operations were performed. Due to the complex structure of geometry, system performance has decreased in some models, even the transfer to finite element software could not be performed. With these results and observations, the most suitable surface model for the field finite element analysis was selected. Comprehensive slope stability analyses were made with the selected surface model, and a separate research was carried out for the selection of the most appropriate slope stability measure.

In the analysis performed in PLAXIS 3D software, the general workflow, which will be explained in the next chapter, is as follows:

1) Transferring the surface model to the software,
2) Forming the terrain finite element model,
3) Formation of lithologic units and assigning material to units,
4) Establishment of mesh model and determination factor of safety,
5) Creation of structural solutions to ensure stability,
6) Performing the analyses.

In the finite element software, preliminary studies were carried out on PLAXIS 3D software in order to select the most appropriate surface model of the terrain where the analyses will be performed. In the preliminary studies, the surface models were compared according to the ability to transfer the surface model to the software and the system performance in the finite element model creation process. The selection of the appropriate surface model was made according to the first two items of the workflow.

The preliminary analyses show that system performance was low in every process performed on the DSM1, DSM2, and DSM3 finite element model in PLAXIS 3D software. The complex and dense mesh situation on the surface caused this. In the DSM4 and DSM5 models, which were created manually by using points taken from the terrain model, no systemic errors were encountered, and no decrease was observed in performance. The low number of polygons and the minimum complexity of DSM4 and DSM5 surface models are the primary factors contributing to software performance. Furthermore, since DSM4 is manually formed, the desired level of detail can be achieved in the desired regions. Apart from these advantages, the disadvantage for the DSM4 model is the time spent manually creating the surface model. The DSM5 model is superior to DSM4 since it can be created within seconds, except for the forming critical point polygons. On the other hand, in terms of the completion time of the analyses, simple models have great advantages. Besides, it is considered that the transfer of surface models of PLAXIS 3D directly to the sites with simple topography is not a problem. It means that there is no incompatibility between Metashape and PLAXIS 3D.

As a result of the studies, the terrain finite element model could be created appropriately with DSM4 and DSM5 surface models. Although the level of field detail is not high, they have enough detail in terms of analysis. Although DSM5 has a high degree of automation, the finite element analysis described in the next section was performed on the DSM4 surface model, since the performance of the DSM4 model with a smaller number of polygons is relatively high.

CHAPTER FIVE
FINITE ELEMENT MODELLING OF THE MINE SITE

5.1 Introduction

2D slope stability analyses are frequently preferred as a classical and practical method in slope stability studies. In recent years, with the development of aerial imaging methods, the ability to create high-resolution terrain surface model has paved the way to 3D geotechnical analysis since structural and topographic characterization. Therefore, formidable task with conventional surveying techniques has become a much easier operation with digital processing of the images acquired by unmanned aerial vehicles. In addition to the fact that the terrain topography can be quite satisfactorily reflected in 3D slope stability analysis, slope stabilizing structural members such as rock and/or cable bolts can also be mapped in a 3D model in greater detail compared with 2D modeling. While a slope stabilizing geotechnical element can only be represented in a 2D model by its length, elevation, and the angle with horizontal, a 3D model enables full characterization of both the geometry and structural elements.

In a 2D analysis, a case is idealized as a plain-strain problem. However, a landslide very rarely poses 2D features. One should note that forces imposed on slope stabilizing members are highly location-dependent, and a 2D model may be not capable of producing reliable results for 3D complex geometries.

In recent years, there has been an increase in the geotechnical software that perform three-dimensional slope stability analyses using either limit equilibrium methods (Svslope, Slide3D) or finite element and finite difference methods (Plaxis3D, Flac3D, GtsNx). In this context, Zhang et al. (2008) compared the 2D and 3D slope stability analysis results. 3D analyses were performed with Svslope, which is a software that uses the limit equilibrium method. In the study, the effect of shear strength parameters, groundwater conditions, and terrain topography on 2D and 3D slope stability analysis results were investigated. It is obtained that as the slope inclination increased, the differences of factor of safety values between the 2D and 3D analyses were also increased. In addition, it is observed that the difference in the factor of safety was increased with the increase of the shear strength parameters. Alkasawneh et al. (2008) have used commercially available programs to investigate the change of factor, safety (LE, FE, Linear Grid Methods, Rectangular grid methods, Monte Carlo Searching Techniques) in 2D and 3D analysis. It carried out the analyses in Sas-Mct, Utexas3, Stabl5m, Plaxis2D and Plaxis3D. He said that the limit equilibrium method would be sufficient for lands that have simple geometry and non-complex ground boundary conditions.

3D modeling makes the analyses more reliable and realistic, but such an approach brings along some disadvantages. For instance, the engineer is required to employ rather sophisticated mapping techniques in defining the start-end coordinates of a geotechnical element, whereas it is a relatively simple task in 2D modeling.

Rock and cable bolts are two of the most commonly used slope stability measures proven to be effective in practice (Zhang, Lu, & Cheng, 2008). Rock bolts penetrate from the terrain surface to the soil behind the sliding surface and increase the shear resistance on the slip surface. On the other hand, cable bolts (i.e., anchors), similarly apply anti-sliding force by supporting the soil surface with the cable that is plugged into the ground behind the sliding plane. Therefore, they change displacement and stress on the ground by applying resistance to sliding force. In order to design the stabilizing members properly, the studies should be supported by field monitoring, laboratory experiments, numerical modeling and analytical analyses (Li & Stillborg, 1999).

Slope stability analyses with rock and cable bolts are usually carried out by 2D numerical analysis methods such as other analyses and mostly by the Finite Element Method, which generates comprehensive output data. In FEM, stabilizing line members (cable and rock bolts) are quickly formed on the idealized profile by defining the start-end points and the angle with the horizontal. The lateral spacing between the stabilizing elements is added to these data to be ready for analysis. However, only one type of stabilization element is modeled in terms of geometry. If the site has a large area and complex stratigraphy, this results in insufficient construction for a single section. To eliminate this problem, the analyses to be made on the different sections may reduce this problem to some extent, but do not produce an output with co-operation of the bolts. The interoperability of stabilization elements can be modeled as 3D analyses in a more realistic way. Thus, it is possible to model the elements in different lengths and angles and in different lateral spacing.

In contrast to 2D analyses, the creation of the geometric position and the calculation of arraying properties of rock bolts and cable bolts in 3D numerical slope stability analysis become difficult due to the 3D drawing conditions on a software interface. The main reason is the depth complexity in 3D modeling. It is necessary to make some acceptances for the application direction so that these elements can be quickly and effectively created and reproduced.

In the literature, there are many geotechnical case-studies and parametric studies carried out with commercial programs using 3D finite element methods besides slope stability. In particular, these programs are frequently used in tunnels (Dehghan, Shafiee, & Rezaei, 2012; Janin et al., 2015) and foundation design (Kim & Jeong, 2011; Pradhan, 2012). In these studies, in three dimensions, both in slope stability and in other engineering applications, the terrain surfaces were generally analyzed as simplified surfaces. In real cases, the field surfaces contain much more detail. This study differs from these examples in terms of land complexity and area size. Also, rock and cable bolts were applied in the sliding region on our finite element model to prevent slippage in the field. For this purpose, the methodology followed to map rock and cable bolts that would serve as slope stabilizing members in a 3D finite element model is presented.

5.2 Creation of the FEM

The formation of the finite element model of the open mining area is examined as two titles. The first one includes the formation of topography and lithological units and the assignment of the soil strength parameters to these units. In the previous section, DSM4 model was selected as the surface model representing the topography. The second title is the placement of cable and rock bolts applied to stabilize the sliding mass.

5.2.1 Generation of Topography and Lithology

Surface models do not have thickness and volume. The models are used in PLAXIS 3D software for the intersection of geometric objects such as a cube or rectangular prism to form a finite element model.

The lithological unit models have been previously created according to the data obtained from drilling and inclinometers in AutoCAD for the mica-schist, feldspar, quartzo-feldspar, gneiss units and shear surface. These models have been generated in accordance with the global coordinate system. Thus, the field surface and units can be positioned in the correct method when transferred to the same drawing environment (Figure 5.1). This structure, which consists of the surface model and the lithological units, is called a field model. The first step is to import the field model to PLAXIS 3D.

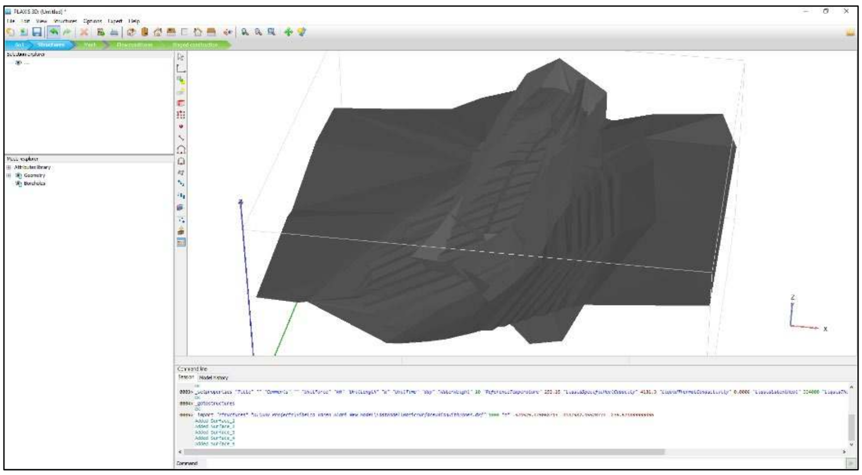

Figure 5.1 Field model imported to PLAXIS 3D finite element software

In order that the models of lithological units to cut the surface pattern clearly, the uppermost three-dimensional faces (3d face elements) were extended slightly higher (+ z-direction) than the surface model. There are 818 mesh elements in the whole model, which consists of 5 soil units and surface model. Although it forms the geometry of the whole field with ground units, it still has many less elements compared to the surface models DSM1, DSM2, and DSM3.

In the preliminary studies, the field model was shifted from the actual coordinates to a region close to the origin in the importing process, since it has been realized that the finite element model provides a rich working opportunity during the geometry creation. The shift amounts are -574529.47m on the x-axis, -4147582.45m on the y-axis, and -239.57m on the z-axis. In the importing process, the model scale was kept the same as the actual scale. A planar polygon was created by drawing a closed polygon on the field model in the x-y plane (top view) within the boundaries of the model (Figure 5.2). Then, this polygon was extended 400 m in the direction of the z-axis to obtain 3-dimensional prism. This extrusion was carried out in the positive or negative z-direction so that the surface prism would pass through the surface model (Figure 5.3). Then, by selecting the surface model and prism, “intersect and recluster” command was applied. Thus, the prism was cut by the surface model, and two different volumes were formed. The 3-dimensional finite element model representing the topography of the terrain was created by deleting the upper volume (Figure 5.4). In order that the intersection process is carried out, the surface model must not contain gas or overlapping polygons. Otherwise, the PLAXIS 3D software cannot perform volume cutting. This was considered in generation of DSM4.

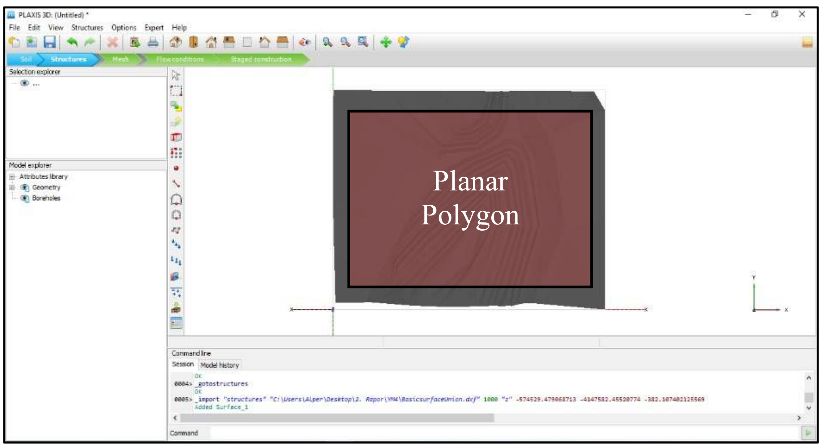

Figure 5.2 Top view of DSM4 imported to PLAXIS 3D and the planar polygon

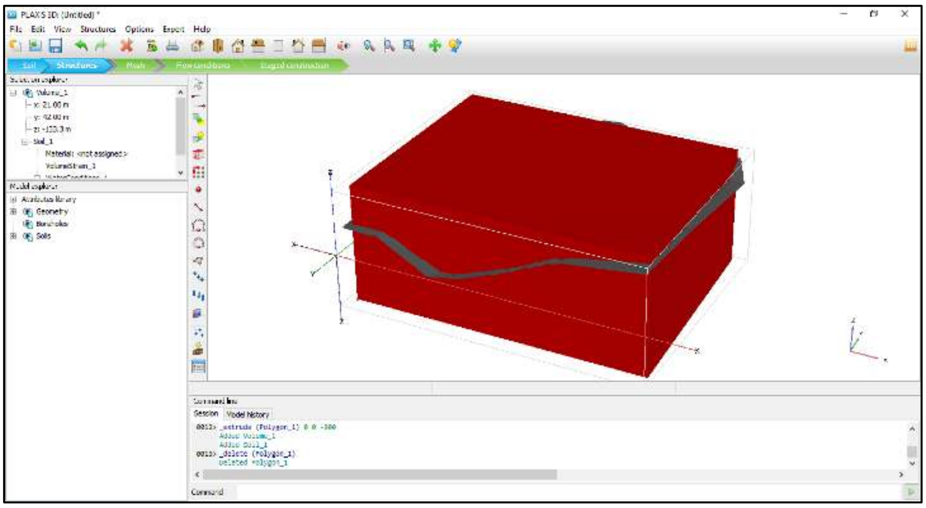

Figure 5.3 Rectangular prism obtained by extrusion in the z direction of the plane polygon

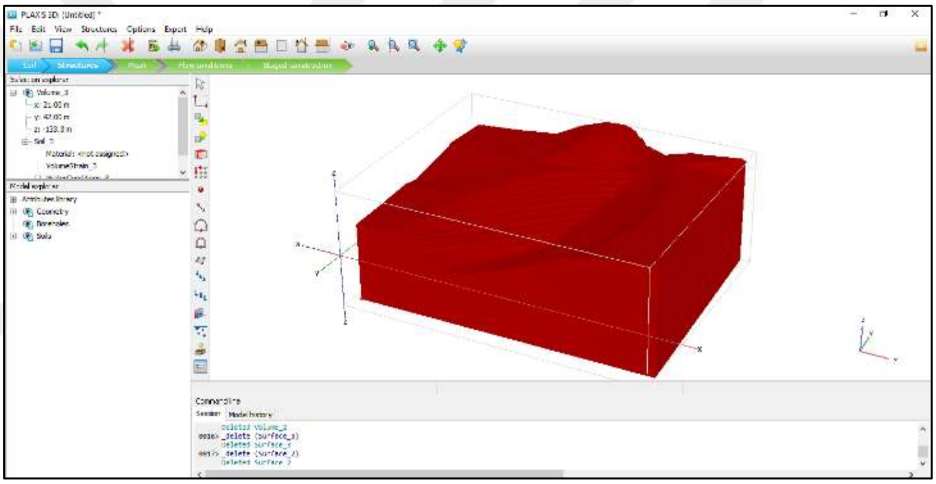

Figure 5.4 3D terrain finite element model obtained by prism and surface intersection

After the topography is created in finite element software, the process is to obtain lithological units. Each unit is a separate piece in order to create the lithological unit models separately in the finite element software (Figure 5.7). For this purpose, firstly, volume and quartzo-feldspar unit surface model were selected together, and "intersection" was applied to divide the model into two parts. The outer volume was then estimated by the surface model of the feldspar unit. Thus, gneiss (Figure 5.6.a) and feldspar (Figure 5.6.b) units are also separated from each other. In order to separate the inner parts, the volume mica-schist surface model and shear unit surfaces were estimated. In this way, the internal volume is divided into the corresponding mica-schist (Figure 5.6.c), quartz-feldspar (Figure 5.6.d), and shear mass (Figure 5.6.e) units.

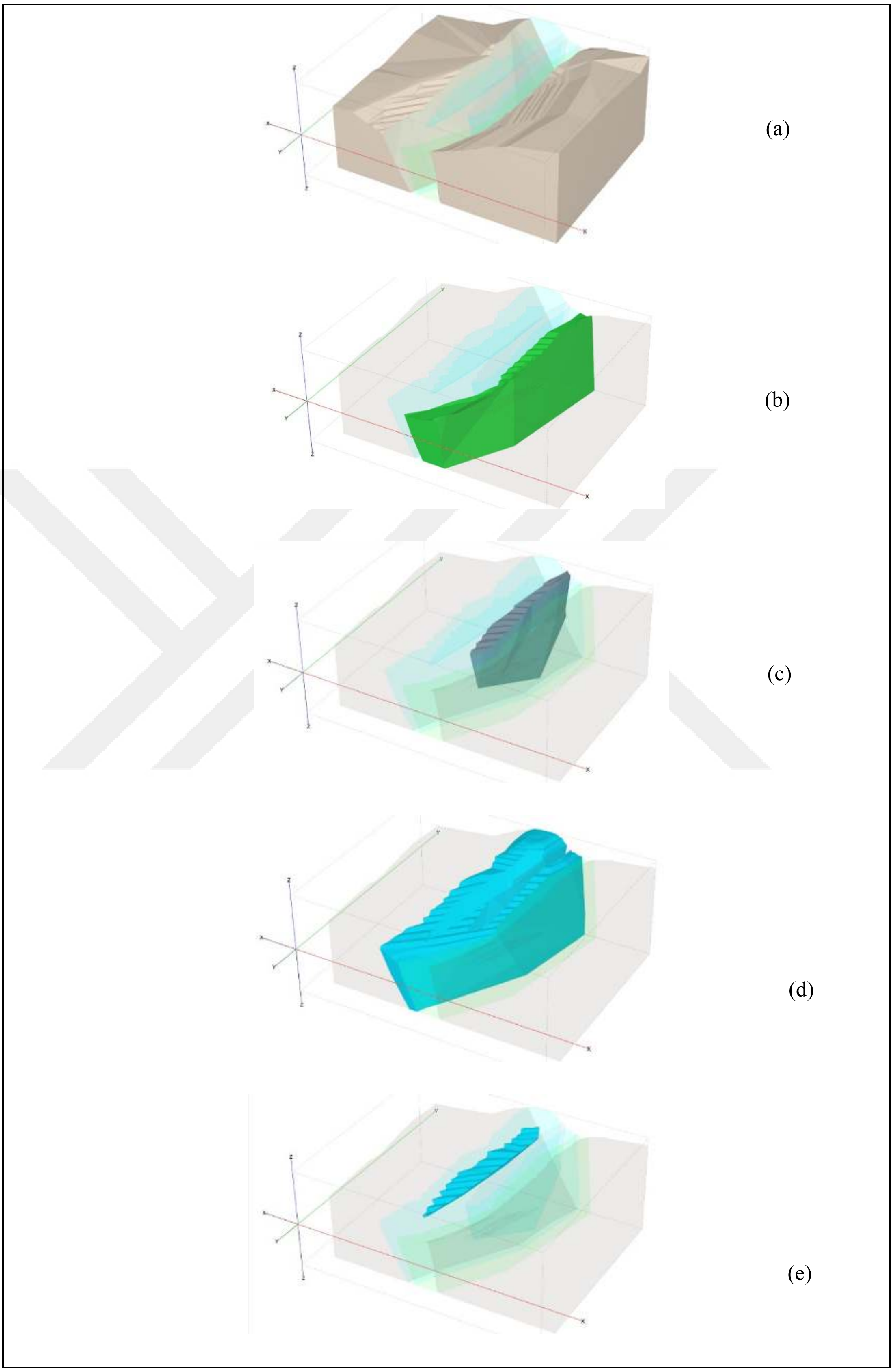

Figure 5.6 Gneiss (a), feldspar (b), mica-scist (c), quartzo-feldspar (d) units and sliding mass (e)

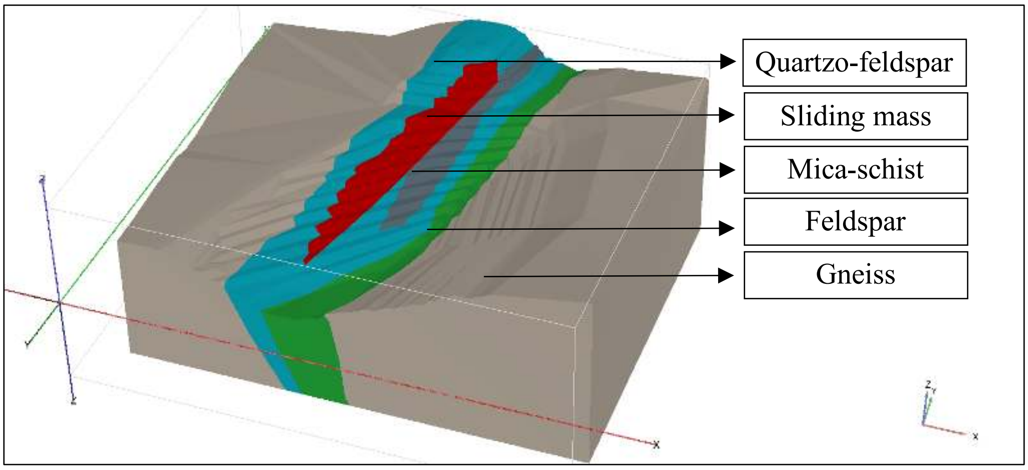

Figure 5.7 The finite element model and the lithological units

Table 5.1 The strength parameters of soil units

Material Properties	Feldspath	Gneiss	Quartz-Feldispar	Mica-Schist
Material Type	Mohr-Coulomb	Mohr-Coulomb	Mohr-Coulomb	Mohr-Coulomb
Drainage Type	Drained	Drained	Drained	Drained
Unit Weight (kN/m³)	26	26	21	20
Saturated Unit Weight (kN/m³)	27	27	22	21
Elasticity Modulus (kN/m²)	1.20E+06	2.20E+06	4.60E+06	1.50E+04
Poisson Ratio	0.2	0.2	0.2	0.3
Cohesion (kN/m²)	350	300	250	50
Internal Friction Angle	30°	55°	45°	34°

Soil parameters of the units in the field model to be analyzed by finite element analyses were determined by evaluating laboratory experiments and data in literature. This data was created as a material type by assigning to the units. The strength parameters of these material types are shown in Table 5.1. The material types thus formed are assigned to the relevant units.

The soil type of the sliding mass is quartzo-feldspar. However, there is a discontinuity plane at the outer boundaries of the unit and is represented by "interface" elements in the software (Figure 5.8). Interfacial coefficient was assigned in the ground units around the interfaces. These coefficient values provide a calculation of the parameters of the interface area by multiplying with this coefficient and assigning the lowest parameter values to the interface region. The interface coefficient in quartzo-feldspar material properties was entered as 0.1. By describing this property to quartzo-feldspar material, only the interface elements around the quartzo-feldspar material are affected. The sliding zone is in contact with the quartzo-feldspar unit and the mica-schist unit. It is, therefore, necessary to define the interface coefficient for the mica-schist material. The interface coefficient for the mica-schist is 0.5.

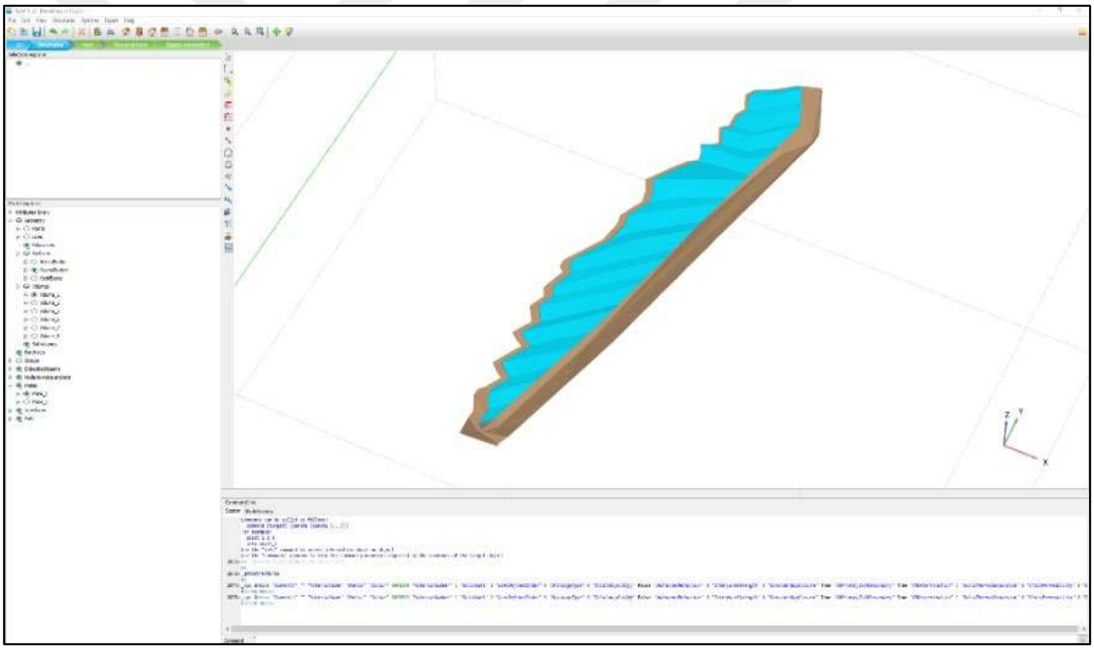

Figure 5.8 Sliding mass (blue) and interface element (brown)

5.2.2 Generation of Stabilizing Structural Elements on Finite Element Software

In the finite element software, the present state of the terrain structure was modeled by the creation of a terrain surface model and the assigning of the soil parameters to the lithological units. In addition, the problematic area was planned to stabilize with cable and rock bolt applications. The accurate modeling of these stabilization elements makes the finite element model quite realistic. However, as with many 3D geotechnical slope stability software, PLAXIS 3D does not allow direct mapping of these stabilization elements in the desired horizontal and vertical angles. In addition, the arraying command used for multiple stabilization element modeling also presents a challenge in such complex geometries.

In the 3D drawing environment, the depth complexity makes the manual drawing difficult. As a result, even if the first point of the stabilization element can be selected on the field surface during modeling of a linear element such as rock bolt or cable bolt on the software, the endpoint to be inside the ground cannot be marked manually. In other words, when a point can be marked on the surface, it is not possible to map a point inside or outside the soil volume as desired. For this reason, in this study, structural element top point coordinates were selected manually on the surface of the terrain, the endpoint coordinate points were not placed manually, they were mapped with the assignment of point coordinate data to software. Calculations of the endpoint coordinate of stabilization elements were calculated according to the top point coordinate, surface penetration angle, and element length.

In this study, a rock bolt application of FEM is shown as an example of methodology. The same methodology can be used for cable bolts or any linear element. The flowchart, which is followed in order to map rock bolts in 3D slope stability analysis, is shown in Figure 5.9. Each stage is described in detail.

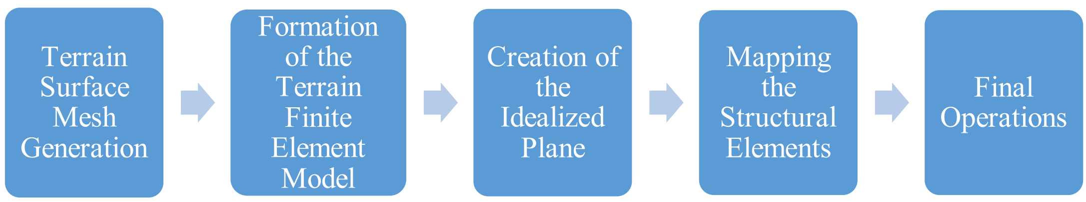

Figure 5.9 Flowchart of generation terrain finite element model with stabilization elements

5.2.2.1 Creation of the Idealized Plane

In most cases, the structural members are formed perpendicular to the surface (i.e., parallel to the normal vector of the surface) and parallel to each other in a row.

However, the angle of the surface may not be the same along the site. In this case, the elements cannot be mapped parallel to each other. Although parallelism can be provided an implementation in the field, in numerical modeling, it is necessary to make some assumptions for the parallel positioning of the elements.

In addition to the parallel placement of the structural elements, it is also vital that proper mapping according to the general surface condition. In this study, the terrain surface, on which the elements are placed, was represented as an idealized plane. Therefore, stabilization elements were mapped according to the normal vector of this plane. When selecting the idealized plane, the general topographical condition of the terrain where the elements will be mapped was considered (Figure 5.10).

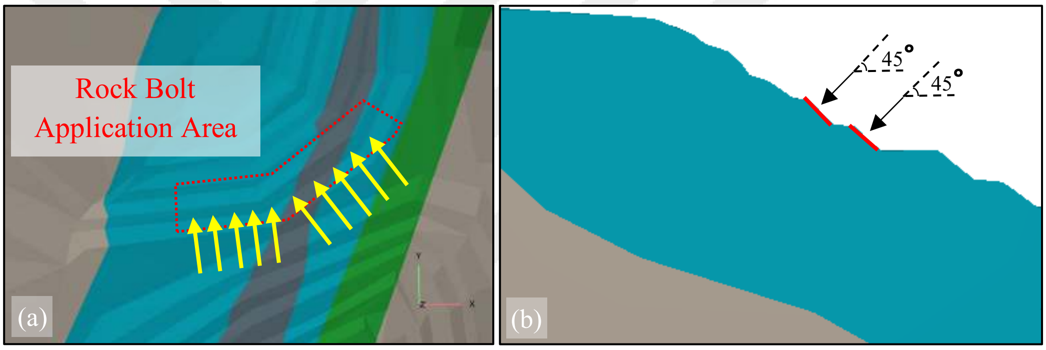

Figure 5.10 Rock bolt application area and their design of construction in plan (a) and profile view (b)

Since the surface structure characteristics in the region where the stabilization elements are placed change rigidly, the region was idealized with two different planes (Figure 5.11.a). The unit normal vector parameters of these idealized planes (IP) can be taken directly from the software (Table 5.2).

The top points of the stabilization elements were placed on idealized planes. Since the idealized planes are formed directly on the surface of the ground and some areas may remain in the ground, they were shifted from the terrain surface. Otherwise, the top points of the stabilization elements place inside the ground.

Table 5.2 Unit normal vector values and shift length in 3D of idealized planes

Number of Plane	Unit Normal Vector		Shift Length for 5m (m)	
	IP #1	IP #2	IP #1	IP #2
x	-0.0408	-0.3948	0.2038	1.9740
y	0.6084	0.5467	-3.0420	-2.7335
z	-0.7926	-0.7384	3.9630	3.6920

The shifting of the idealized planes was performed according to their unit normal vector. A displacement was made according to the values in Table 5.2 calculated by multiplying the unit with the normal vector values (Figure 5.11.b).

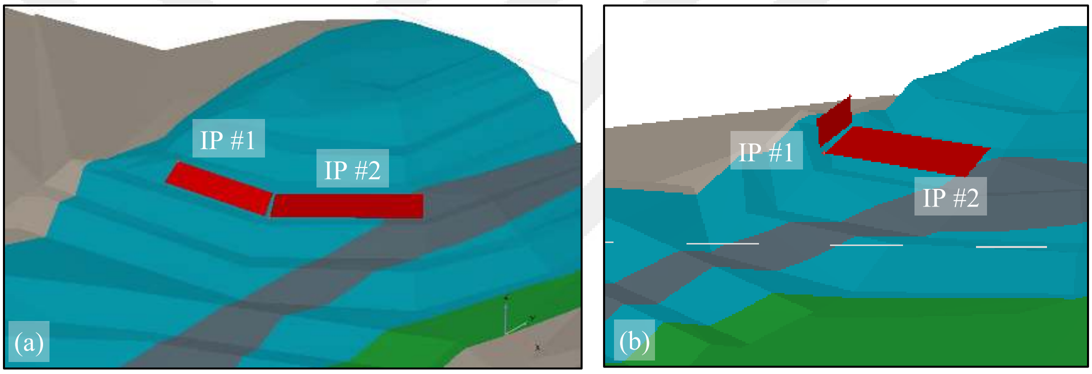

Figure 5.11 The idealized planes (a) and their shifted locations (b)

5.2.2.2 Mapping the Structural Elements

Since the structural elements were placed on the idealized plane and the idealized plane was shifted, an exceeding length of the elements remain between the ground surface and the idealized planes. For this reason, the length of the element was entered as a larger value than the actual length. This excess was removed as described later.

Rock bolt type stabilization elements used in this study were selected in lengths of 16 meters. So, the first element was formed with a 30 meters pre-dimension. For this, the first point of the element was placed on the shifted idealized plane. Then, in order to determine the coordinate of the other point, the coordinate difference values between top and endpoints were calculated with the following formulations depending on the normal vector parameters of the idealized plane:

$$\Delta y = \frac{\sin(\alpha) * y}{\sqrt{x^2+y^2}} * L; \quad (5.1)$$

$$\Delta x = \frac{\sin(\alpha) * x}{\sqrt{x^2+y^2}} * L; \quad (5.2)$$

$$\Delta z = -\cos(\alpha) * L \quad (5.3)$$

Δx, Δy, Δz : the coordinate difference between top and endpoints of elements
α : vertical angle of the element with the idealized plane
L : pre-length of the stabilization elements
x, y, z : the unit normal vector values of the idealized plane

With these formulas, the coordinate difference values between the top and end points for rock bolts to be added to the planes 1 and 2 have been calculated. The first pre-dimensioned (30 m) rock bolt placed according to these values is shown in Figure 5.12.

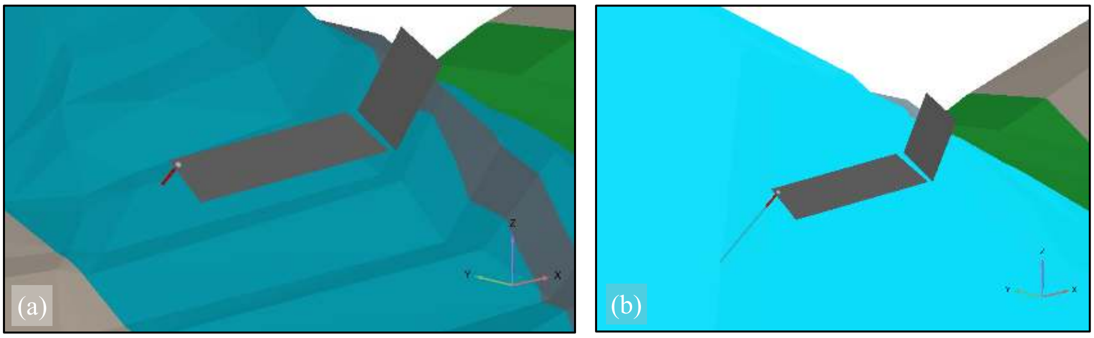

Figure 5.12 The 30 m long rock bolt with a top point on the idealized plane (a) and the position of the endpoint in the transparent ground view (b)

Direction vectors belonging to the plane were used in order to array the 30m length rock bolt horizontally and vertically on the plane. Values required for horizontal arraying of the rock bolt were calculated by multiplying the horizontal unit direction vector ($\vec{H}$) by the horizontal spacing between the bolts, and for the vertical arraying process, the values were multiplied by the vertical direction vector ($\vec{V}$) and the vertical spacing. In Figure 5.13, $\vec{N}$ (unit normal vector), $\vec{H}$, and $\vec{V}$ vectors are shown.

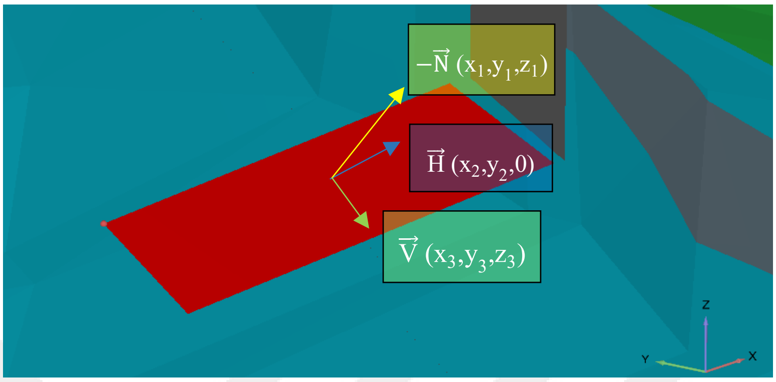

Figure 5.13 Unit normal, horizontal unit direction and vertical unit direction vectors

The horizontal unit direction vector and the vertical unit direction vector were calculated using the normal vector ($\vec{N}$) parameters of the plane. As the rock bolts are horizontally arrayed, the z component of the horizontal unit direction vector is 0 because it will only be shifted in the x-y plane. In the calculations with vector product, the parameters of the horizontal and the vertical unit direction vector were calculated in terms of unit normal vector parameters:

$$\vec{N} = \vec{H} \times \vec{V} = \begin{vmatrix} i & j & k \\ x_2 & y_2 & 0 \\ x_3 & y_3 & z_3 \end{vmatrix} \tag{5.4}$$

$$\vec{H} = \vec{V} \times \vec{N} = \begin{vmatrix} i & j & k \\ x_3 & y_3 & z_3 \\ x_1 & y_1 & z_1 \end{vmatrix} \tag{5.5}$$

$$\vec{V} = \vec{N} \times \vec{H} = \begin{vmatrix} i & j & k \\ x_1 & y_1 & z_1 \\ x_2 & y_2 & 0 \end{vmatrix} \tag{5.6}$$

As a result of the calculations made over these operations, horizontal and vertical unit direction vectors were obtained in terms of unit normal vector parameters as follows:

$$\vec{H}(x_2,y_2,z_2)=\vec{H}\left(\frac{y_1}{\sqrt{x_1^2+y_1^2}},\frac{-x_1}{\sqrt{x_1^2+y_1^2}},0\right) \tag{5.7}$$

$$\vec{V}(x_3,y_3,z_3)=\vec{V}\left(\frac{z_1\,x_1}{\sqrt{x_1^2+y_1^2}},\frac{-y_1}{z_1}\left(\sqrt{x_1^2+y_1^2}-\frac{1}{\sqrt{x_1^2+y_1^2}}\right),-\sqrt{x_1^2+y_1^2}\right) \tag{5.8}$$

When the normal vector values (x_1, y_1, z_1) of both idealized planes were replaced in these formulas, horizontal unit direction vectors and vertical unit direction vectors were calculated. The horizontal and vertical spacing lengths of the rock bolts in the arraying process were also calculated by multiplying the parameters of the horizontal and the vertical unit direction vectors by 3m in horizontal and vertical directions, which is the desired range (Figure 5.14).

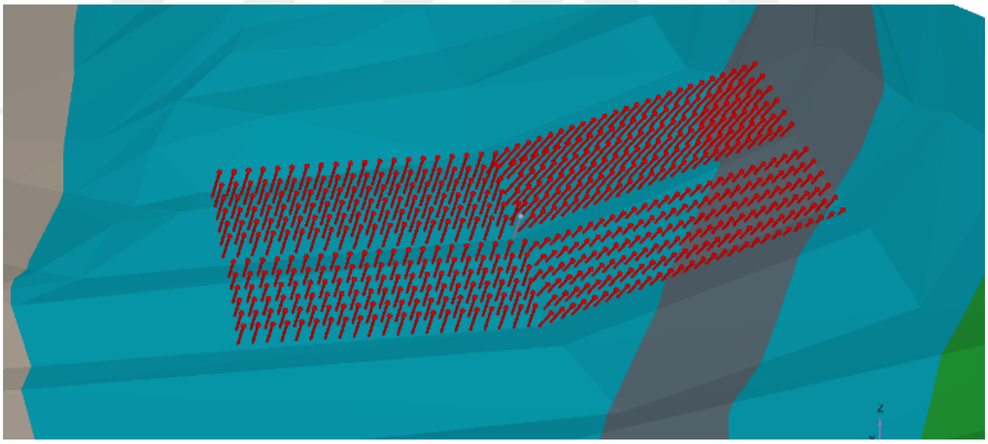

Figure 5.14 Arrayed rock bolts

5.2.2.3 Final Operations

The desired application length of the rock bolts placed on the finite element model is actually 16m. However, the bolts were modeled as 30 meters. In order to shorten the rock bolts as real lengths, the surface model was imported back to the software and the exceeding lengths of rock bolts between the terrain surface and idealized planes were deleted (Figure 5.15).

The intersecting process for exceeding rock bolts length in the ground was made separately in the idealized plane regions 1 and 2. For this purpose, by selecting length as 16 m in the formula (5.1), the results were used to shift the terrain model toward the ground. In this way, the regions between the real terrain surface and 16m shifted surface model, and the actual surface was intersected, and exceeding 16m part was removed (Figure 5.16). As a result, all the processes have been completed to pass to the analysis stage by defining structural parameters (geometrical and mechanical properties) to the bolts.

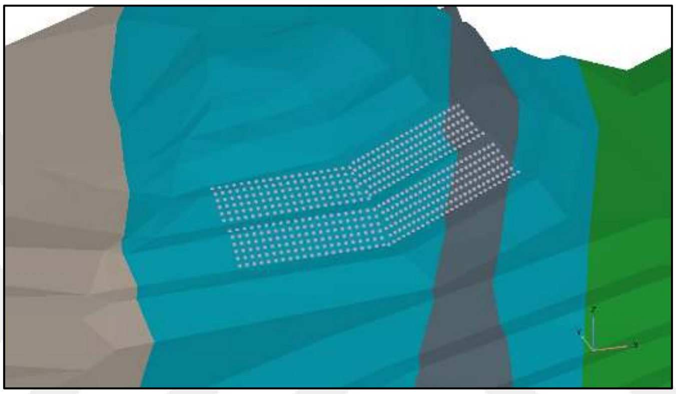

Figure 5.15 Rock bolts with exceeding portions removed above the surface

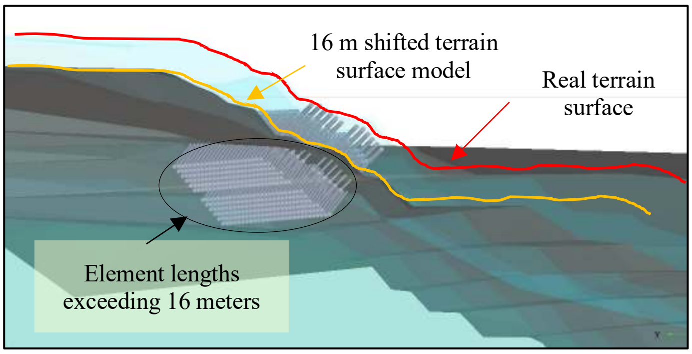

Figure 5.16 Shifting terrain surface model

5.2.2.4 Other Applications

The method of modeling structural elements is explained only for the application of rock bolts in the finite element software. The same method was applied as cable bolt on the 490 m and 460 m elevated benches. These applications were carried out with idealized planes which are formed according to the surface normal. It was applied on both benches with a width of 125 m and a horizontal spacing of 6m with a single row (Figure 5.17). Angles of the anchors with the horizontal change between 20° and 25° and 100m length.

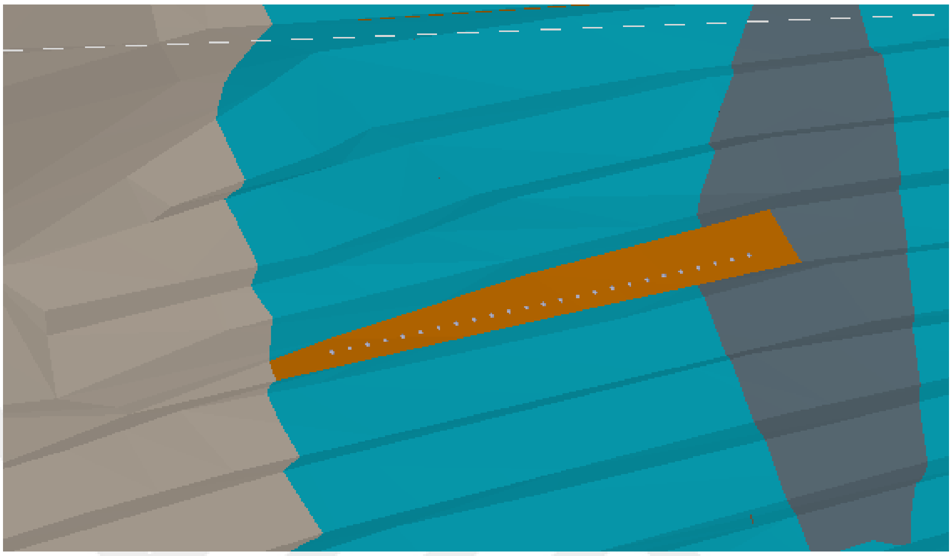

Figure 5.17 The cable bolt application at 460 m elevation

In addition to these applications, vertical anti-slide pile modeling at 490m elevation with 125m width and 50m length was generated (Figure 5.18). The lateral distance between the piles is 3m. In the analyses described in detail in the next section, these types of applications were compared by applying different combinations.

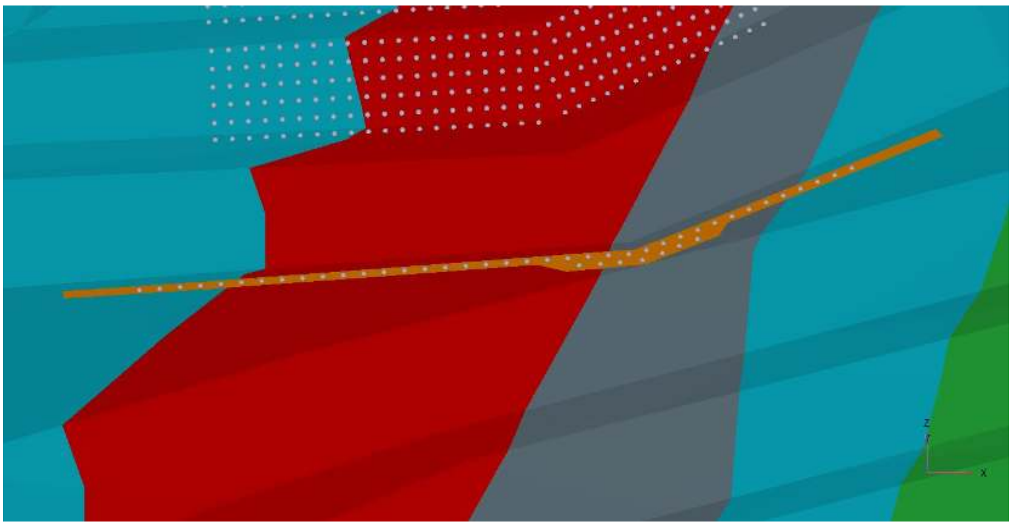

Figure 5.18 The anti-slide pile application at 490 m elevation

CHAPTER SIX
SLOPE STABILITY ANALYSES

6.1 Modelling Consideration

A finite element model is divided into a finite number of three-dimensional elements by the software in order to perform calculations such as surface displacements, internal forces of elements, and shear safety factor. These elements are called as meshes. Depending on the density of the mesh elements, the solution sensitivity, and duration vary. In the software, the detailed status of the mesh of each structural element and the soil can be adjusted in the coarseness factor section. With the roughness factor 0 to 1 assigned to the structural elements, solutions can be realized at the desired level of detail. Low roughness factor values mean that smaller size; however, a large number of mesh elements is used for the solution.

The software also needs to define a general roughness factor that it applies to the finite element model just before the model is divided into mesh elements. These are:

- Very fine,
- Fine,
- Medium,
- Coarse,
- Very coarse.

In addition to these adjustments, the mesh quality of the finite element model can be improved by the “advanced network element optimization” tool. All the adjustments made to separate the model into mesh elements are intended to determine the level of detail of the model. By increasing the level of detail, the quality of the model develops. However, increasing the level of detail and the number of mesh elements extends the time to calculate.

During all the studies on the software, the most challenging operation was that dividing the finite element model to meshes. In most of the attempts at the separation of mesh elements with local roughness factor values defined to soil units and structural elements, the processes could not be finished. In these errors, the software warns, “Try again by defining different local roughness factor”. After many unsuccessful attempts, it was tried to reach the result by using the values entered manually instead of automatic values of general roughness values. With this approach, the local roughness factor values in Table 6.1, and the general roughness factor are used, mesh generation was successfully completed. When the quality of the mesh element was examined on the software, it was seen that low-quality mesh elements are concentrated in the non-slip regions. In the landslide region, it can be said that the quality of the mesh element is better than the average compared to the regions (Figure 6.1). Thus, a mesh of sufficient quality for the analysis was created.

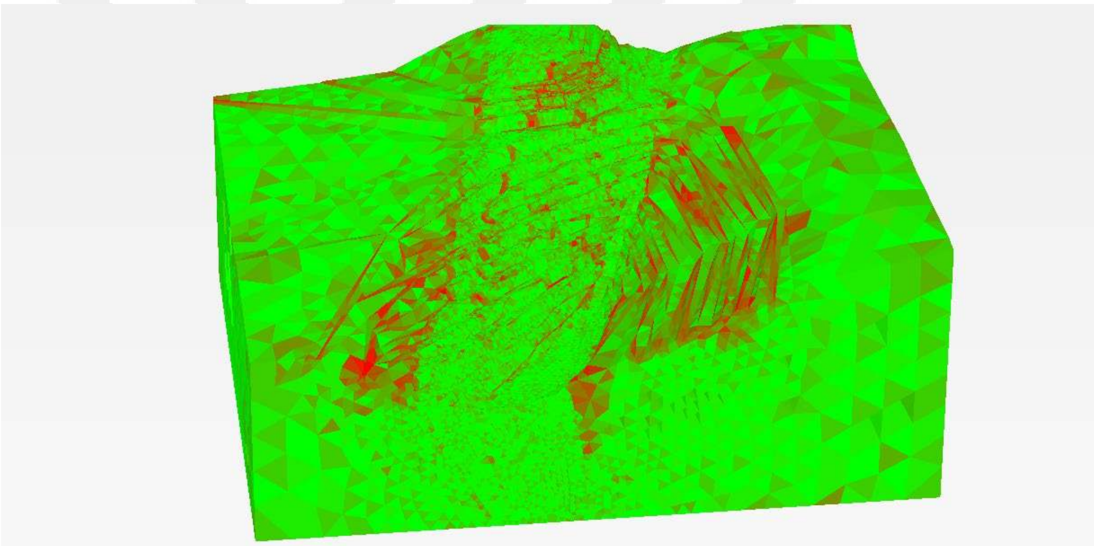

Figure 6.1 The quality status of mesh elements

Table 6.1 The roughness factors

Geological Units	Roughness Factor
Sliding Zone	0.15
Mica-schist	0.15
Quartzo-Feldspar	0.15
Feldspar	0.15
Gneiss	1.00
General Roughness Factor	0.04125

After the surface model analyses discussed in Chapter 4, it was decided to construct a three-dimensional finite element model with the SEM4 option. In the created model, the effect of the stability measures introduced in stages was investigated by idealizing the shear mechanism showed on the surface geology map given in Figure 6.2. These measure steps and their effects on slope stability are discussed below.

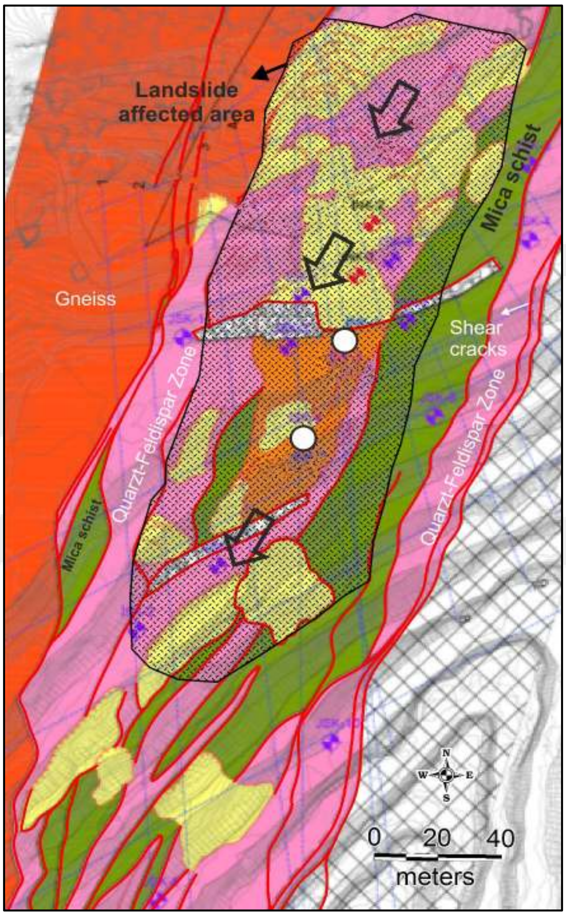

Figure 6.2 The landslide field with ellipsoid shape, shear direction and surface geology on the surface

6.2 Slope Stability Measures and Analyses

A number of commonly used methods for slope stability was investigated by 3D finite element analysis. In this context, 3 different solutions have been proposed and these slope stability measures are listed below.

- Plan A: Rock bolts manufactured between +500 and +520 elevations. Their main function is to fix the highly separated rock blocks. Therefore, Plan A will be implemented in the field (regardless of the analysis results). Plan B and Plan C will be added to the rock bolt application and the appropriate one will be selected.

- Plan B: Prestressed anchor application on the slope face between + 490 and +500 elevations which is activated in the model following the construction of rock bolts. The calculation is made under horizontal peak acceleration of 0.03g which can trigger slope movement. The anchors were applied to the model with a diameter of 8 cm in unbonded free part (85 m) and 20 cm in bonded part (15 m), a length of 100 m and with angle of 20°.

- Plan C: Analysis of anti-slide piles on +500 elevation with rock bolts. The piles will be built on the bench at +490 level and connected with the head beam. The piles were applied to the model with a diameter of 140 cm and a height of 50 m. The calculation is also made under horizontal peak acceleration of 0.03g which can trigger slope movement.

In the PLAXIS 3D finite element analysis software, analyses are performed in staged construction. In this way, the traces of stress-strain resulting from field conditions and excavation-filling processes can be simulated. Gradually, the analysis can be carried out as the steady state, then the formation of the sliding and then the application of structural solutions. As a result, the internal forces on the structural elements and the safety factor in the field can be obtained.

Figure 6.3 shows the three-dimensional finite element model geometry of the landslide area. Mohr-Coulomb Failure Model parameters used in the analysis for rock units are given in Table 5.1. Since there is no free groundwater table in the field and drainage conditions cannot be determined within the complex three-dimensional geometry, excessive pore water pressure or hydrostatic water pressure due to shear deformation is not defined in the analysis stages. Instead, the weakening and shear effect of water in the very weak mica-schist zone was handled with the help of the parameter assigned to the interface elements, the finite element model (the case where rock bolts on the +500 elevation) was calibrated through back analysis to obtain displacements in the inclinometer readings as much as possible. In this context, the interface element factor was reduced, and the calculations were repeated until the factor of safety against sliding dropped down to a meaningful low value (FS=1.2).

As a result, when the quartz-feldspar and mica-schist units were assigned R_{inter}=0.0625 and R_{inter}=0.3312 respectively, the phi-c reduction technique was used to achieve 1.20 under static conditions, and the subsequent calculation steps were continued under these parameters.

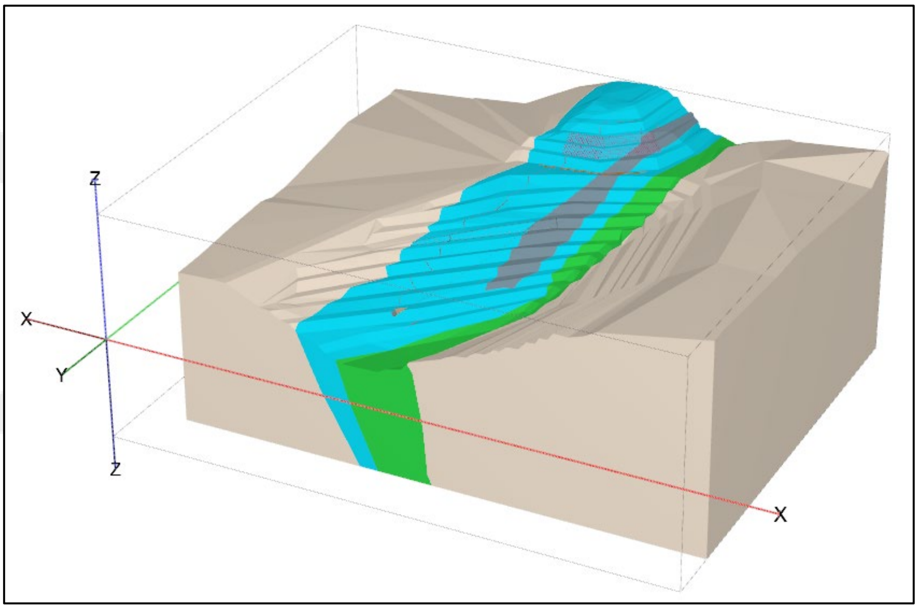

Figure 6.3 Finite element model geometry for analysis

PLAN A

According to this plan, rock bolt application was modeled on 2 slope benches (+490-+500 and +500-+510) with spacing of 2.5 m horizontally and vertically at 300 m^2 area. These modeling phases are explained in detail in Chapter Five. The main purpose of the rock bolt application at the elevation of +490 is to fix the weathered rock structure in the region. Furthermore, the shear and normal force strengths of the bolts provide a resistance to shear and ensure that the shear circle is shifted down from this region. Rock bolts have a diameter of 32 mm and a wall thickness of 17 mm. In application, the 15 mm hole inside is filled by injection of concrete grout.

The critical surface as appears on Figure 6.4 and Figure 6.5 was obtained in phi-c reduction analysis stage. Formation of this surface was governed by the geometry, soil-rock stratification and assigned interfaces surrounding the sliding body. The sliding mass is approximately 20 m thick within the central portion of Section A-A. At higher and lower elevations, the thickness reduces to 10~12 m band. The location of the cut section is illustrated on Figure 6.5. The interface elements, on the other hand, are shown in Figure 6.6. As noted earlier in this report shear strength of these elements is directly related to neighboring geo materials by means of interface adjustment factor "R".

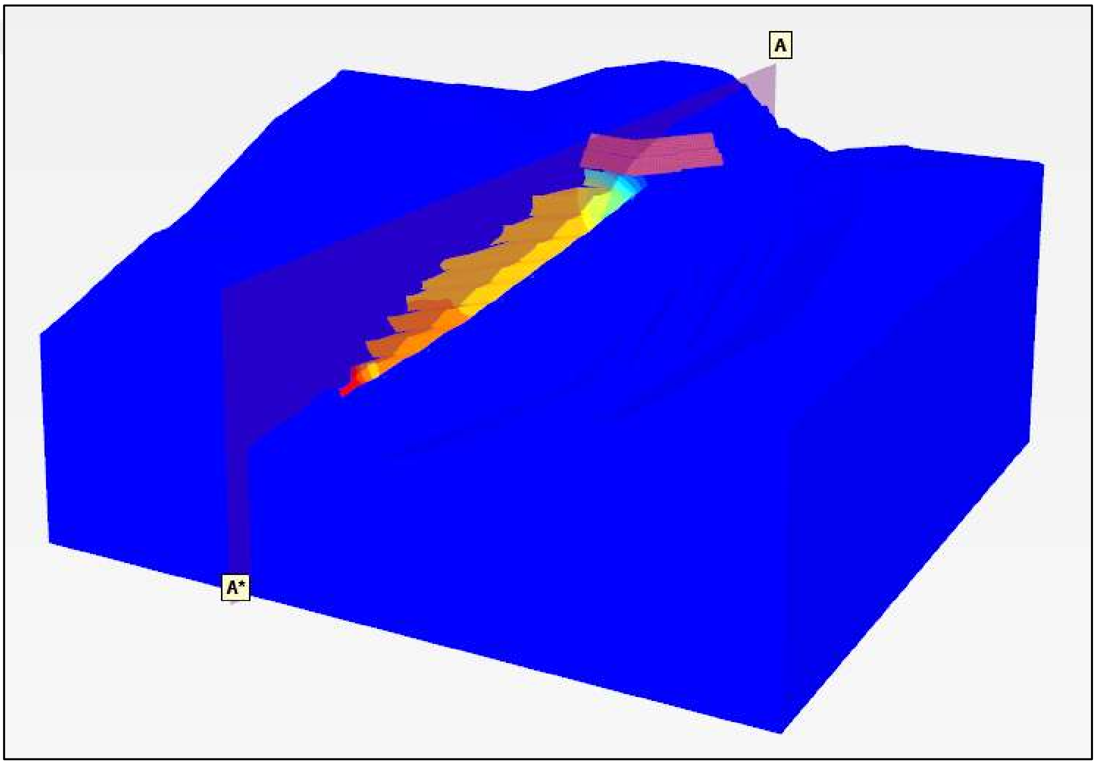

Figure 6.4 Phi-c reduction analysis performed with rock bolts above +500 elevation and Section A-A

It is obtained that the factor of safety value did not change, however, Figure 6.4 shows that the slip surface moved to lower elevations. The reason FS does not change is the fact that the excessive sliding in the lower elevations could not be reduced and only the sliding problem in the upper elevations was solved. Besides, the sliding will be tried to be reduced by the Plan B and Plan C.

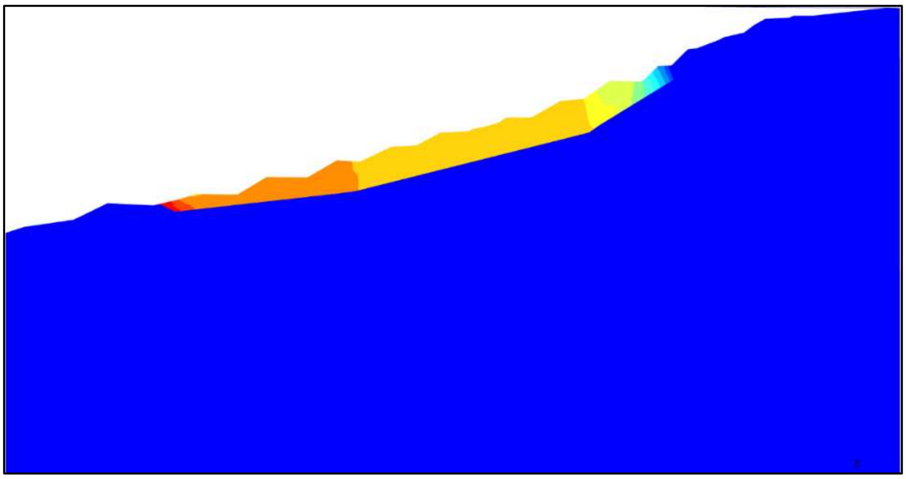

Figure 6.5 Critical sliding surface in Section A-A' (Fs=1.20)

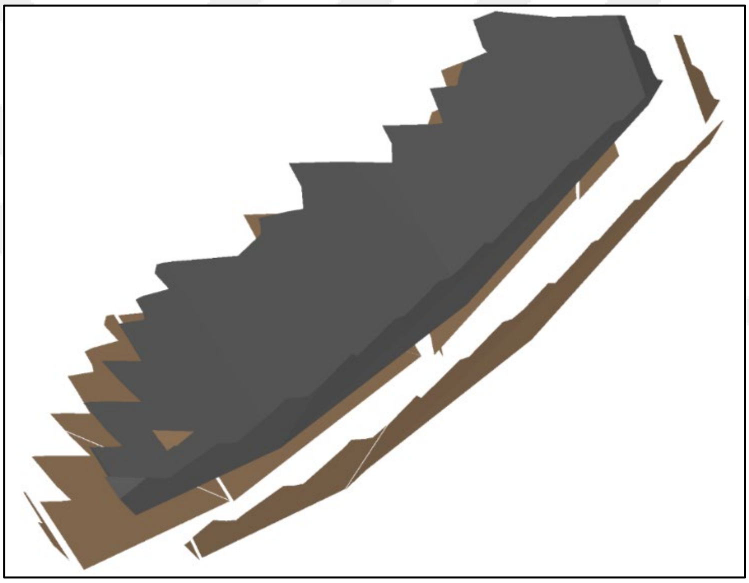

Figure 6.6 Interface elements defined around the sliding mass

PLAN B

In addition to the rock bolts on the +500 elevation, prestressed anchor measure is intended for the protection of the road at elevation +490. It is aimed to increase the friction force between the rock joints by the effect of the anchors. For this purpose, 16 prestressed anchors were modeled. The prestress value for each member was assigned as 800 kN. In the deep failure analysis for this option, the safety factor FS = 1.20 was found. In terms of shear safety, prestressed anchors do not have a significant benefit, but the reinforced concrete wall (which acts as a chest beam) supports the anchor and shifts the critical sliding surface slightly below the +500 level (Figure 6.7).

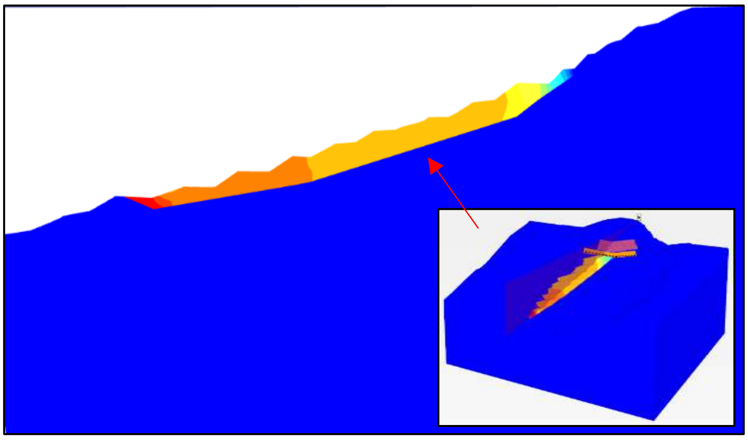

Figure 6.7 Critical sliding surface for the option of prestressed anchoring measures in addition to rock bolts (F_S=1.20)

PLAN C

Slope stabilizing pile option was also studied in this study. A pile row with 43 piles was added to the finite element model at +490 elevation. As an initial approach pile diameter and length were set as 140cm and 50m, respectively. The center-to-center plan spacing of the piles were decided as 3m. FEM runs revealed that longer piles were only necessary within the highly weathered and sheared mica-schist bands. Deformation pattern of the pile row as shown in Figure 6.8 points out to the fact that piles in the east mica-schist band exhibit lateral deformation to a significant depth deserving a much longer length as compared with the remaining ones.

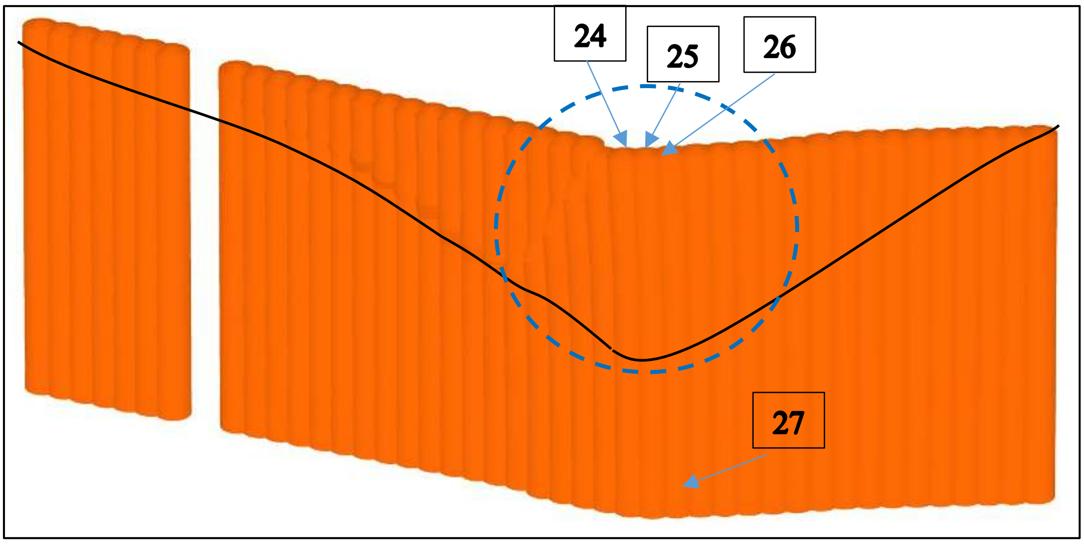

Figure 6.8 Deformation pattern of the single row slope stabilizing piles

One should note the gap between the first group of seven piles and the second group was left intentionally in order to overcome meshing difficulties nearby in west mica-schist band, which is considerably narrower than that in east.

The parameters of the structural members using for Plan A, Plan B and Plan C are summarized in Table 6.2.

Table 6.2 Material properties of the structural elements

Properties	**Pile**	**Rock Bolt**	**Ground Anchor**	
			Bonded Part	**Unbonded Part**
Material Type	Elastic	Elastic	Elastic	Elastic
Diameter (m)	1.40	0.032	0.20	0.08
Total Length (m)	50	16	15	85
E (kN/m^2)	50.0 E+6	45.0 E+6	27.5 E+6	200.0 E+6
γ (kN/m^3)	25	24	25	-
Predefined Beam Type	Massive Circular Beam	Massive Circular Beam	Massive Circular Beam	-
Max. Pullout Force (kN)	1.0 E+12	240	1200	-
Max. Base Resistance (kN)	1.5 E+04	0	0	-

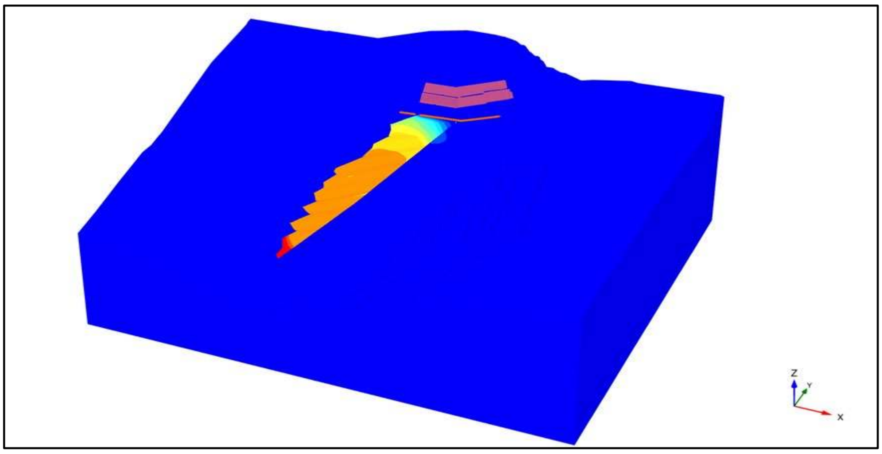

Figure 6.9 Analysis for the case of anti-slide piles with rock bolts on +500 elevation ($F_S \cong 1.614$)

In the calculations, FS = 1.614 against deep failure is calculated. As shown in Figure 6.9, the safety factor is increased by the addition of the anti-slide piles, and the critical sliding surface is shifted below the +490 level.

Although FEM analyses were made for a pile length of L=50m, achieved results proved that the moment and shear force distributions along the pile depth within the circled zone pointed out that longer piles are needed inside the highly weathered mica-schist bands (Figures 6.10 and Figure 6.11). Bending moment and shear force distributions indicate that L=50m long piles are not fully fixed at the tip as one can notice on Figure 6.10 and 6.11. This behavior is better observed when piles #23 and #24 are excluded from the set (Figure 6.12 and 6.13) since they unusually exhibited larger values nearby the pile cap, which can be attributed to meshing difficulties in 3D model. Average of the shear forces and bending moments are also plotted on the same figures.

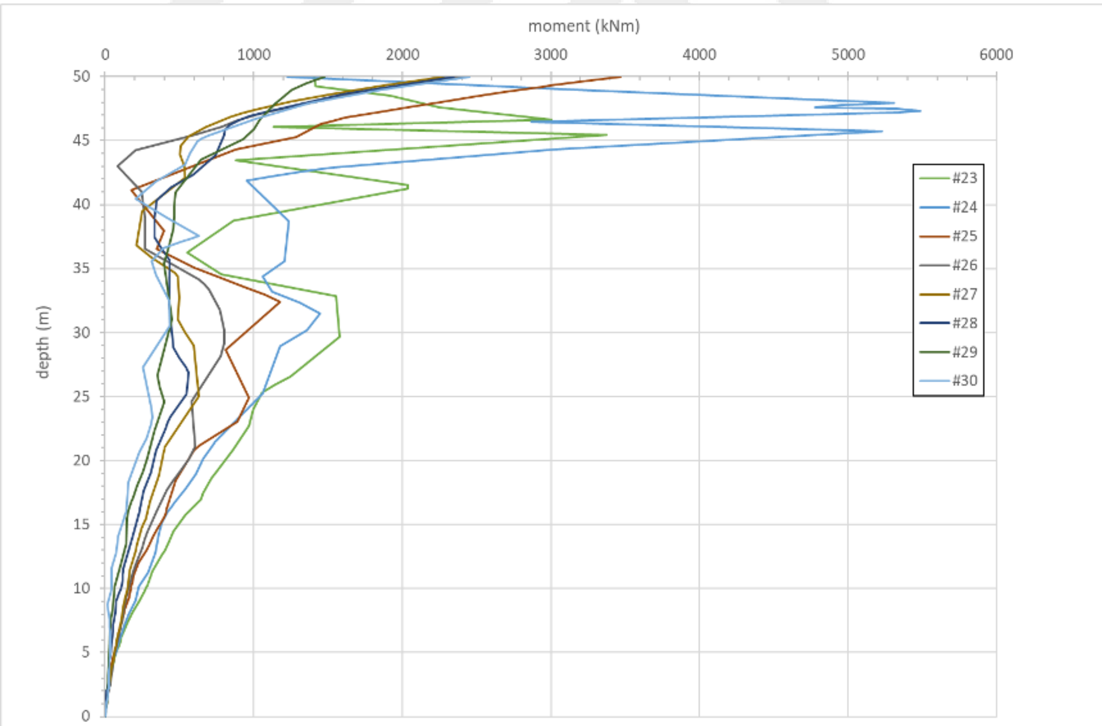

Figure 6.10 Resultant bending moment distributions along piles #23 ~ #30

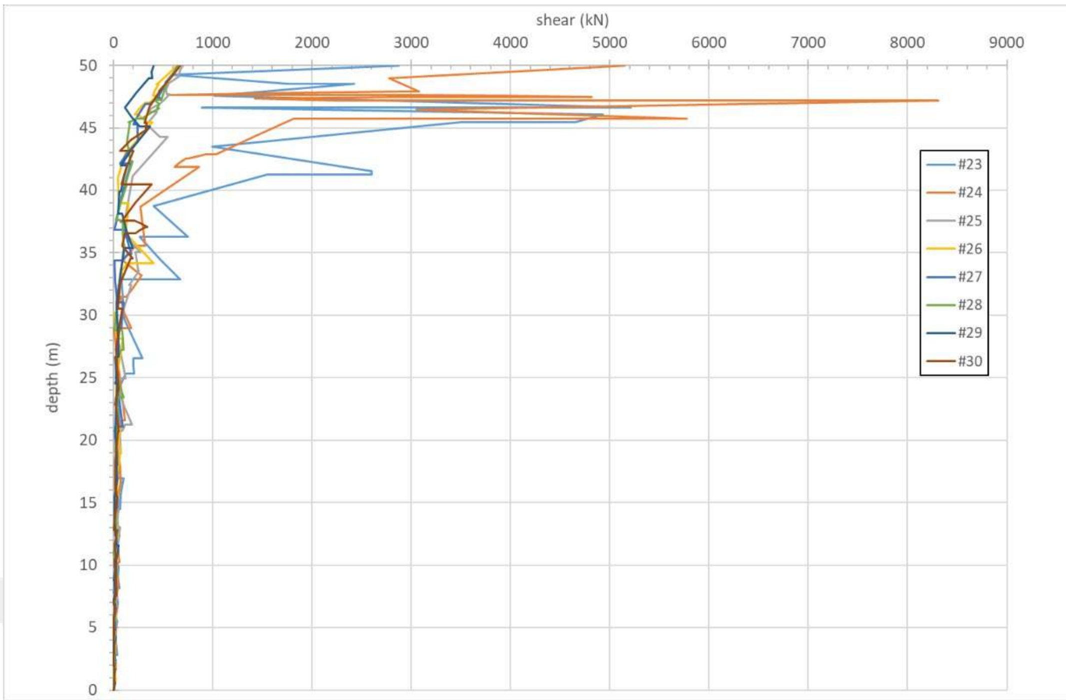

Figure 6.11 Resultant shear force distributions along piles #23 ~ #30

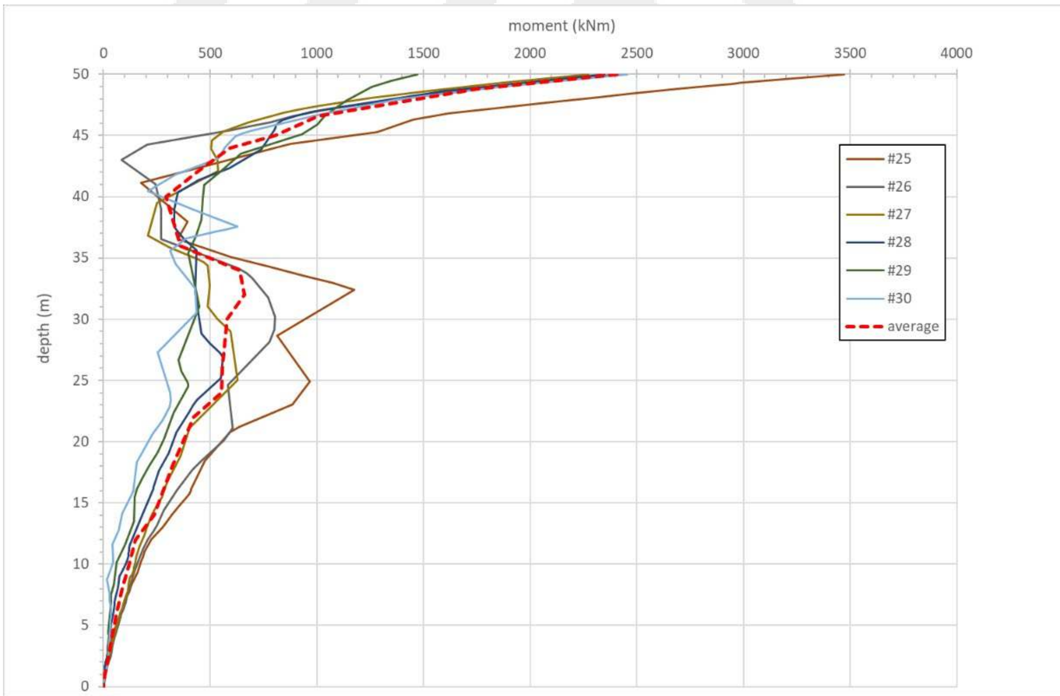

Figure 6.12 Resultant bending moment distributions along piles #25 ~ #30 and their average line

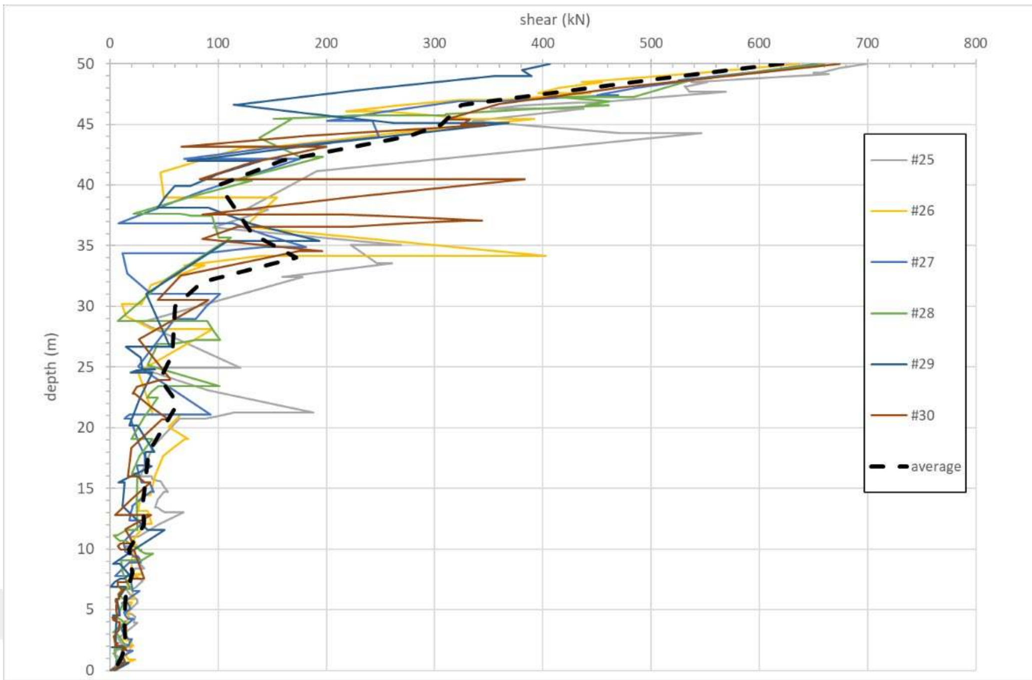

Figure 6.13 Resultant shear force distributions along Piles #25 ~ #30 and their average line

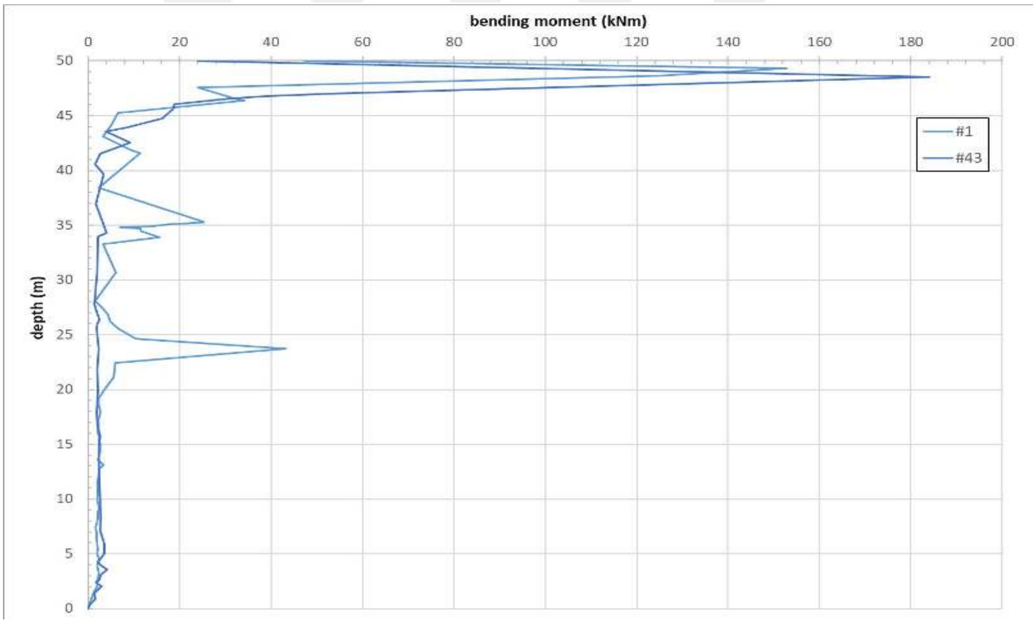

Figure 6.14 Bending moment distributions along the two edge piles

Internal forces are significantly lower than the central piles (i.e. 23~30) at two edge piles (Pile #1 and #43) as shown in Figure 6.14. It appears that the design moment is 2500 kNm for the central portion at the cap level whereas it reduces to approximately 160 kNm at the edges. Figure 6.15-6.18 shows the shear force and moment graphs on the piles together.

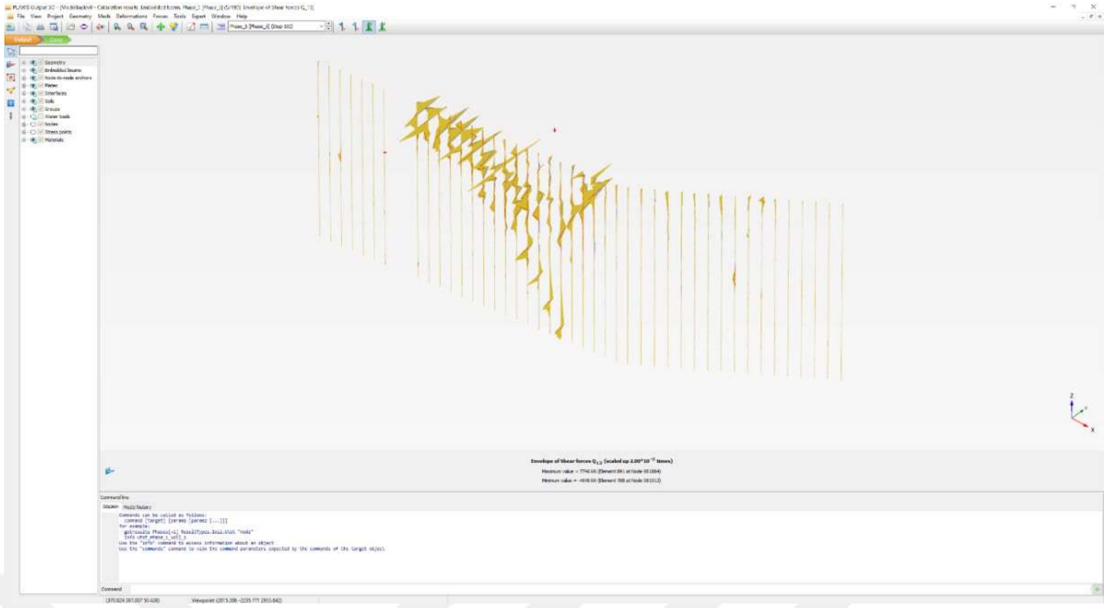

Figure 6.15 y-y axis shear force diagrams in piles at +490 elevation as a result of 0.03g ground acceleration analysis in x and y directions in finite element model

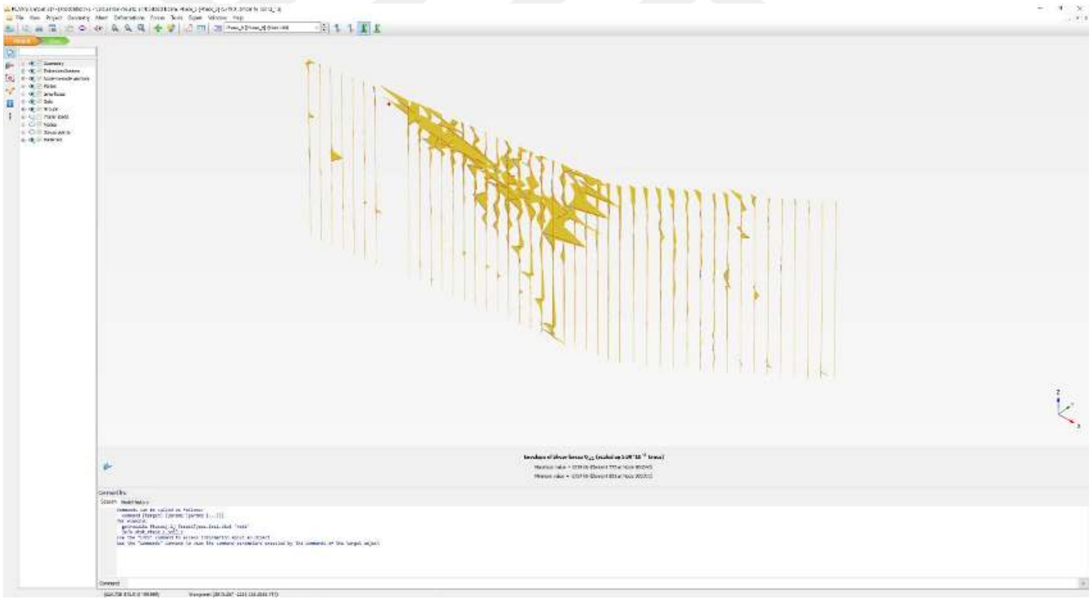

Figure 6.16 x-x axis shear force diagrams in piles at +490 elevation as a result of 0.03g ground acceleration analysis in x and y directions in finite element model

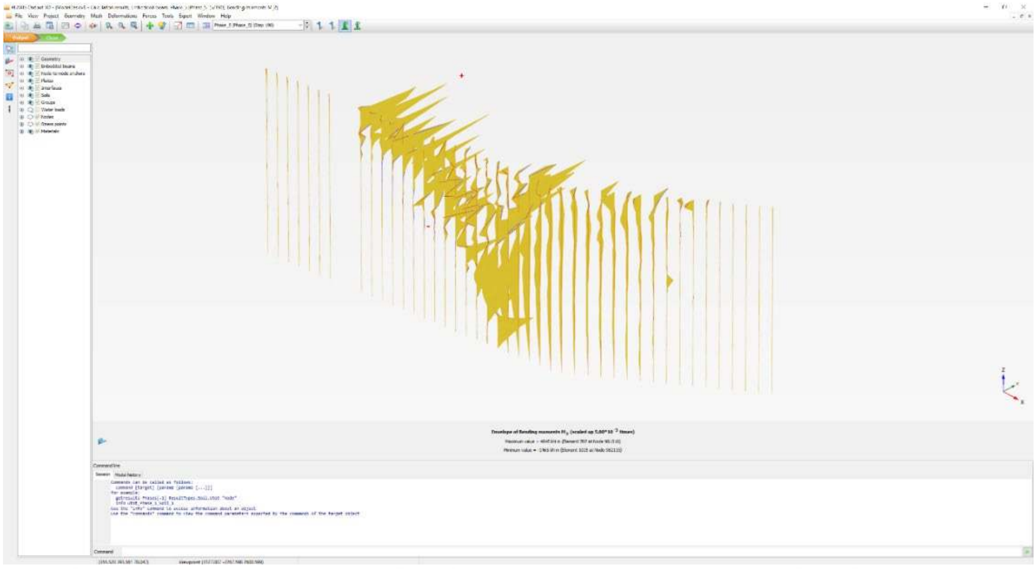

Figure 6.17 y-y axis moment diagrams in piles at +490 elevation as a result of 0.03g ground acceleration analysis in x and y directions in finite element model

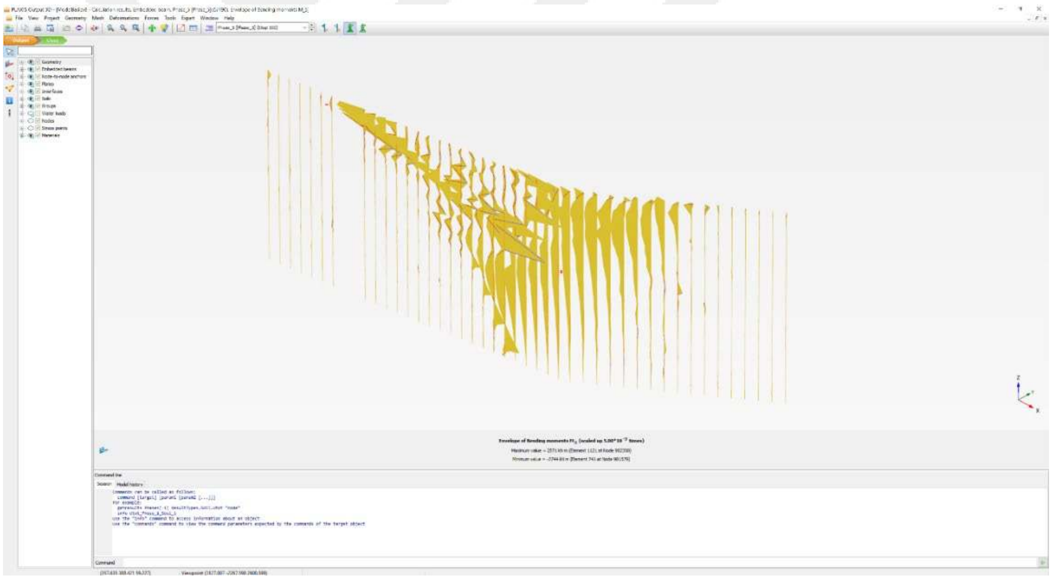

Figure 6.18 x-x axis moment diagrams in piles at +490 elevation as a result of 0.03g ground acceleration analysis in x and y directions in finite element model

As seen in Figure 6.15-6.18, the three-dimensional analysis model was able to represent the slope’s behavior realistically, and the three-dimensional behavior of the anti-slide piles could be obtained. This behavior was influenced by the arching effect of the landslide mass to the sides, and the rock units, which were stable on both sides of the sliding slope, were able to support the piles in the sliding part, and thus, the non-stable mass.

CHAPTER SEVEN
DISCUSSIONS AND CONCLUSION

This thesis focuses on the development of a methodology for the use of unmanned aerial vehicles in slope stability problems. In this context, three-dimensional topographic models of the active landslide in a mine site located in Aydın/Çine were created, analyzes were performed on these models and time-dependent monitoring of the displacements in the site was performed. For this purpose, aerial images were obtained by making flights, and surface models were created by using digital image processing techniques on photographs. Changes in topographic models were monitored with flights on different dates, and data were collected for finite element analysis. The original aspect of the thesis was the transfer of the surface topography obtained from the photographic methods and the data obtained from the field to the finite element model. For this purpose, a systematic study was carried out, and studies were carried out in order to perform finite element analyses, which resulted in logical periods. The results of this thesis are summarized below:

- It was determined that surface displacements exceeding a threshold value could be detected as a result of the comparison of slope models obtained with aerial photographs. In addition, it was observed that the technique can be used in applications such as monitoring of settlements due to water withdrawal in large areas, determination and monitoring of surface displacements and discontinuities due to fault dislocations.

- It was revealed that the deformations of slopes, as well as changes in vegetation cover and field interventions, can be detected by comparing the aerial images taken at different dates. Thus, the side benefits of aerial imaging and modeling techniques outside the scope of the thesis were also observed.

- In the studies conducted for the mine site, it was found that the aerial imaging technique provided a great advantage, especially in steep areas such as mine sites and where topographic reception is impossible with the traditional methods. Another advantage of the technique is that the surface topography is created very quickly and with high resolution compared to the conventional method. Thanks to the rapid creation, it possible to compare the surfaces obtained at short intervals with each other. In addition, the surface model, which has a high level of visual data obtained, has been an advantage for the determination of geological units in the field. It has greatly facilitated the monitoring of geological units and discontinuities in steep and large areas where it is difficult to move in the field.

- The boundaries of the mass moving in the slope were determined by comparing the surface models formed at certain time intervals from the aerial photographs, and this data was used to solve the landslide mechanism and to construct the finite element model. In addition to this data, inclinometer wells equipped in the field were used in the generation of the finite element model.

- The forest cover in the peak area of the +543 elevated hill in the mine site has produced unfavorable results on the structure of the dense point cloud model and hence, the surface model. Due to the complex structure of the trees and the inability to maintain their location due to the wind, gaps were formed in these regions of the dense point cloud model. Therefore, in the surface model used for finite element analysis, point-to-point jumps and consequently lead to the formation of defective surfaces.

- Although the defective surface formations in the surface model can be removed with the photogrammetric software tool, there is no solution for such complex terrain. For this reason, it is necessary to perform manual intervention on the surface model. The main objective of the interventions was to improve and simplify the overall structure of the surface as much as possible without deterioration. Accordingly, it was found that surface models with less polygonal numbers provide faster and more accurate model formation. The dense and complex structure of the other models has led to very long process times, and even the finite element rigid model has not been created.

- Geological units on the finite element model are formed by intersecting the 3D finite element model with the boundary surfaces of the units. For this reason, it is provided to create boundary surfaces of geological units by placing each borehole data in its own position in AutoCAD software, which provides 3D drawing opportunity. As mentioned before, because of the contribution of simple surface models to finite element analysis, it is aimed to keep the polygon number low as much as possible in this process. In addition, it is known that the creation of surface models of geological units can be generated automatically by some geotechnical programs (e.g., Geo5-Stratigraphy). This automatic method can also be integrated into the methodology followed in this study.

- One of the most challenging issues in the studies was the mesh formation process, which is necessary for the finite element analyses. In the complex structure models, great difficulty was encountered in the meshing processes. By using simple and low polygonal surface models, this process has been more successful. The quality of the mesh elements to be used in finite element analysis directly affects the accuracy of the analysis calculations. Therefore, after the mesh creation process, this situation should be followed with the mesh quality tool on the finite element program.

- In the calculations made for various slope stability measures, it was observed that the safety factor against sliding did not increase significantly, but that the activated mass could be shifted downwards from the peak of the hill at +543 elevation. The three-dimensional geometry of the slope and in particular, the effect on the anti-slide piles could be clearly observed. The developed technique was seen to be applicable in the analysis and solution of real engineering problems.

- In the analysis made by 3D modeling, internal moment and shear force diagrams on structural elements can be obtained in detail. In classical 2D analyzes, diagrams for the most pessimistic section can be obtained. In this way, it is very difficult to decide the application spacing of the structural member with the data obtained by considering a single section. Furthermore, the variation of the internal force distribution on the structural element along the width cannot be achieved by 2D analysis. However, as this study shows, the fact that the internal force distribution is known along the width in 3D slope stability analyzes makes a difference in the selection of structural elements properties (length, diameter, material). By this means, different element types can be selected along the width and secure-economic solutions can be chosen.

- Another advantage of the formed surface models is that electronic data can be stored and shared with remote users. Storing data has an opportunity on a resolution of disputes and sharing data has made it possible to collaborate with remote clients.

- The creation of models using image processing with images taken from unmanned aerial vehicles and using them in finite element analysis required a high amount of processing power. Besides, during the systematic study, data transfer between image processing software and finite element software has been a labor-intensive part.

REFERENCES

Alkasawneh, W., Husein Malkawi, A. I., Nusairat, J. H., & Albataineh, N. (2008). A comparative study of various commercially available programs in slope stability analysis. *Computers and Geotechnics*, *35*(3), 428–435.

Ashkenazi, V., & Yau, J. (1986). Significance of discrepancies in the processing of GPS data with different algorithms. *Bulletin Géodésique*, *60*(3), 229–239.

Bentley Geotechnical Engineering. (2016). Plaxis 3D 2016: importing CAD data into PLAXIS 3D [Video File]. Retrieved January 10, 2020, from https://www.youtube.com/watch?v=PcXSZyBVhF8.

Besl, P. J., & McKay, N. D. (1992). A Method for Registration of 3-D Shapes. *IEEE Transactions on Pattern Analysis and Machine Intelligence*, *14*(2), 239–256.

Carbonneau, P. E., & Dietrich, J. T. (2017). Cost-effective non-metric photogrammetry from consumer-grade sUAS: implications for direct georeferencing of structure from motion photogrammetry. *Earth Surface Processes and Landforms*, *42*(3), 473–486.

Chandler, J., Ashmore, P., Paola, C., Gooch, M., & Varkaris, F. (2002). Monitoring river-channel change using terrestrial oblique digital imagery and automated digital photogrammetry. *Annals of the Association of American Geographers*, *92*(4), 631–644.

Cheng, Y. M., Lansivaara, T., & Wei, W. B. (2007). Two-dimensional slope stability analysis by limit equilibrium and strength reduction methods. *Computers and Geotechnics*, *34*(3), 137–150.

CloudCompare. (n.d.). *CloudCompare version 2.6.1 user manual*. Retrieved January 10, 2020, from http://www.cloudcompare.org/doc/qCC.

Cruden, D. M. (1991). A simple definition of a landslide. *Bulletin of the International Association of Engineering Geology*, *43*, 27–29.

Cuneyt Erenoglu, R. (2016). Generating a digital elevation model using unmanned aerial system for a deep seated rotational landslide on forest cover and vegetation. *Austrian Journal of Forest Science, 133*, 47–61.

Dehghan, A. N., Shafiee, S. M., & Rezaei, F. (2012). 3-D stability analysis and design of the primary support of Karaj metro Tunnel: Based on convergence data and back analysis algorithm. *Engineering Geology*, *141*, 141–149.

Dunnicliff, J. (1993). *Geotechnical instrumentation for monitoring field performance.* (1st ed.). New York: John Wiley & Sons.

Erenoğlu, R. C. (2016). Generating a digital elevation model using unmanned aerial system. *Austrian Journal Forest Science, 133,* 47-61.

Furukawa, Y., & Ponce, J. (2010). Accurate, dense, and robust multiview stereopsis. *IEEE Transactions on Pattern Analysis and Machine Intelligence*, *32*(8), 1362–1376.

Gili, J. A., Corominas, J., & Rius, J. (2000). Using global positioning system techniques in landslide monitoring. *Engineering Geology*, *55*(3), 167–192.

Griffiths, D. V., & Lane, P. A. (1999). Slope stability analysis by finite elements. *Géotechnique*, *49*(3), 387-403.

Griffiths, D. V., & Marquez, R. M. (2007). Three-dimensional slope stability analysis by elasto-plastic finite elements. *Géotechnique*, *57*(6), 537–546.

Gupta, S. K., & Shukla, D. P. (2017). 3D reconstruction of a landslide by application of uav & structure from motion. *20th AGILE Conference on Geographic Information Science*, 9–12.

Guzzetti, F., Carrara, A., Cardinali, M., & Reichenbach, P. (1999). Landslide hazard evaluation: a review of current techniques and their application in a multi-scale study, Central Italy. *Geomorphology, 31*, 181-216.

Hackl, J., Adey, B. T., Woźniak, M., & Schümperlin, O. (2018). Use of unmanned aerial vehicle photogrammetry to obtain topographical information to improve bridge risk assessment. *Journal of Infrastructure Systems*, *24*(1), 04017041.

Hicks, M. A., & Spencer, W. A. (2010). Influence of heterogeneity on the reliability and failure of a long 3D slope. *Computers and Geotechnics*, *37*(7–8), 948–955.

Huang, M., & Jia, C. Q. (2009). Strength reduction FEM in stability analysis of soil slopes subjected to transient unsaturated seepage. *Computers and Geotechnics*, *36*(1–2), 93–101.

Hungr, O., Evans, S. G., Bovis, M. J., & Hutchinson, J. N. (2001). A review of the classification of landslides of the flow type. *Enviromental & Engineering Geoscience*, *7*(3), 221–238.

James, M. R., Robson, S., d'Oleire-Oltmanns, S., & Niethammer, U. (2017). Optimising UAV topographic surveys processed with structure-from-motion: ground control quality, quantity and bundle adjustment. *Geomorphology*, *280*, 51–66.

Janin, J. P., Dias, D., Emeriault, F., Kastner, R., Le Bissonnais, H., & Guilloux, A. (2015). Numerical back-analysis of the southern Toulon tunnel measurements: A comparison of 3D and 2D approaches. *Engineering Geology*, *195*, 42–52.

Javernick, L., Brasington, J., & Caruso, B. (2014). Modeling the topography of shallow braided rivers using Structure-from-Motion photogrammetry. *Geomorphology*, *213*, 166–182.

Kim, Y., & Jeong, S. (2011). Analysis of soil resistance on laterally loaded piles based on 3D soil-pile interaction. *Computers and Geotechnics*, *38*(2), 248–257.

Koschitzki, R., Schwalbe, E., Cardenas, C., & Maas, H. G. (2017). Photogrammetric monitoring concept for remote landslide endangered areas using multi-temporal aerial imagery. *IEEE 1st International Symposium on Geoscience and Remote Sensing, GRSS-CHILE 2017*, 1–6.

Leon, J. X., Roelfsema, C. M., Saunders, M. I., & Phinn, S. R. (2015). Measuring coral reef terrain roughness using "structure-from-motion" close-range photogrammetry. *Geomorphology*, *242*, 21–28.

Li, C., & Stillborg, B. (1999). Analytical models for rock bolts. *International Journal of Rock Mechanics and Mining Sciences*, *36*(8), 1013–1029.

Li, Y. J., Hicks, M. A., & Nuttall, J. D. (2015). Comparative analyses of slope reliability in 3D. *Engineering Geology*, *196*, 12–23.

Liu, S. Y., Shao, L. T., & Li, H. J. (2015). Slope stability analysis using the limit equilibrium method and two finite element methods. *Computers and Geotechnics*, *63*, 291–298.

Lowe, D. G. (2004). Distinctive ımage features from scale-invariant keypoints. *International Journal of Computer Vision*, *60*(2), 91–110.

Manousakis, J., Zekkos, D., Saroglou, F., & Clark, M. (2016). Comparison of uav-enabled photogrammetry-based 3d point clouds and interpolated dsms of sloping terrain for rockfall hazard analysis. *ISPRS - International Archives of the Photogrammetry, Remote Sensing and Spatial Information Sciences*, *42*, 71–77.

Micheletti, N., Chandler, J. H., & Lane, S. N. (2015). Structure from motion (SFM) photogrammetry. *Clarke, L.E. and Nield, J.M. (Eds.) Geomorphological Techniques (Online Edition)*, *2*, 1–12.

Niethammer, U., James, M. R., Rothmund, S., Travelletti, J., & Joswig, M. (2012). UAV-based remote sensing of the Super-Sauze landslide: evaluation and results. *Engineering Geology*, *128*, 2–11.

Pradhan, D. L. (2012). *Development of p-y curves for monopiles in clay using finite element model Plaxis 3D Foundation*. Master's Thesis, Norwegian University of Science and Technology, Trondheim.

Reinoso, J. F., Gonçalves, J. E., Pereira, C., & Bleninger, T. (2018). Cartography for civil engineering projects: Photogrammetry supported by unmanned aerial vehicles. *Iranian Journal of Science and Technology, Transactions of Civil Engineering*, *42*(1), 91–96.

Ruggles, S., Clark, J., Franke, K. W., Wolfe, D., Reimschiissel, B., Martin, R. A., Okeson, T., et al. (2016). Comparison of SfM computer vision point clouds of a landslide derived from multiple small UAV platforms and sensors to a TLS-based model. *Journal of Unmanned Vehicle Systems*, *4*(4), 246–265.

Ružić, I., Marović, I., Benac, Č., & Ilić, S. (2014). Coastal cliff geometry derived from structure-from-motion photogrammetry at Stara Baška, Krk Island, Croatia. *Geo-Marine Letters*, *34*(6), 555–565.

Saito, H., Uchiyama, S., Hayakawa, Y. S., & Obanawa, H. (2018). Landslides triggered by an earthquake and heavy rainfalls at Aso volcano, Japan, detected by UAS and SfM-MVS photogrammetry. *Progress in Earth and Planetary Science*, *5*(1), 15.

Savvaidis, P. D. (2003). Existing landslide monitoring systems and techniques. *From Stars to Earth and Culture. The Aristotle University of Thessaloniki, Greece*, 242–258.

Schweiger, H. F. (2005). Application of FEM to ULS design (Eurocodes) in surface and near surface geotechnical structures. *Proc. 11th Int. Conf. Computer Methods and Advances in Geomechanics, Patron Editore, Bologna*, *4*, 419–430.

Siebert, S., & Teizer, J. (2014). Mobile 3D mapping for surveying earthwork projects using an unmanned aerial vehicle (UAV) system. *Automation in Construction*, *41*, 1–14.

Snavely, N., Seitz, S. M., & Szeliski, R. (2008). Modeling the world from Internet photo collections. *International Journal of Computer Vision*, *80*(2), 189–210.

Stark, T. D., & Choi, H. (2008). Slope inclinometers for landslides. *Landslides*, *5*(3), 339–350.

Stumpf, A., Malet, J.-P., Allemand, P., Pierrot-Deseilligny, M., & Skupinski, G. (2015). Ground-based multi-view photogrammetry for the monitoring of landslide deformation and erosion. *Geomorphology*, *231*, 130–145.

Varnes, D. J. (1958). Landslide types and processes. *Landslides and engineering practice, 24,* 20-47.

Varnes, D. J. (1978). Slope movement types and processes. *Landslides, Analysis and Control, Special Report*, *176,* 11-33.

Westoby, M. J., Brasington, J., Glasser, N. F., Hambrey, M. J., & Reynolds, J. M. (2012). "Structure-from-Motion" photogrammetry: A low-cost, effective tool for geoscience applications. *Geomorphology*, *179*, 300–314.

Yaprak, S., Yildirim, O., Susam, T., Inyurt, S., & Oguz, I. (2018). The role of unmanned aerial vehicles (uavs) in monitoring rapidly occuring landslides. *Natural Hazards and Earth System Sciences Discussions*, 1–18.

Yu, H. S., Salgado, R., Sloan, S. W., & Kim, J. M. (1998). Limit analysis versus limit equilibrium for slope stability. *Journal of Geotechnical and Geoenvironmental Engineering*, *124*(1), 1-11.

Yu, M., Huang, Y., Zhou, J., & Mao, L. (2017). Modeling of landslide topography based on micro-unmanned aerial vehicle photography and structure-from-motion. *Environmental Earth Sciences*, *76*(15), 520.

Zhang, H., Lu, Y., & Cheng, Q. (2008). Numerical simulation of reinforcement for rock slope with rock bolt (anchor cable) frame beam. *Journal of Highway and Transportation Research and Development (English Edition)*, *3*(2), 65–71.

Zienkiewicz, O. C., Humpheson, C., & Lewis, R. W. (1977). Discussion: Associated and non-associated visco-plasticity and plasticity in soil mechanics. *Géotechnique*, *27*(1), 101–102.